COSMOGRID

Three-dimensional models of astrophysical magnetohydrodynamical jets

by

Gareth Charles Murphy

A Thesis submitted to
The University of Dublin
for the degree of

Doctor in Philosophy

School of Cosmic Physics,
Dublin Institute for Advanced Studies
and
School of Physics,
University of Dublin,
Trinity College

May, 2007

I hereby declare that this thesis has not been submitted as an exercise for a degree at this or any other University and that it is entirely my own work.

I agree that the Library may lend or copy this thesis upon request.

Signed,

Gareth Murphy

November 8, 2017.

Summary

In the previous fifty years it has become clear that jets and outflows play a vital role in the formation of stars and compact objects. Jets from young stellar objects typically show Herbig-Haro knots and bow shocks. Additionally, it now appears that (1) most stars form in binaries, and (2) jets from young stars are multiple and episodic outflows. Several groups have carried out large-scale simulations of jets, but often assuming a uniform ambient medium and a single disk and star. In this thesis the problems associated with non-uniform media and binary systems are explored. In order to understand the role of jets in star formation the questions are asked: how do jets from binary stars behave? What is the effect of the prehistory of jets on their collimation, acceleration and morphology?

To answer these questions, a parallel adaptive-grid magnetohydrodynamics code, ATLAS, is modified to include optically thin atomic radiative cooling losses. The code is rigorously tested, with particular reference to the shock-capturing and the radiative cooling. The tests used include one-dimensional shock-tube tests, two-dimensional blast waves, double Mach reflection of a strong shock from a wedge, the overstable radiatively cooling shock, and the Orszag-Tang vortex. A comparison of the code with another code, PLUTO, for the type of jet problems solved in this thesis is also performed. Using ATLAS, the propagation of jets in complex environments is studied. The first ever simulations of binary jets are performed. Three aspects of the problem are studied, the effects of source orbiting, the effects of interaction, and the role of the magnetic field. It is shown that jets from binary stars can interact and the signature of the interaction is demonstrated. The negligible effect of source orbiting is demonstrated. A toroidal magnetic field is placed in the ambient environment and further accentuates the interaction. Following on from this work, the evolution of the jet when the environment is not uniform is studied. Simulations have been performed which track the evolution of a jet in an partially evacuated cavity. The parameter space of the problem is explored in axisymmetry. The strong effect of the cavity on the recollimation, the acceleration and the radiative cooling losses is demonstrated.

Acknowledgements

I would like to thank my supervisors in the School of Cosmic Physics, Professor Luke O'C. Drury and Dr. Thibaut Lery for scientific guidance, direction, availability and knowledge, Professor Denis Weaire for being my internal supervisor in Trinity College, and Professor Thomas P. Ray for extensive help and assistance in all things jet-related.

Stephen O'Sullivan without whom all this would have been impossible and for hosting in NASA plus many many questions and emails answered, Andrew J. Lim for all the physics and programming help, Alex Rosen for insight, perspective and moral support and thorough revision, Dirk Froebrich for all the observational and dust extinction help, Turlough Downes for many emails and questions answered, Fabio De Colle for much Riemann solver assistance, Andrea Mignone for CTU correction, Claudio Zanni for IDL chombo-reading files, Francesca Bacciotti for explanations of ionisation fractions, Silvano Massaglia for Kelvin-Helmholtz assistance, David Collins and Brian W. O'Shea for explaining the Roe solver and for driving me around Hawaii, L.A. and Chicago, Dave Nutter for a lift up to the top of Mauna Kea, Cóilín Ó Maoiléidigh for all the business plan help, John Walsh for Grid assistance, David O'Callaghan, for helping with the Grid submission. Stephane Dudzinski for installing everything and fixing everything also John Allman and Diarmuid Bourke, David Golden for multitasking, managing and paging in CFD memory, S.A.E.G. Falle, for providing a copy of the Godunov paper, Brian Reville, for correcting errors, Sean Corkery, for being a great host, Dr Stefan Hutzler and Dr Kenneth A. Brakke for plenty of advice during the minimal surfaces course.

Rachel Curran, for polarimetry help and every single other thing, Dr. Emma T. Whelan. B.A., Ph.D. for observational help and explaining mysteries, Fiona McGroarty for being sensible, Celine Combet for much confederacy and putting up with me, Cian Crowley for IDL help, Deirdre Coffey for hosting in Arcetri, Matt Redman for sheer expertise, John D. Sheehan for frogmarching me home from excessive study, Eimhear Clifton for overcoming misgivings and finally allowing me to get in the door, Hilary O'Donnell for smoked salmon and DIAS experience, Max Moorkamp for C++ omniscience.

Dublin Institute for Advanced Studies for the Hamilton Scholarship, CosmoGrid for funding, Anne Shaw for keeping everything running, HPC-Europa for the CINECA research grant, the Institute for Pure and Applied Mathematics, UCLA for funding to travel to IPAM workshop, University of Hawaii for the funding to travel to Hawaii, Bank Of Ireland for the initial training, funding and for a powerful motivation towards further study, J.-C. Desplat for HPC knowledge, ICHEC and

TCD HPC for computing horsepower.

My parents, Mary Keaveney (whose idea it all was in the first place) and Frank Murphy for much support, patience and financial assistance, Dr Paula Murphy for advice and climbing Snowdon, Dr Deirdre Murphy, Brendan, Siobhan Murphy, my flatmate Stephen Moynes for putting up with a lot of moaning and groaning, for providing accommodation, beer and wisdom and constantly being correct, Karen Law for being my Trinity Hall flatmate, fellow PhD-mates and writer-uppers Fergal Casey and Stephen Redmond, Neil Simon for providing laptop, wisdom and experience.

Everyone else - you know who you are.

Publications

Refereed Publications

Froebrich, D., Ray, T.P., **Murphy, G.C.**, Scholz, A., 2005, A&A, 432, L67
A Galactic Plane relative extinction map from 2MASS

Combet, C., Lery, T., **Murphy, G.C.**, 2006, ApJ, 637, 798
Transit flow models for low and high mass star formation

Froebrich, D., Scholz, A., Eislöffel, J., **Murphy, G.C.**, 2005, A&A, 432, 575
Star formation in globules in IC1396

Murphy, G.C., Lery, T., O'Sullivan, S., Spicer, D.S., Bacciotti, F. 2007, *in prep*
Interacting jets from binary stars

Murphy, G.C., Rosen, A., Lery, T., O'Sullivan, S., Spicer, D.S. 2007, *in prep*
Modelling Jet Recollimation in an Evacuated Ambient Medium

Posters & Proceedings

Murphy, G.C., Lery T., Drury L. O'C. 2003
Adaptive Mesh Refinement in a Grid Computing Environment
in AMR 2003,ASCI/Alliances Centre for Astrophysical Thermonuclear Flashes, Chicago, 2003

Lery, T., Combet, C., **Murphy, G.C.**, 2004, Ap&SS, 293, 263
The Environment of YSO jets

Combet, C., **Murphy, G.C.**, Lery, T., 2004
Flows around low & high mass young stellar objects: Effects of opacity & magnetic field
SF2A-2004: Semaine de l'Astrophysique Française, Paris, France, 2004

Murphy, G.C., Froebrich, D., Scholz. A. 2004
A galactic plane extinction map obtained from 2MASS - An Embarrassingly Parallel Problem
in Cores, Disks, Jets & Outflows in Low & High Mass Star Forming Environments Conference,

Canada 11-16 July 2004

Murphy, G.C., Lery, T., O'Sullivan, S., Spicer, D.S., Bacciotti, F. 2005
Interacting Jets from a Binary Source
Protostars and Planets V 2005

Murphy, G.C., Froebrich, D., Walsh, J., Scholz, A. 2005
Grid-enabled Extinction Mapping
in Cosmogrid 2005, University College Dublin

Lery, T., Combet, C., **Murphy, G.C.**, 2005, Ap&SS, 298, 375
Virtual MHD Jets on Grids

Lery, T., Combet, C., **Murphy, G.C.**, 2005, AIP Conference Proc., 784, 140
Star Formation Histories

Contents

Contents **vii**

List of Figures **xiii**

List of Tables **xxi**

1 Introduction **1**

1.1 Jets and outflows in nature . . . 1

1.2 Jets and star formation . . . 3

1.2.1 Gravitational collapse mediated by magnetic fields and turbulence . . . 3

1.2.2 Angular momentum problem . . . 5

1.2.3 Magnetocentrifugal launching . . . 6

1.2.4 Binary Star Formation . . . 7

1.2.5 Empirical Classification for Low Mass Stars . . . 9

1.2.6 High-Mass Stars . . . 9

1.3 Rival jet launching theories . . . 11

1.3.1 Stellar winds . . . 11

1.3.2 Disk-driven winds . . . 11

1.3.3 Boundary-layer driven winds . . . 13

1.4 Jets and shocks . . . 14

1.4.1 Shocks . . . 14

1.4.2 Radiative shocks and “Forbidden” line emission . . . 16

1.4.3 Magnetohydrodynamic shocks . . . 17

1.4.4 Jump-type (“J-type”) shocks . . . 18

1.4.5 Continuous-type (“C-type”) shocks . . . 19

1.4.6 Bow shocks and Internal Working Surfaces 19
1.4.7 Jet diagram 20
1.5 From the kinetic theory to MHD 20
1.5.1 Boltzmann's Equation 20
1.5.2 Moment Equations 21
1.5.3 Maxwell's Equations 22
1.5.4 Quasi-Neutral Single Fluid Approximation 23
1.5.5 Ideal MHD Approximations 23
1.5.6 Rankine-Hugoniot Conditions 24
1.6 Numerical methods for solving equations 25
1.6.1 History and current state of star formation jet simulations 27
1.7 Structure of this thesis 28

2 Numerical Method **29**
2.1 The Equations of Ideal Magnetohydrodynamics (MHD) 29
2.2 Numerical constraints 30
2.2.1 Shock-capturing Scheme 31
2.2.2 Shock-smearing – Artificial Dissipative Terms 31
2.2.3 Linear hybrid schemes 32
2.2.4 Godunov's Method 32
2.2.5 Reconstruction-Evolution Method 37
2.2.6 Multidimensional correction: The Corner Transport Upwind method 38
2.2.7 Satisfying and maintaining $\boldsymbol{\nabla} \cdot \mathbf{B} = 0$ 40
2.2.8 Modelling the Microphysics of Atomic Radiative Cooling 41
2.3 An MHD 3D numerical code: ATLAS 43
2.3.1 Parallelisation 43
2.3.2 Achieving Higher Resolution using Adaptive Mesh Refinement 44
2.4 Leda, a parallel cluster 44

3 Numerical Tests **51**
3.1 Introduction 51
3.2 HD Tests 52
3.2.1 One-dimensional Shock Tube 52

3.2.2 Blast Wave 53
3.2.3 Double Mach Reflection (DMR) Test 53
3.3 Cooling Tests 56
3.3.1 Overstable Radiative Shock 56
3.4 MHD Tests 57
3.4.1 MHD Shock Tube 57
3.4.2 Orszag-Tang Vortex 59
3.4.3 MHD Blast Wave 61
3.5 Simulation 62
3.6 Code comparison and scheme comparison 62
3.6.1 PLUTO description 62
3.6.2 Performance 63
3.6.3 Comparison I: Underdense Adiabatic Jet 63
3.6.4 Comparison II: Overdense Adiabatic Jet 63
3.7 Summary 64

4 Jets from Binary Protostars 67
4.1 Introduction 68
4.1.1 Jets and star formation 68
4.1.2 Binary Systems 68
4.1.3 Models for Binary jets 68
4.2 Observations of jets from the binary protostar IRS 5 70
4.2.1 Morphology 72
4.2.2 X-ray emission 73
4.2.3 Polarimetry 73
4.3 Method 73
4.3.1 Initial and boundary conditions 74
4.4 Results 75
4.4.1 Case I: HD 75
4.4.2 Case II: MHD 76
4.4.3 Case III: Orbiting binary jet 78
4.4.4 Emission maps 79
4.5 Discussion 79

4.5.1 The source of X-ray emission . . . 79
4.5.2 Magnetic field effects . . . 81
4.5.3 Source orbiting effects . . . 81
4.5.4 Jet merging . . . 81
4.6 Conclusions . . . 82

5 Jet Recollimation and Acceleration in an Evacuated Cavity 83
5.1 Introduction . . . 84
5.1.1 Motivation: Circulation Model . . . 84
5.1.2 Motivation: Prehistory of Jets and Outflows from the Source . . . 85
5.1.3 Recollimation . . . 85
5.2 Method . . . 86
5.2.1 Numerical method . . . 86
5.2.2 System of equations . . . 86
5.2.3 Initial and boundary conditions . . . 87
5.3 Results . . . 88
5.3.1 Parameter space exploration . . . 88
5.3.2 Case I: Pulsed, overdense adiabatic jets in cavities . . . 89
5.3.3 Case II: Pulsed, underdense adiabatic jets in cavities . . . 89
5.3.4 Case III: Steady, radiatively cooling jet in cavity . . . 89
5.3.5 Case IV: Pulsed, non-adiabatic jet in cavity . . . 90
5.3.6 Pulsed, non-adiabatic, three-dimensional jet in cavity . . . 90
5.4 Discussion . . . 90
5.4.1 The effects of collimation and acceleration . . . 90
5.4.2 Observational signatures of the circulation model . . . 91
5.4.3 Prehistory of jets . . . 91
5.5 Conclusions . . . 91

6 Conclusions and Future Work 99
6.1 Code Testing and Code Comparison . . . 99
6.2 Jets from Binary Protostars . . . 100
6.3 Jets in Evacuated Ambient Media . . . 101
6.4 Future Work . . . 102

6.4.1 Jets from Binary Protostars 102
6.4.2 Jets in Evacuated Cavities 103

Bibliography **107**

A List of variables used in the text **119**

B Derivation of the energy equation from the second moment of the Boltzmann equation **121**

List of Figures

1-1 Jets from young stellar objects at different ages. Chains of Herbig-Haro knots, jet wiggling, and the terminal bow shock are all visible. Upper Left Credit: C. Burrows (STScI, ESA), the WFPC 2 Investigation Definition Team, and NASA Upper Right Credit: J. Hester (Arizona State University), the WFPC 2 Investigation Definition Team, and NASA Bottom Credit: J. Morse/STScI, and NASA. 3

1-2 Left panel: Taurus-Auriga giant molecular cloud in ^{13}CO. Right panel: Star formation region: the Orion Nebula (NGC 1976, M42) - a 2.5 light-year section of the giant molecular cloud and star-formation region in Orion. The colour composite image shows oxygen in blue, hydrogen in green and nitrogen in red - atomic lines generated by reflection from nearby main sequence and massive stars. Image from NASA, C.R. O'Dell and S.K. Wong (Rice University). 4

1-3 Schematic of the star-disk-outflow configuration. Typically $\sim$90% of the infalling material is accreting onto the star, carrying $\sim$10% of the angular momentum. The 10% not accreted will be flung off in an outflow, carrying 90% of the angular momentum. 6

1-4 Classification of low mass protostars according to their spectral energy density and their bolometric temperature (Andre et al. 1993). The temperature increase is seen in the movement of the spectrum down the wavelength axis. The excess of infrared was deduced by observers to be some material distributed around the star in such a way as not to completely block it out. The presence of a disk was surmised. 8

1-5 The Disk Wind Model, the jet is magnetocentrifugally launched from a broad region in the disk (Figure from Snell et al. (1980)). 12

1-6 Shu's X-Wind Model - the jet or x-wind is launched from the R_x region, close to the central object (Shu et al. 1994a). 13

1-7 The three hydrodynamic waves arising from the breakup of a discontinuity in a fluid in a one-dimensional shock tube. The entropy wave, u, separates the forward-moving shock or rarefaction from the reverse-moving shock/rarefaction. 15

1-8 Terminal Working Surface in the rest frame of the shock. 16

1-9 Crossing the shock, there is a rapid increase in density. The density then gradually increases as the thermal energy is radiated away. Shown in the figure are the cooling zones of [OIII], [OII] and [OI]. 17

1-10 The seven magnetohydrodynamic waves arising from the breakup of a discontinuity in a fluid. The contact wave, u, separates the forward-moving family of slow magnetosonic, Alfvén and fast magnetosonic waves from the backward-moving family. 17

1-11 Jump-type Shocks and Continuous-type Shocks , T_n denotes the neutral temperature, n denotes the neutral number density. v denotes the velocity. 18

1-12 Basic features of a radiatively cooling jet - bow shock, internal working surfaces and cocoon. 19

1-13 Numerical methods for solving the fluid partial differential equations 26

2-1 The top two panels show the initial and final states for a purely hydrodynamical one-dimensional shock tube problem. The lower right panel shows the x-t characteristics for the same problem. (Figure from Haque 2006). 33

2-2 Piecewise-constant, piecewise linear and piecewise parabolic reconstruction of the cell interface values. 37

2-3 Isopycnics for 300 km s^{-1} purely hydrodynamic jet with atomic radiative cooling at $t = 317$ years. The adiabatic atomic jet has a bow shock which has been broken up by cooling – causing loss of pressure which erodes the bow shape. 46

2-4 A depiction of the corner transport upwind method for the advection equation in two dimensions. Using the method shown in the left panel results in the south west cell being unrepresented in the flow. 47

2-5 The constrained transport method relies on the explicit use of Stokes' theorem, (Faraday's law), taking the path integral of the electric field, $\mathcal{E}$, around the closed contour, in this case the cell face shown by red arrows in the diagram. 47

2-6 Log normalised radiative cooling loss Λ, where $L_{cooling} = \rho^2\Lambda$ plotted against log temperature Sutherland & Dopita (1993). 48

2-7 Density comparison of 2D slab-symmetric jet propagating with cooling turned off (lower panel) and on (upper panel). Jet velocity = 300 km/s. Density, 120 cm^{-3}, temperature 1000 K. The jets are density and pressure matched to the ambient medium. Note the slower speed of the cooled jet, the distortion of the bow shock, and the shape of the core of the jet. 48

2-8 7 levels of adaptive mesh refinement for a 2D integration. 48

2-9 Adaptive Mesh Refinement Example; this is an early stage of a 2D cylindrical symmetric jet simulation. Four levels of refinement are visible. The individual cells are not shown as they obscure the image - shown instead are the boundary boxes each of which bounds 10x30 cells. 49

3-1 Results of one-dimensional HD shock tube test at time t=0.8 for comparison with Laney (1998) Left panels show pressure, velocity, and sound speed. Right panels show density, entropy and Mach number. The simple features of the expansion fan, contact discontinuity, and shock have all been captured. 53

3-2 The most important feature of the 2D blast wave test is its perfect symmetry. The shock is also well-resolved. Density colourmaps at times: t=3, 6, 9, 12. The units are arbitrary. 54

3-3 A strong shock striking a reflecting wedge gives rise to a complicated pattern of shocks and contact discontinuities. Photograph taken from Van Dyke (1964). . . . 55

3-4 Double Mach Reflection Initial Conditions. 55

3-5 Isopycnics for double Mach reflection, parameters are α=60° , γ=1.4, M=10. This compares well with published results using this test (Woodward & Colella 1984; Stone & Norman 1992; Berger & Colella 1989). Main features visible include the contact discontinuity roll-up along the lower right of the image, launching a jet of dense material towards the Mach stem and causing it to bulge outwards, the triple point or lambda point where the three shocks meet and the wall heating error where the perfect resolution at the a priori boundary condition contrasts with the slight smearing by the numerical code. 56

3-6 Isopycnics for double Mach reflection. Detail of Figure 3-5 - notice the Kelvin-Helmholtz instability on the contact discontinuity. The triple points are evident at the upper left and right corners of the image. The jet of dense material which causes the Mach stem to bulge outwards is also visible. 57

3-7 Strong radiative shock reflected from a wall, oscillating back and forth. 57

3-8 Shock position vs. time plotted for overstable radiative shock test, for velocities, 140, 160, 170 km/s. The results shown for velocities of 140, 160 and 170 km/s demonstrate that the stability limit lies in the range below 140 km/s. 58

3-9 Results of the first one-dimensional MHD shock tube Ryu & Jones (1995) test at time t=0.8 for comparison with Ryu & Jones (1995). The results of the simulation show the main features, fast shock, slow rarefaction, contact discontinuity, slow shock and fast shock have all been captured, however the contact discontinuity has been smeared over a few cells. 59

3-10 Results of the second one-dimensional MHD shock tube Ryu & Jones (1995) test at time t=0.8 for comparison with Ryu & Jones (1995). The results of the simulation show the main features, fast shock, slow slock, contact discontinuity, slow rarefaction and fast rarefaction have all been captured, however the contact discontinuity and slow shockhave been smeared over a few cells. There are also some small oscillations near the fast rarefaction (at the extreme right). 60

3-11 Contours of magnetic pressure *(upper left)*, thermal pressure *(upper right)*, compressibility $\nabla \cdot \mathbf{v}$ *(lower left)* and vorticity $\nabla \times \mathbf{v}$ *(lower right)*. Periodic boundary conditions were used on a domain of x=[0,1], y=[0,1] using 256x256 cells with a Courant number of 0.5. The initial configuration was set to match that of RJF and is $\rho = \frac{25}{36\pi}, v_x = -\sin(2\pi y), v_y = \sin(2\pi x), v_z = 0, B_x = -\sin(2\pi y), B_y = \sin(4\pi x), B_z = 0, p = \frac{5}{12\pi}$ The results show excellent agreement with Londrillo & Del Zanna (2000), O'Sullivan (1999), Dai & Woodward (1998), Ryu et al. (1998), Ryu et al. (1995). 61

3-12 Solution for the MHD blast wave log magnetic pressure, density and log thermal pressure at time t=0.2. The field lines are overplotted onto the density colourmap. The initial conditions are: $\rho = 0.1, B_x = 10/\sqrt{(2)}, B_y = 10/\sqrt{(2)}, p = 0.1$. The grid is of unit side with periodic boundary conditions. 65

3-13 Comparison of numerical codes ATLAS and PLUTO for an underdense ($\eta = 0.1$) jet, using directionally unsplit schemes and Roe solver. 66

3-14 Density colourmaps of a comparison of numerical codes ATLAS (left panel) and PLUTO (right panel) for a Mach 10 jet, using directionally unsplit schemes and Roe solver. 66

4-1 Left panel: Cartoon of LDN1551 IRS 5 jets. Right panel: Cartoon of H111 and HH121 jets. 70

4-2 Observations of LDN 1551 IRS 5. The upper panel shows an image of the jet pair in [FeII] from Pyo et al. (2002). The middle panel is a radio image at 3.6 cm of the binary jet which shows the blue and red lobes of the binary jets from Rodríguez et al. (1998). The two rectangles at the centre of the image mark the positions of the two disks. The solid lines show the estimated directions of the two disks. The lower panel is a radio image of the pair disks which drive the binary jets at7 mm from Rodríguez et al. (1998). 71

4-3 Observations of LDN 1551 molecular cloud in [SII] on the Cerro Tololo Telescope, from Moriarty-Schieven et al. (2005). The infrared source of the binary jets, IRS 5 is located at RA 04 31 34.20 DEC +18 08 04.8. 72

4-4 Fridlund & Liseau (1998) provide a HST R-band image of the two jets from the binary protostar LDN1551 IRS 5, located in the constellation Taurus. (Image courtesy of Fridlund & Liseau (1998)) 75

4-5 The bent morphology of the southern (lower) jet is visible in this midplane colour density map of 3-D binary jet simulation at $t = 245$ years. The scale of the grid is 1500AU by 400AU. 77

4-6 Time evolution of MHD binary jets at t=125, 155, 170, 185 years. The images shown are 2D midplane cuts through the 3D grid. Blue is low-density, red is high density. Note that the angle between jet axes is quite discernable in the earliest panel, but not so much later, which shows the bending of the slow, southern jet over time. 77

4-7 Surface plot of 3-D binary jet simulation at $t = 1648$ years. The scale of the grid is 4×10^{17}cm $\times$ 10^{17}cm $\times$ 10^{17}cm A longitudinal magnetic field of $10^4 \mu$G is used. 78

4-8 [SII] line emission map to compare with observations of the LDN1551 IRS 5 jet (HH154). The image shows the lower part of the two jets at a time t=190.2 years. The emission map is quite different to what is seen in the density contour and shows that the second jet is almost obliterated by the faster jet. There is a peak in emission where the bow shock is striking the beam. 80

5-1 HH30, a high velocity ($v_{jet} \sim 200$ km s^{-1}), highly collimated (opening angle $\sim 2°$ degrees) jet from a young star. Image from Alan Watson (UNAM, Mexico), Karl Stapelfeldt (JPL), John Krist (STSI) and Chris Burrows (ESA/STSI) 84

5-2 The circulation model: the densities are shown in log scale colour and the velocity field is shown by the arrows. From Combet et al. (2006). 85

5-3 Overdense (η=10), 300 km s^{-1}, Mach 800 adiabatic jet, velocity-pulsed with an amplitude of 30% and a period of 9.6 years (3×10^8 s) injected into (left panel) an evacuated cavity, with density decrement, δ=10. Strong recollimation and rapid acceleration are evident, compared with the right panel, which shows an identical jet in constant density ambient medium (CDAM). The box is an axisymmetric rectangle 3×10^{17} cm by 8×10^{16} cm. An adaptive grid is used with 6 levels of refinement, and a resolution equivalent to 256x1024-sized uniform mesh. 93

5-4 Underdense (η=0.1), 300 km s^{-1}, Mach 800 adiabatic jet, velocity-pulsed with an amplitude of 30% injected into (left panel) an evacuated cavity with density decrement, δ=10, (right panel) a constant density ambient medium (CDAM). The acceleration is most pronounced in this case. 94

5-5 Left panel: Steady, radiatively-cooled jet in evacuated cavity, with density decrement, δ=10 and η=1 Right panel: Identical jet in constant density ambient medium, with η=1 With strong radiative cooling typical of protostellar jets, recollimation is less apparent. The cooling instabilities are much less evident. 95

5-6 Left panel: Jet in evacuated cavity, with density decrement, δ=10 and η=1 Right panel: Jet in constant density ambient medium, with η=1 With strong radiative cooling typical of protostellar jets, recollimation is less apparent. The cooling instabilities are much less evident. 96

5-7 Left panel: Logscale density for 3d jet simulation without evacuated cavity at time t=588 years. Right panel: Logscale density for 3d jet simulation in evacuated cavity at the same time. 97

5-8 Left panel: Logscale Hα line emission for 3d jet simulation without evacuated cavity Right panel: Logscale Hα line emission for 3d jet simulation in evacuated cavity 98

6-1 Log density colourmap of axially symmetric MHD disk wind simulation at t=63. (Time units are Keplerian periods a the disk inner radius) As the disk wind moves upward from the disk it becomes collimated. The fast magnetosonic and Alfvén surfaces are plotted as yellow and black contours respectively. 105

List of Tables

1.1 The relative sizes of astrophysical jets 2

1.2 Typically observed parameters for jets and molecular outflows associated with Class I protostars
1. Eislöffel et al. (2000),
2. Bacciotti & Eislöffel (1999),
3. Downes (1996) 10

2.1 Nodes on the Leda cluster 45

3.1 A Test Matrix for Shock-capturing codes 52

4.1 Evidence of Binary Jets and Outflows? 69

4.2 Observed data for LDN1551 IRS 5 74

4.3 Initial conditions 76

5.1 Parameters used in the numerical calculations 88

5.2 Parameter Space 88

5.3 Jet aspect ratios and bow shock advance speeds for cases I-IV 92

“In science there is only physics; all the rest is stamp collecting.”

Ernest Rutherford, 1st Baron Rutherford of Nelson

1

Introduction

In this Chapter we review the subjects of jets and outflows in star formation, introducing the theories and problems associated with gravitational collapse, conservation of angular momentum and magnetocentrifugal launching of jets. We discuss the rival theories for the launching of jets from young stars and the role of shocks, give an overview of the derivation of the equations of magnetohydrodynamics from the kinetic theory and outline the numerical methods used for solving the magnetohydrodynamics equations. A survey of the history and current state of star formation jet simulations is also presented.

1.1 Jets and outflows in nature

Matter does not remain stationary in the Universe, but moves and accelerates, driven by gravity and electromagnetic forces, collapsing into stars, exploding in supernova, streaming in jets and outflows. The interplay between the forces results in complex and often unexpected results. A good example of this may be seen in the large molecular clouds which pervade the galaxy, and collapse under the influence of gravity. Surprisingly, inspection of the collapsing cloud reveals not

	Length	*Central Mass*
AGN	2,500 pc	$10^8 M_{sun}$
YSO	0.1 pc	$1 M_{sun}$
BD	<< 0.1 pc	$0.013 M_{sun}$

Table 1.1: *The relative sizes of astrophysical jets*

just infalling matter but *outflow*, in the form of narrow high-speed jets and wide-angle lower-speed molecular outflows. Outflows appear to be ubiquitously linked with the process of accreting material onto a central mass. In fact, they are commonly found in observations of active galactic nuclei (AGNs), brown dwarfs (Whelan et al. 2005), X-ray binaries, young stellar objects (YSOs), planetary nebulae (PN; Vlemmings et al. 2006), microquasars (Paredes et al. 2002), and their presence is inferred in observations of gamma-ray bursts (GRB; Maiorano et al. 2006). They exist over a broad range of mass scales from the smallest brown dwarf jets with central objects of only a few tens of Jupiter masses to the monumental jets from AGNs which extend over thousands of parsecs from central objects with masses of over 100 million $M_{\odot}$.

Although the American astronomer Sherbourne Wesley Burnham observed a "very small condensed nebula" near to the young star T Tauri in 1890, the first observation of an astrophysical jet proper was that of Heber Doust Curtis (1918) who described a "curious straight ray ... apparently connected to the nucleus by a thin line of matter" near the spiral galaxy M87. This research is primarily focussed on jets and outflows in the star formation process. These have been observed in the form of chains of emitting nebulae first separately observed by Herbig (1951) and Haro (1952). The nebulae were named Herbig-Haro objects (or HH objects) in their honour. Osterbrock (1958) suggested that the HH objects might be related to mass-loss caused by rotation of the T Tauri star. Schwartz (1975) tabulated the forbidden-line emission ratios of an object in Burnham's Nebula (now called HH255) against those of a supernova remnant and was able to conclude that the line ratios could only be produced by a radiative shock. While it was originally speculated that the shock was caused by an ionised wind striking a small cloudlet (Schwartz 1978), it was soon realised that the convexity of the bow shock implied a directed flow impinging on an ambient medium. The chains of visible Herbig-Haro knots were originally attributed to crossing shocks in the jet (Falle et al. 1987), but are now considered much more likely to be induced by velocity variations in the outflow (Raga et al. 2001).

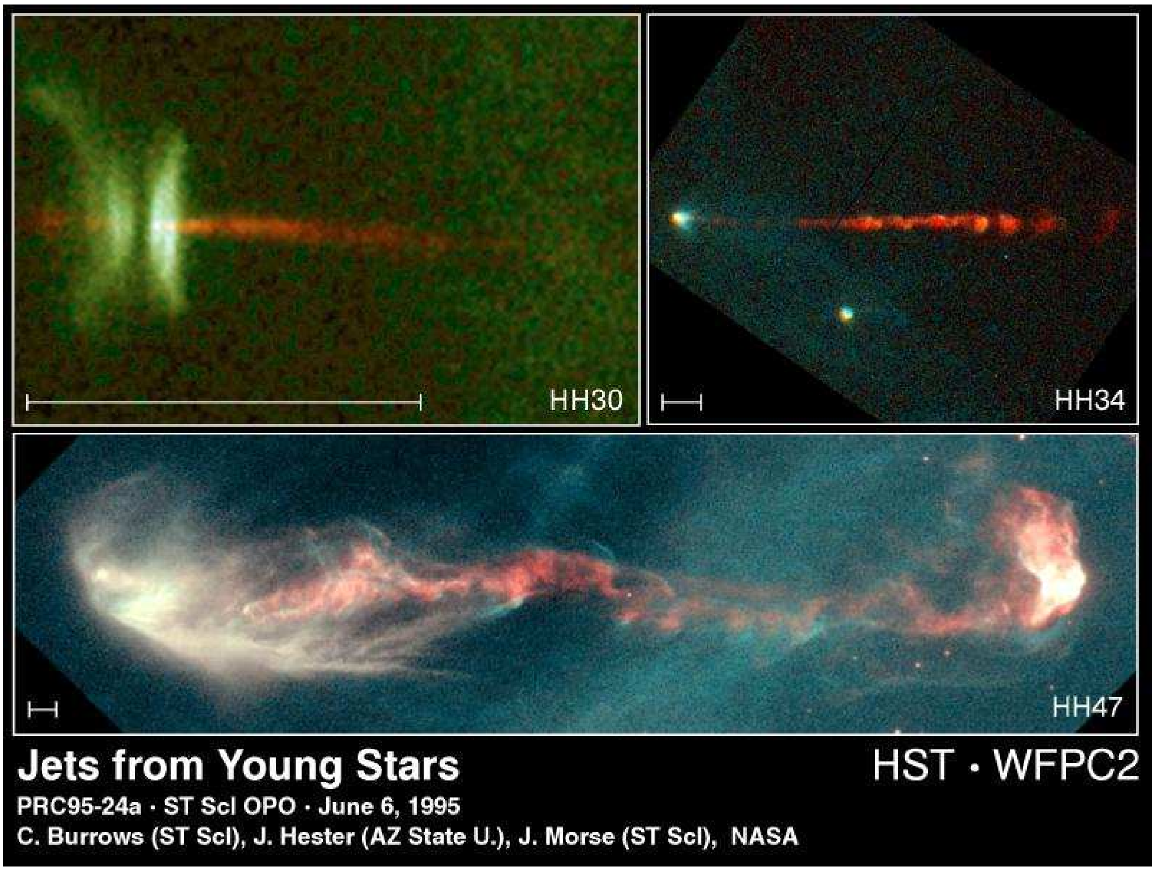
HH30
HH34
HH47
Jets from Young Stars
HST • WFPC2
PRC95-24a • ST ScI OPO • June 6, 1995
C. Burrows (ST ScI), J. Hester (AZ State U.), J. Morse (ST ScI), NASA

Figure 1-1: *Jets from young stellar objects at different ages. Chains of Herbig-Haro knots, jet wiggling, and the terminal bow shock are all visible. Upper Left Credit: C. Burrows (STScI, ESA), the WFPC 2 Investigation Definition Team, and NASA Upper Right Credit: J. Hester (Arizona State University), the WFPC 2 Investigation Definition Team, and NASA Bottom Credit: J. Morse/STScI, and NASA.*

1.2 Jets and star formation

1.2.1 Gravitational collapse mediated by magnetic fields and turbulence

The modern theory of star formation has its origins in the nebular hypothesis of Kant (1755) and Laplace (1796). According to current understanding, a star begins life in a rotating molecular cloud, made up of mainly ($\sim$99%) molecular hydrogen and helium and dust. Giant molecular clouds may be observed in molecular lines (such as H_2 1-0 S(1)), 21cm hydrogen and optically thanks to reflected either light from nearby stars. They can also be seen in extinction maps in silhouette against light from background stars. The dust component plays a vital role in star formation, allowing material to cool down both by blocking light from other nearby stars (extinction) and by adsorbing

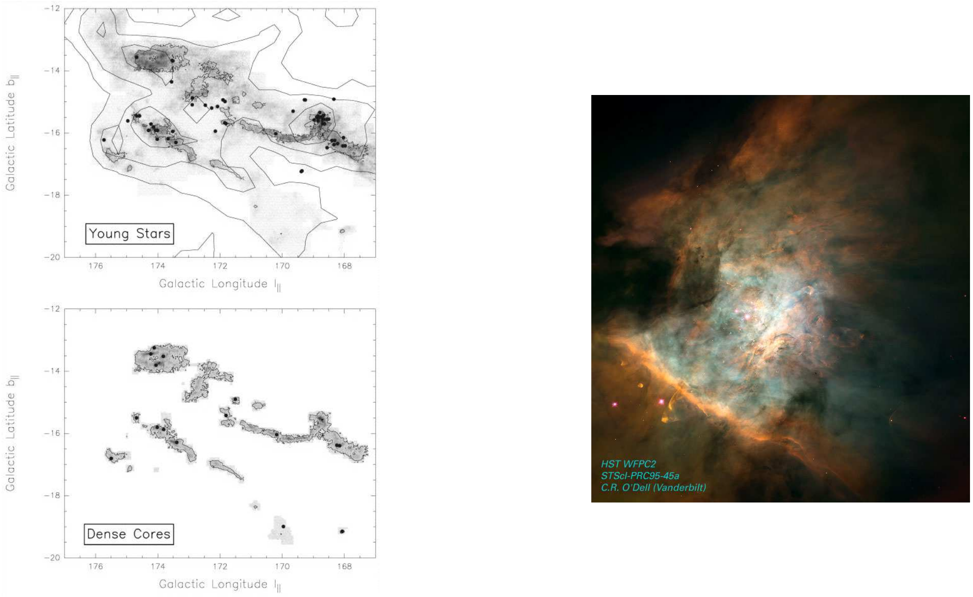

Figure 1-2: *Left panel: Taurus-Auriga giant molecular cloud in* ^{13}CO. *Right panel: Star formation region: the Orion Nebula (NGC 1976, M42) - a 2.5 light-year section of the giant molecular cloud and star-formation region in Orion. The colour composite image shows oxygen in blue, hydrogen in green and nitrogen in red - atomic lines generated by reflection from nearby main sequence and massive stars. Image from NASA, C.R. O'Dell and S.K. Wong (Rice University).*

hydrogen and onto grain surfaces and thereby catalysing the formation of molecular hydrogen, further cooling the molecular cloud (Hollenbach & McKee 1979). In Chapter 6 the extinction property of dust is exploited to produce maps of the dust clouds in the Galactic plane.

Giant molecular clouds are thought to be supported against gravitational collapse by a seemingly formidable coalition of thermal pressure, ambient magnetic fields and turbulence, but over time the turbulence can dissipate, and the cloud can become prone to condensing into clumps and subsequently cores when neutral matter is drawn together by the gravitational force and slips unaffected through the magnetic field lines in the process known as ambipolar diffusion. Such cores can be observed in molecular line emission and the submillimetre continuum. The process of condensation may also be triggered or accelerated by interactions from supernova remnants or jets and outflows, which create irregularities in the density structure of the molecular cloud (Bonnell et al. 1997). When matter builds up in a pressure-supported dense core it will eventually reach the Jeans mass[1], M_J. M_J corresponds to the limit of gravitational stability beyond which the cloud will start to collapse. The gravitational collapse will not be a pure free-fall but will be slowed by the magnetic field and turbulence. The infalling matter possesses an inherent angular momentum, and therefore will not in general precipitate directly on the small central object, but will instead distribute itself around the centre of gravity in the equatorial plane, forming a disk of matter typically rotating at Keplerian speeds very close to the centre of gravity. Such disks were originally inferred from the infra-red excess visible in the spectra of young stars, which implied some distribution of material about the central object, arranged so as not to obscure the young star completely. O'Dell et al. (1993) used the Hubble Space Telescope to produce the first images of the predicted disks.

---

[1] The Jeans mass, $M_J \approx {c_s}^3/\left(G^{3/2}\rho^{1/2}\right)$, where c_s is the sound speed, G , the Universal Gravitational Constant, and ρ is the average density. It is derived by equating the freefall time $t_{ff} \simeq /\sqrt{G\rho}$ to the sound wave crossing time

The rotating disk possesses an effective viscosity, the cause of which is still unknown, but may be due to the Balbus-Hawley (Magnetorotational) Instability (Balbus & Hawley 1991) generating turbulence in the disk . The more slowly moving material in the disk will gradually spiral inward and accrete onto the protostar, as long as it has velocity lower than the escape/break-up velocity of the protostar. If the protostar is magnetised the material inside the radius of the magnetosphere may accrete onto the protostar via the magnetic field lines. These columns of accreting material will generate shocks at their bases which may be detected as hot spots on the surfaces of accreting protostar. Fields in the range of a few kilogauss on the surface of a protostar have been observed (Hawley 1993). The role of turbulence is still an open question but it may tangle the magnetic field lines, transport angular momentum out of the disk and slow down the cloud collapse.

1.2.2 Angular momentum problem

Due to the conservation of angular momentum $m\omega r^2$, the angular velocity, ω will tend to increase, in order to compensate for the decrease in radius, r as the core collapses. Pudritz (1985) points out that observed accretion disk specific angular momenta ($\sim 10^{22}$ cm^2 s^{-1}) are much greater that those for formed stars ($\sim 10^{17-18}$ cm^2 s^{-1}). Indeed if all the angular momentum from the condensing cloud was conserved within the sytem it would lead to "ridiculous spin rates" (Lynden-Bell & Pringle 1974)). A mechanism is thus required to transport angular momentum out of the star-disk system. Angular momentum transport can be achieved through the *deflection* of infalling material into highly collimated jets or molecular outflows that are associated with protostars and young stars. Other mechanisms include the transfer of angular momentum from rotation to orbital motion (fragmention into a binary or multiple star), or transport of angular momentum outwards through the disk by turbulent viscosity (von Weizsäcker (1943), Lüst (1952) and Lynden-Bell &

$t_{cross} = R/c_s$.

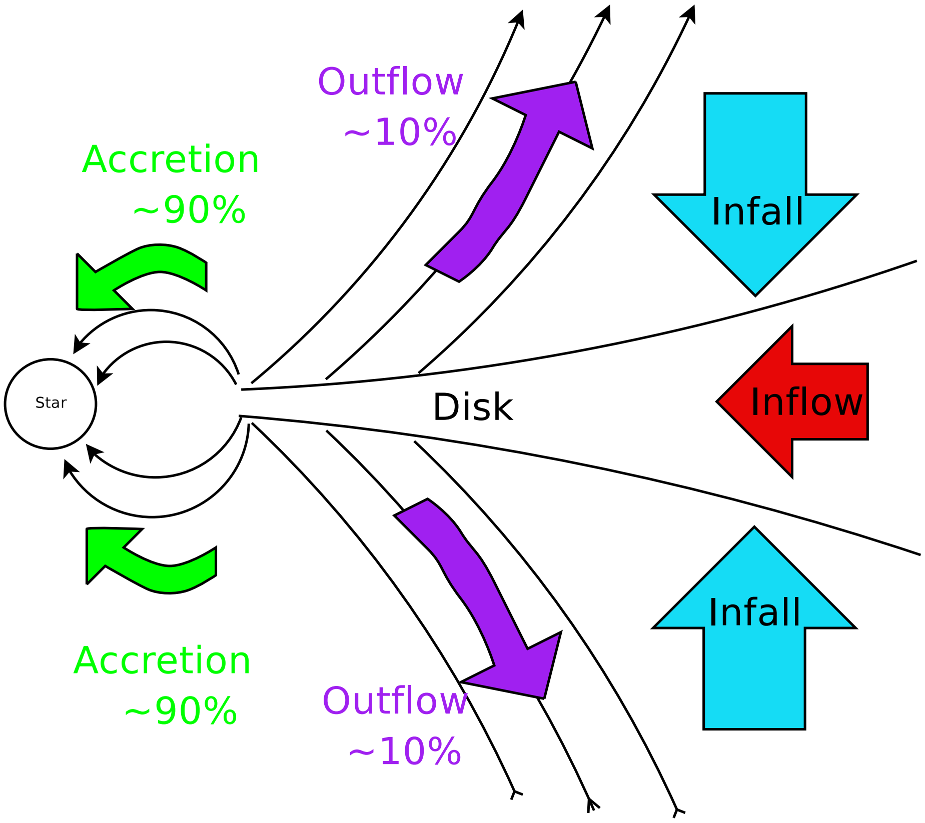

Figure 1-3: *Schematic of the star-disk-outflow configuration. Typically ∼90% of the infalling material is accreting onto the star, carrying ∼10% of the angular momentum. The 10% not accreted will be flung off in an outflow, carrying 90% of the angular momentum.*

Pringle (1974)).

1.2.3 Magnetocentrifugal launching

Rotating matter can be flung out from the polar regions of the disk like a magnetic slingshot and will preferentially travel along magnetic field lines like beads strung on a wire (Henriksen & Rayburn 1971) while slower moving matter continues to accrete onto the protostar. The flow of accreting and outflowing material is sketched in Figure 1-3. The cylindrical column of material which makes up the outflowing material will be bound to the disk by the magnetic field lines which thread it and will therefore corotate with it up to the Alfvén surface. (The Alfvén surface is defined as the surface at which the ram pressure of the outflowing material equals the magnetic pressure and the fluid is able to bend the magnetic field line. If the magnetic field is a dipole $\mathbf{B} = \frac{\boldsymbol{\mu}}{r^3}$ (where $\boldsymbol{\mu}$ is the magnetic moment) one can derive a closed-form expression for the Alfvén radius. Balancing the ram and magnetic pressures: $\rho v^2 = B^2 = \frac{\mu^2}{r^6}$ one gets $r_A = \left(\frac{\mu^2}{\rho v^2}\right)^{\frac{1}{6}}$. The dipole approximation is not necessarily valid for the whole star-disk region.) The outflowing material will, by applying a back torque, magnetically brake the disk, enough to allow collapse. (More angular momentum can be removed by the viscosity in the accretion disk as mentioned previously.)

1.2.4 Binary Star Formation

Although the above theories feature a cloud collapsing to form a single star, Duquennoy & Mayor (1991), Mayor et al. (1992), Zinnecker et al. (1992), Ghez et al. (1993), Simon et al. (1995), Preibisch et al. (1999), have studied multiplicity and found frequent examples of binarity. The binary formation mechanism, whether by fragmentation of a molecular core or capture of a nearby star by gravity must therefore be efficient. In Chapter 4 the role played by binary jets in the star formation process is explored.

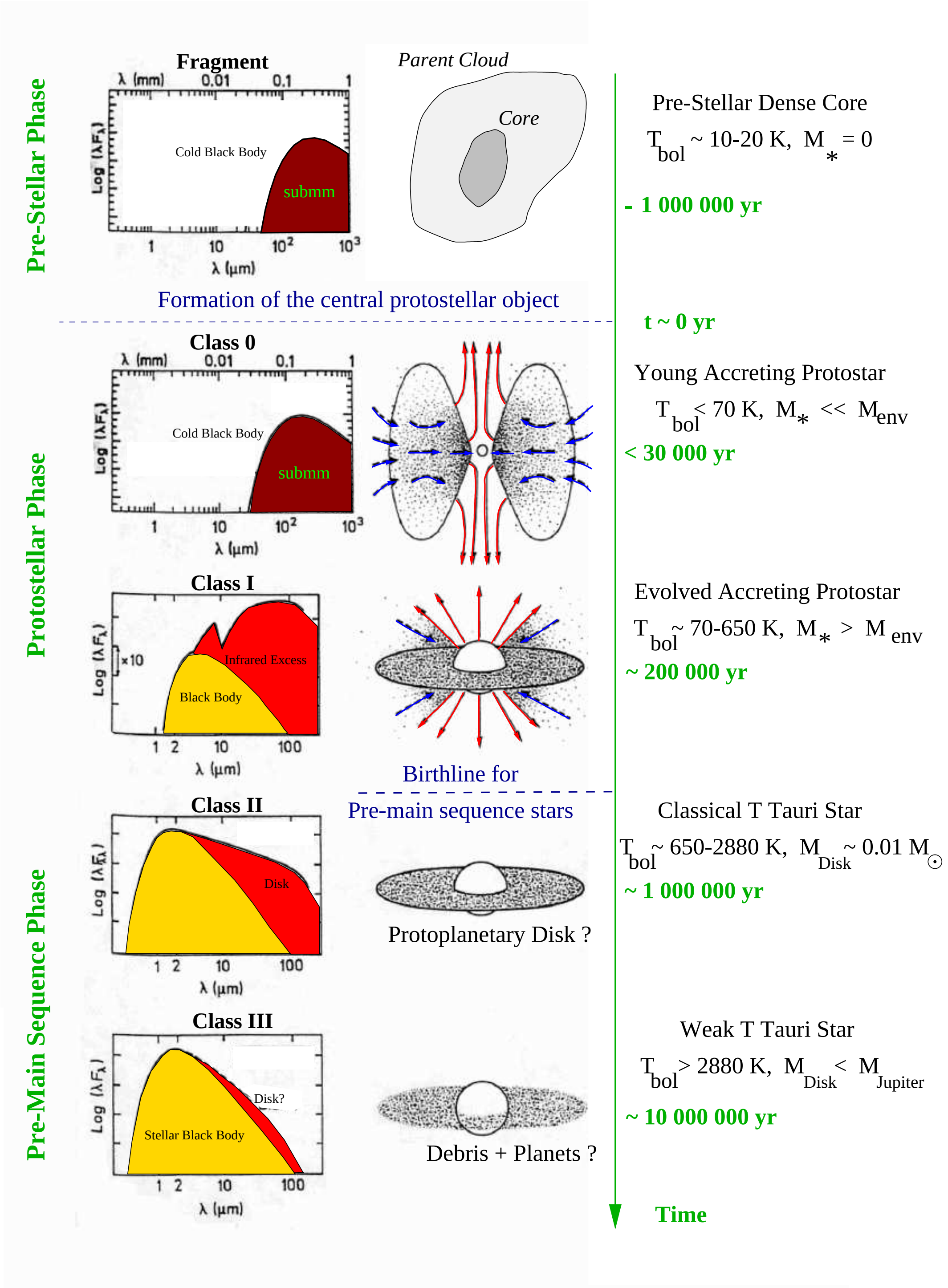
Pre-Stellar Phase
Fragment
λ (mm)
0.01
0.1
1
Log (λF_λ)
Cold Black Body
submm
1
10
10²
10³
λ (μm)
Parent Cloud
Core
Pre-Stellar Dense Core
T_bol ~ 10-20 K, M_* = 0
- 1 000 000 yr
Formation of the central protostellar object
t ~ 0 yr
Protostellar Phase
Class 0
λ (mm)
0.01
0.1
1
Log (λF_λ)
Cold Black Body
submm
1
10
10²
10³
λ (μm)
Young Accreting Protostar
T_bol < 70 K, M_* << M_env
< 30 000 yr
Class I
Log (λF_λ)
×10
Infrared Excess
Black Body
1
2
10
100
λ (μm)
Evolved Accreting Protostar
T_bol ~ 70-650 K, M_* > M_env
~ 200 000 yr
Birthline for
Pre-main sequence stars
Pre-Main Sequence Phase
Class II
Log (λF_λ)
Disk
1
2
10
100
λ (μm)
Protoplanetary Disk ?
Classical T Tauri Star
T_bol ~ 650-2880 K, M_Disk ~ 0.01 M_⊙
~ 1 000 000 yr
Class III
Log (λF_λ)
Disk?
Stellar Black Body
1
2
10
100
λ (μm)
Debris + Planets ?
Weak T Tauri Star
T_bol > 2880 K, M_Disk < M_Jupiter
~ 10 000 000 yr
Time

Figure 1-4: *Classification of low mass protostars according to their spectral energy density and their bolometric temperature (Andre et al. 1993). The temperature increase is seen in the movement of the spectrum down the wavelength axis. The excess of infrared was deduced by observers to be some material distributed around the star in such a way as not to completely block it out. The presence of a disk was surmised.*

1.2.5 Empirical Classification for Low Mass Stars

Observers have classified low-mass young stellar objects according to their spectra. This classification (Lada 1987; Andre et al. 1993) is depicted in Figure 1-4. The scheme is consistent with an evolutionary sequence, increasing in time from Class 0 to Class III. The first stage corresponds to Class 0 objects, the most deeply embedded sources. Such objects are still surrounded by infalling envelopes containing at least half of the mass of the central object. All Class 0 objects are associated with highly collimated molecular outflows, typically more energetic than those associated with the next stage, i.e. Class I objects. The latter are still deeply embedded in dense envelopes and not optically visible. They are often associated with jets and molecular bipolar outflows, though less energetic than those associated with Class 0 objects. Jets are highly collimated (opening angles of $\sim 1^\circ$ - 5°, radii of $\sim$ 0.001 pc - 0.05 pc), denser than the ambient medium (densities $\sim 10^2$ - 10^3 cm^{-3}) beams of matter travelling at high speeds ($\sim$ 200 km s^{-1}) which plough through the interstellar medium. Molecular outflows are more dense ($\sim 10^4$ - 10^6 cm^{-3}), less well-collimated flows with wider opening angles. Typical values for the jet and outflow parameters are shown in Table 1.2. Class II objects, or Classical T-Tauri stars, are surrounded by an accretion disk but with no infalling envelopes. Finally, Class III objects (weak T-Tauri stars) have a photo-sphere with a radial stellar wind although free of any significant amounts of circumstellar material. The outflowing material is either supersonically launched or accelerated up to supersonic speeds very rapidly. Jets propagate at supersonic and super-Alfvénic speed and in doing so they shock the gas in the ambient medium ahead, forming a bow shock. Additionally if the velocity of the jet is episodically varied at the source the jet will form internal shocks or working surfaces where the slower moving material meets the faster moving material. The resulting emission, highly visible in optical wavelengths, paradoxically the result of an outflow, is the main source of information to the earthbound observer about the accretion process which mainly consists of infall. In this study models are of jets from a Class I type protostar which are in general atomic, fast, less dense and narrow. Class 0 outflows are typically heavy, dense, slow, and molecular.

1.2.6 High-Mass Stars

High-mass star formation is even less well understood than low-mass star formation. Massive stars form in crowded clusters, riddled with multiple outflows and supernova remnants. A major problem with the theory is how high mass protostellar objects overcome the radiation pressure, which counteracts the gravitational force and in principle could halt the process of accretion (Kahn 1974; Yorke

	Jet	*Molecular Outflow*
Velocities:	50-400 km/s (1)	10-50 km/s
Density:	10^2 -10^3 cm^{-3} (2)	10^4 - 10^5 cm^{-3}
Length:	0.1 pc - 10 pc (3)	10^4 AU
Radius:	0.01 pc - 0.5 pc (3)	
Temperature:	10^3-10^6K	10-10^4K
Tracer materials:	[HI], [NII],[OI], [SII]	CO, H_2, SiO_3
Opening Angle:	1°-10° (3)	5°-40°

Table 1.2: *Typically observed parameters for jets and molecular outflows associated with Class I protostars*

1. Eislöffel et al. (2000),

2. Bacciotti & Eislöffel (1999),

3. Downes (1996)

& Kruegel 1977; Wolfire & Cassinelli 1987). Radiation pressure is thought to prevent stars of $>$ 20 solar masses (depending on the model) from forming, whereas stars of up to 100 solar masses have been observed (Figer et al. 2004). Massive stars have much shorter lives than low-mass stars, many different phenomena are present and occur on short timescales. O stars are deeply embedded for 15% of their lifetimes which makes them hard to observe (Wood & Churchwell 1989). Observations of such dusty regions are restricted to longer wavelengths. All or nearly all forming stars show strong outflows (Terebey et al. 1989). Observational difficulties are compounded by the fact that massive stars are relatively rare and the nearest massive star-forming region is 500 parsecs away in Orion. One theory of high-mass star formation is competitive accretion, somewhat endearingly termed the "nurture, not nature" scenario, where the amount of accretion is related to the number of neighbours (Bonnell et al. 2004). Another theory is the coalescence scenario, where low mass stars collide to form massive stars, avoiding the radiation pressure limit (Bonnell et al. 1998). Another school of theories concentrates on quantative adjustments of the standard low-mass star formation theory. It is also possible to increase the amount of material accreted if the radiation pressure or the accretion is anisotropic (Combet et al. 2006). See Beuther et al. (2005) for a review.

1.3 Rival jet launching theories

Although the major models for the generation of jets agree on the magnetocentrifugal origin of the jets - they diverge on other points. Following Bachiller (1996), the current models for jet generation can be subdivided into two main categories, disk-driven winds and boundary-layer driven winds.

1.3.1 Stellar winds

Very early analytical models by Parker (1958) were successful at explaining and predicting the velocity of the solar wind using a purely one-dimensional spherically symmetric hydrodynamic thermally driven wind. However this theory cannot explain the directional, collimated nature of the protostellar jets. Including the magnetic field in the analysis (Weber & Davis 1967) makes the wind directional. In fact it is not thought possible that highly collimated jets originate from protostellar surfaces. Bachiller (1996) gives several reasons why jets cannot originate from central stars.

- Neutral species observed at high velocities around YSOs suggest the origin of the wind could not be at the hot stellar surface.
- To drive a jet the star would need to rotate at or near breakup velocity - much faster than the observed T Tauri rotation speeds.
- There is a strong correlation between presence of jets and presence of disks for young stellar objects.

For these reasons it is thought that the jet origin is not at the central source but either in the disk or at the boundary layer.

1.3.2 Disk-driven winds

Several theories of jet formation of varying degrees of credibility exist. Blandford & Payne (1982, ; herafter BP82) in a seminal paper were responsible for an early jet generation model, originally devised for extragalactic jets but later applied to YSO jets by Pudritz & Norman (1983); Pudritz (1985); Pudritz & Norman (1986) and Königl (1989). BP82 imagined an external magnetic field threading a disk. If the poloidal component of the magnetic field makes an angle less than 60° from a rotating disk, the centrifugal force can fling a packet of gas off the surface of the disk to infinity. This may be visualised using the mechanical analogy suggested by Henriksen & Rayburn (1971) of a bead on a rigid massless wire attached to a rotating disk. If the wire is normal to the plane of

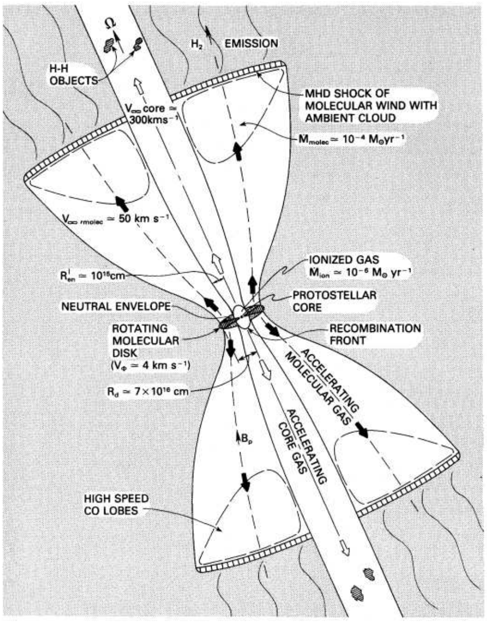
Ω
H-H
OBJECTS
H₂ EMISSION
V_∞ core ≃
300kms⁻¹
MHD SHOCK OF
MOLECULAR WIND WITH
AMBIENT CLOUD
$\dot{M}_{molec} = 10^{-4}\ M_\odot yr^{-1}$
$V_{\infty\ rmolec} = 50$ km s⁻¹
$R^i_{en} = 10^{16}$cm
IONIZED GAS
$\dot{M}_{ion} \simeq 10^{-6}\ M_\odot\ yr^{-1}$
PROTOSTELLAR
CORE
NEUTRAL ENVELOPE
ROTATING
MOLECULAR
DISK
($V_\Phi = 4$ km s⁻¹)
RECOMBINATION
FRONT
$R_d \simeq 7\times10^{16}$ cm
ACCELERATING
MOLECULAR GAS
ACCELERATING
CORE GAS
B_p
HIGH SPEED
CO LOBES

Figure 1-5: *The Disk Wind Model, the jet is magnetocentrifugally launched from a broad region in the disk (Figure from Snell et al. (1980)).*

the disk the bead will not move. If it makes an angle less than a critical angle to the disk the bead will move up the wire.

The magnetic field threading the disk is analogous to the wire, pinched in at the centre by an accretion disk (see Figure 1-5) which provided a bead-on-a-wire mechanism for the packets of gas to transport angular momentum away from the protostellar disk. The packet of gas will be launched at escape velocity, and accelerated up to the typical outflow velocity by the magnetic field. In their steady-state model, BP82 did not account for the time variations in velocity which appear to be the cause of several observed Herbig-Haro objects.

Uchida & Shibata (1985) performed the first numerical simulations of the disk winds, modelling the accretion disk's rotation twisted the field as well as the disk's contraction compressing and strengthening the field until powerful reconnection events occur leading to an episodic outflow burst. At this point the field lines are straight, normal to the disk and the cycle begins again.

Lovelace et al. (1995) discussed differential rotation causing loop inflation and opening of the field lines - allowing an outflow along the opened field lines. However, this is a steady flow model and does not account for episodic outflows. Goodson et al. (1997, 1999); Goodson & Winglee (1999) modelled differential rotation causing loop inflation resulting in reconnection releasing jet plasma from the system. This model is capable of producing an unsteady flow with knots.

The weaknesses of the disk-driven wind theory centre on the magnetic field. The required field

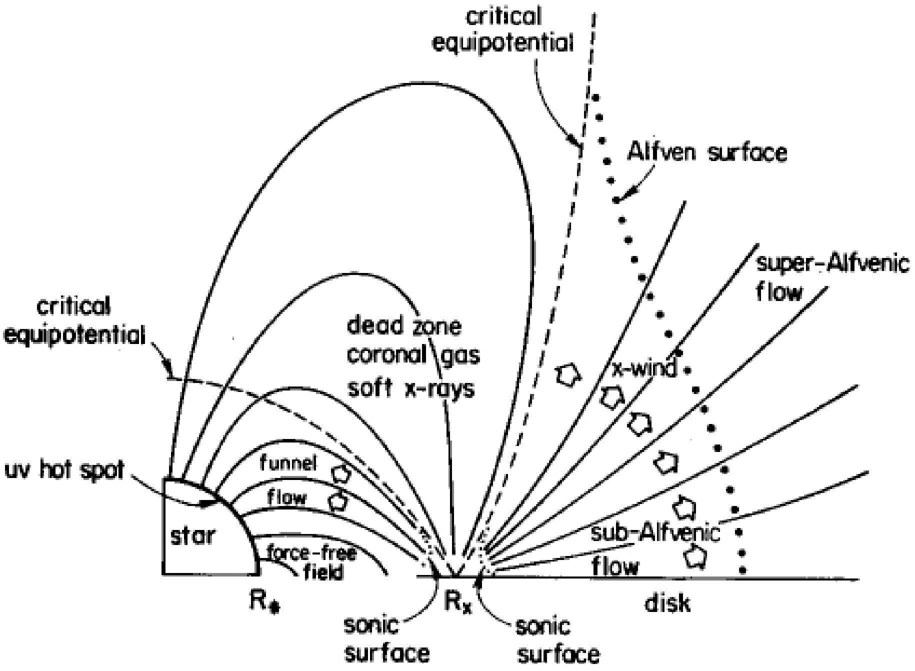
critical
equipotential
Alfven surface
super-Alfvenic
flow
critical
equipotential
dead zone
coronal gas
soft x-rays
x-wind
uv hot spot
funnel
flow
star
force-free
field
sub-Alfvenic
flow
R_*
R_x
disk
sonic
surface
sonic
surface

Figure 1-6: *Shu's X-Wind Model - the jet or x-wind is launched from the R_x region, close to the central object (Shu et al. 1994a).*

in the disk has to be maintained by a turbulent dynamo but this is expected to be too weak. The external fields in the disk are possibly insufficient to launch the wind. Matt et al. (2002); Matt & Pudritz (2004, 2005) pointed out that differential rotation causes opening of field lines which yoke the disk to the protostar. The magnetic torque provided by the closed field lines is thought to counteract the angular momentum deposited by accretion and allow the protostar to spin down (Königl 1991).

1.3.3 Boundary-layer driven winds

Boundary layer models were proposed by Shu et al. (1988), Pringle (1989), Camenzind (1990) and Bertout & Regev (1992). The most popular boundary-layer driven model is the X-Wind or X-celerator model. The X-Wind was model originally propounded by Shu et al. (1988) as a wind from a rapidly-rotating T Tauri star but extended and modified by Shu et al. (1994a,b); Najita & Shu (1994). This differs from the previous models in that the magnetic field is argued to be from the protostar rather than an external field threading the disk. Shu et al. (1994a) argue that the disk excludes the magnetic field. Pringle (1989) pointed out that the requirement for the protostar to be spinning at close to breakup is in contradiction with the observations. The modifications in Shu et al. (1994a) allowed for protostars rotating below breakup. Masson & Chernin (1992, 1993) found that the X-Wind model could not account for the mass-velocity power-law $m(v) \sim v^{-1.8}$ relation found consistently in CO observations of molecular outflows in L1551 (Moriarty-Schieven & Snell 1988), NGC 2051 (Moriarty-Schieven & Snell 1988) and HH46-47 (Chernin & Masson 1991). Chernin & Masson (1995) found that the X-Wind model could not account for observed momentum distributions. Li & Shu (1996) addressed the criticisms of Masson & Chernin (1992) and modified their model accordingly. The main weakness of the X-Wind model is that it is star-formation specific and cannot be applied to active galactic nuclei, which do not have magnetospheres. The X-Wind and disk-wind theories are not mutually exclusive - there could be for example a high-velocity component X-Wind in the centre surrounded by a lower velocity disk-wind.

1.4 Jets and shocks

Jets from young stellar objects are seen at optical, ultraviolet and infrared wavelengths thanks to their bright Herbig-Haro knots along their length and their terminating bow shocks.

1.4.1 Shocks

To understand shocks, a brief exposition of wave theory is given. Whitham (1974) intuitively describes a wave as “any recognisable signal that is transferred from one part of a medium to another with a recognisable velocity. The signal may be any feature of the disturbance such as a maximum or an abrupt change in some quantity”. A single conservation law in one dimension:

$$\frac{\partial u}{\partial t} + \frac{\partial f\left(u\right)}{\partial x} = 0 \tag{1.1}$$

may be written in the form:

$$\frac{\partial u}{\partial t} + a\frac{\partial u}{\partial x} = 0 \tag{1.2}$$

u is the signal or wave, a is the wavespeed. The curves $\frac{dx}{dt} = a$ are the characteristic curves or characteristics. If a is a function of u, the system is nonlinear. For a system of conservation laws, which could be for example the hydrodynamic equations or the equations of magnetohydrodynamics,

$$\frac{\partial \mathbf{U}}{\partial t} + A\frac{\partial \mathbf{U}}{\partial x} = 0 \tag{1.3}$$

If A is diagonalizable,

$$\frac{\partial \mathbf{v}}{\partial t} + Q^{-1}AQ\frac{\partial \mathbf{v}}{\partial x} = 0 \tag{1.4}$$

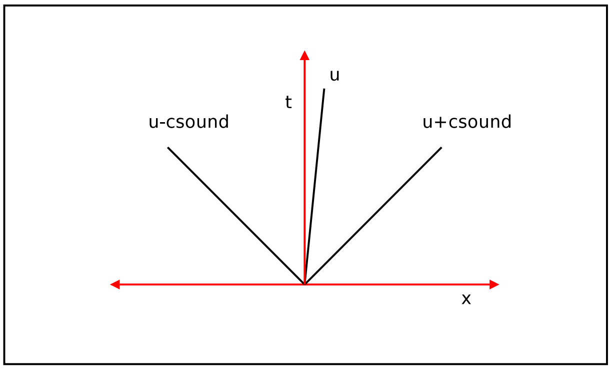

Figure 1-7: *The three hydrodynamic waves arising from the breakup of a discontinuity in a fluid in a one-dimensional shock tube. The entropy wave, u, separates the forward-moving shock or rarefaction from the reverse-moving shock/rarefaction.*

where Q is the matrix of right eigenvectors of the A, $\mathbf{v}$ is defined by $d\mathbf{v} = Q^{-1}d\mathbf{U}$, the eigenvalues λ_i of A are the wave speeds, $\mathbf{v}$ is the vector of signals or information carried by the waves or characteristic variables, the curves $\frac{dx}{dt} = \lambda_i$ are the wavefronts or characteristics. An example of the characteristics for the linearised wave equations is shown in Figure 1-7. When characteristics from the same family intersect a *shock* is formed. When the characteristics diverge, an *expansion wave* or rarefaction is formed. There is a third possibility, where the characteristics are parallel, entropy waves or contact discontinuities. Physically, a shock is characterised by a sudden violent abrupt change in pressure, temperature or velocity which happens over a distance so short (depending on the microphysics of the system this may be one mean free path for a collisional gas or one particle gyroradius for a low-density plasma) that it may be approximated as a discontinuous change. A shock travels faster than information can propagate though a system, so the medium has no time to react. Entropy waves or contact discontinuities are characterised by a jump in entropy, where the pressure is constant. Entropy waves may exist as static phenomena, whereas shocks result from dynamic action. Nonlinear acoustic waves steepen into shocks when they “break” like waves on a beach. Gas which passes through a shock or which a shock passes through is heated and compressed and cools by radiating energy. Many astrophysical problems, such as supersonic jets, novas, coronal mass ejections, involve large masses of gas colliding at high speeds. In such cases, a mathematical description may be applied by abstracting the situation to a one-dimensional “shock tube”.

The contact separates the shock from another wave, which may be either compressive (shock) or rarefactions/expansion (see Figure 1-7). In the case of a jet propagating into an ambient medium there is a forward moving shock at the head of the jet (the bow shock) and a reverse shock (Mach

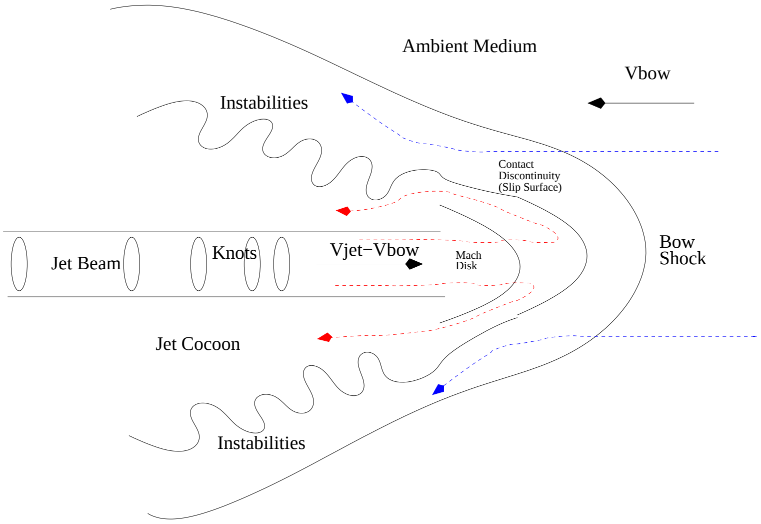

Figure 1-8: *Terminal Working Surface in the rest frame of the shock.*

disk) separated by a contact discontinuity (slip surface). Along the length of the jet variations in the velocity of the source produce internal working surfaces which are thought to be the cause of the Herbig-Haro knots.

In the rest frame of the contact discontinuity, the "shock frame" (see Figure 1-8) the bow shock sees the ambient medium approach it with a velocity V_{bow}. The jet is incident on the Mach disk with velocity $V_{jet} - V_{bow}$. Gas crossing the Mach disk experiences a rapid, unexpected drop in velocity and most of this energy is immediately converted to heat. At some surface between the two shocks, the ram pressures of the colliding fluids balance and there is no net transfer of material. This surface is the contact discontinuity. It is also well described as the "slip surface" since the shocked ambient and jet material slips sideways and out into the cocoon. The jet and ambient matter can have different shear velocities and generate Kelvin-Helmholtz instabilities.

1.4.2 Radiative shocks and "Forbidden" line emission

As incoming material crosses the shock it experiences a rapid increase in density. $\frac{\rho_{postshock}}{\rho_{preshock}} = \frac{\gamma+1}{\gamma-1}$, where gamma is the adiabatic index or ratio of specific heats. For the adiabatic case, $\gamma = 5/3$, the density ratio is 4. For a radiatively cooling shock, γ is effectively lowered and the jump in density can be much greater. The amount of ionisation and excitation due to collisions is significantly increased in the thin dense ionising/exciting layer at the shock front. Radiative transitions which obey the normal electric dipole quantum mechanical selection rules are called "permitted" emission lines. Those which obey the slower magnetic dipole or electric quadrupole rules are called "forbidden" lines. These lines have low transition probabilities (typically 1 s^{-1}) compared to permitted

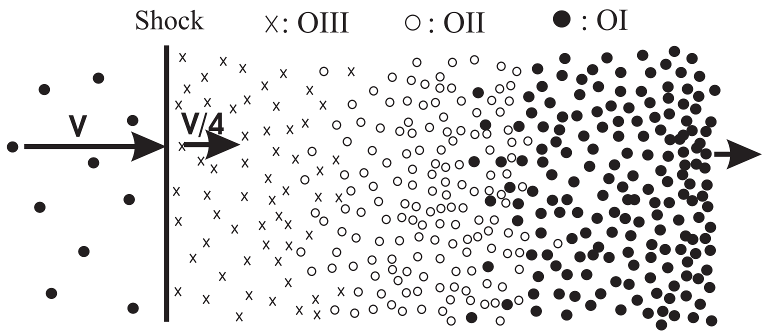

Figure 1-9: *Crossing the shock, there is a rapid increase in density. The density then gradually increases as the thermal energy is radiated away. Shown in the figure are the cooling zones of [OIII], [OII] and [OI].*

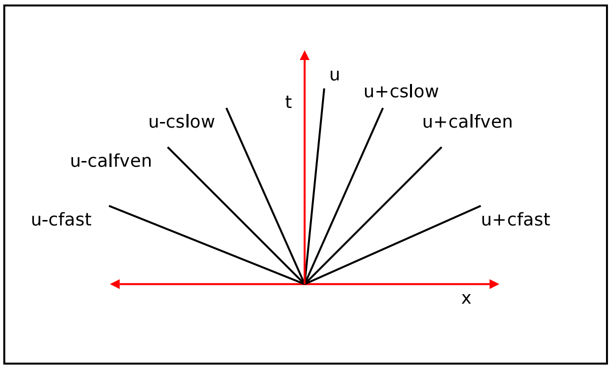

Figure 1-10: *The seven magnetohydrodynamic waves arising from the breakup of a discontinuity in a fluid. The contact wave, u, separates the forward-moving family of slow magnetosonic, Alfvén and fast magnetosonic waves from the backward-moving family.*

lines ((typically 10^8 s^{-1}) Dyson & Williams 1980).

1.4.3 Magnetohydrodynamic shocks

The magnetic field interacts with the fluid through the Lorentz force. The Lorentz force, $\mathbf{j} \times \mathbf{B}$, can be thought of as affecting the dynamics in two different ways.

$$\mathbf{J} \times \mathbf{B} = \frac{1}{\mu}(\mathbf{B} \cdot \boldsymbol{\nabla})\mathbf{B} - \boldsymbol{\nabla}\left(\frac{B^2}{2\mu}\right) \tag{1.5}$$

The first term represents a *magnetic tension* which acts along the magnetic field lines, resulting in a transverse wave mode (Alfvén waves). This is a restoring force analogous to the tension in a violin string. The Alfvén wave speed is $c_A = \frac{B_\perp}{\sqrt{\rho}}$. The second term represents a *magnetic pressure* gradient which can add to or subtract from the ram pressure resulting in the fast or slow

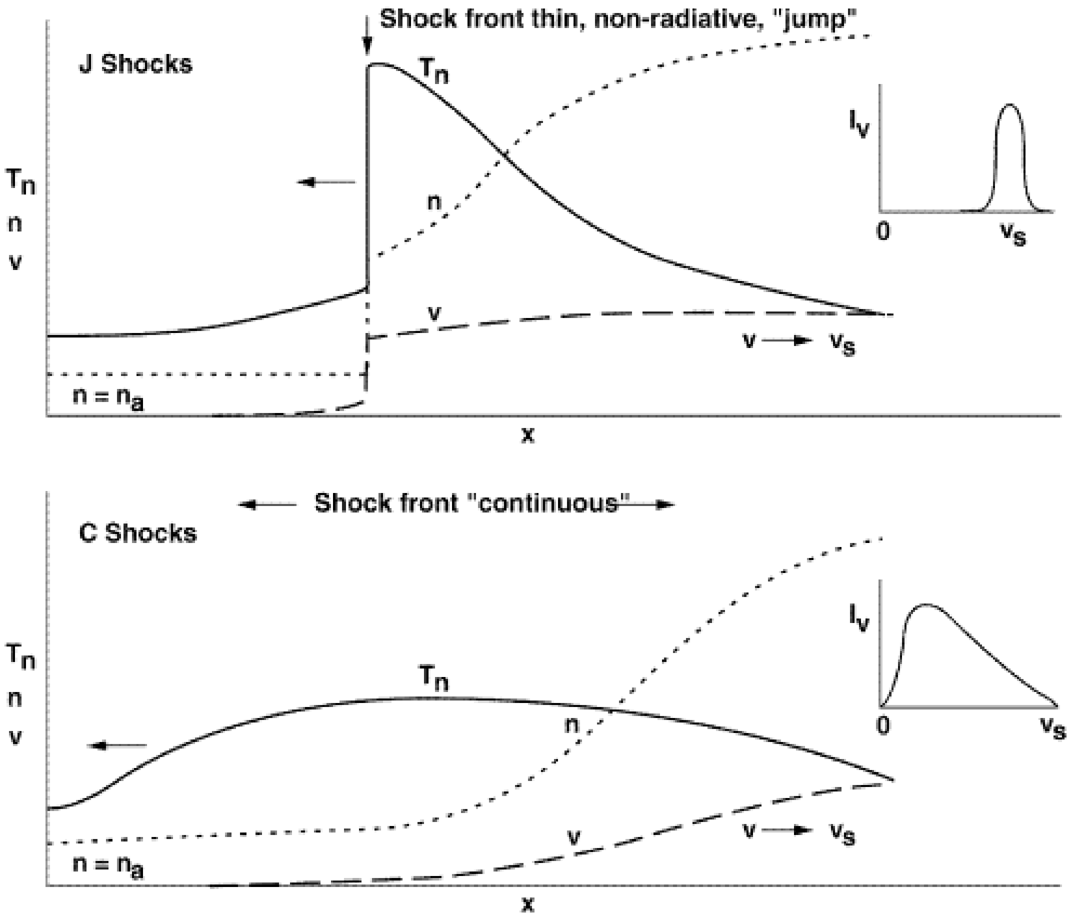
Shock front thin, non-radiative, "jump"
J Shocks
T_n
T_n
n
v
n
v
I_v
0
v_s
$v \rightarrow v_s$
$n = n_a$
x
Shock front "continuous"
C Shocks
T_n
T_n
n
v
n
v
I_v
0
v_s
$v \rightarrow v_s$
$n = n_a$
x

Figure 1-11: *Jump-type Shocks and Continuous-type Shocks , T_n denotes the neutral temperature, n denotes the neutral number density. v denotes the velocity.*

magnetosonic wave modes. This has the same dimensional form as the thermal pressure term in the hydrodynamic equations. Instead of three waves there is a family of seven waves (see Figure 1-10). The contact discontinuity remains the same but the forward and reverse moving waves have each been replaced by the set of slow, Alfvén and fast waves. In a weak or absent magnetic field the Alfvén and slow velocities are zero and the fast velocity collapses to the sound speed.

1.4.4 Jump-type ("J-type") shocks

In a J-shock the velocity is sufficiently high to exceed the Alfvén velocity, hence there is a jump discontinuity in all the state variables.

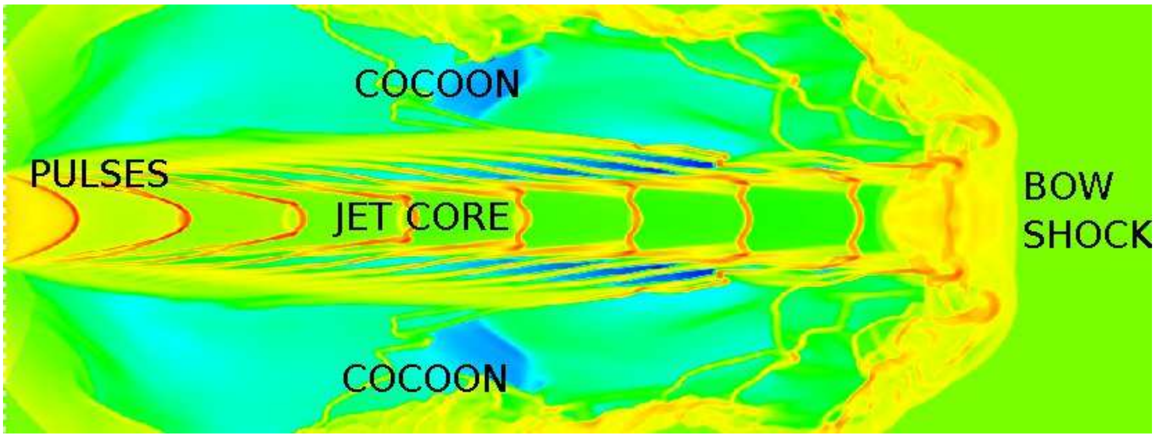

Figure 1-12: *Basic features of a radiatively cooling jet - bow shock, internal working surfaces and cocoon.*

1.4.5 Continuous-type ("C-type") shocks

Mullan (1971) showed magnetised weakly ionised shocks may have continuous solutions for v_S less than a critical value. Draine (1980) introduced the nomenclature "C-type shock" to denote weakly ionised shocks where the ion Alfvén velocity c_A exceeds the shock speed, v_S. In a C-type shock the variables change continuously across the shock, since a magnetic precursor gives the material in the path of the shock time to react to the shock and dissipate its energy smoothly. The magnetic field has a "cushioning" effect; it absorbs some of the incoming momentum. This can occur when the Alfvén speed is higher than the propagation speed. This means that not all material is thermalised when it crosses the shock. But the Wardle instability may cause the C-type shock to be unstable for some modal range of magnetic field perturbations (Stone 1997). See Draine & McKee (1993) for a review article.

1.4.6 Bow shocks and Internal Working Surfaces

At the end of the jet a terminating bow shock is formed where the jet ploughs into the ambient gas around it. Internal working surfaces appear along the length of the jet - they were initially thought to be the crossing shocks which appear in jet simulations. Later they were attributed to velocity variations in the source, which are still of unknown origin. The latter are thought to result from the reconnection of the wound up magnetic field.

1.4.7 Jet diagram

In Figure 1-12, a time-dependent simulation of a radiatively cooling jet is shown. The dense jet material is injected in at the left side of the box and the velocity is varied, causing the internal working surfaces to form. The internal working surfaces develop instabilities as they progress down the jet core and shed vortices adding to the mixing layer in the cocoon. At the front of the jet the terminal working surface or bow shock ploughs into the ambient medium supersonically.

Using a simple one-dimensional approximation, a simple analytic estimate of the bow shock speed is obtained in terms of the jet speed and the ratio of the jet and ambient material densities (assuming ram pressure balanced at the contact discontinuity), which is useful as a simple check on the validity of the numerical simulations. In the rest frame of the working surface, the ambient medium is travelling backwards into the surface at a velocity -W, and the jet is travelling forward at a velocity $v_b - W$. Balancing the ram pressures $\rho_b(v_b - W)^2 = \rho_a\left(-W^2\right)$ leading to $\frac{v_b}{W} = \frac{\sqrt{\eta}}{1+\sqrt{\eta}}$, where $\eta = \rho_a/\rho_b$. Although this is only a two-dimensional simulation, the thin dense shell of material is clearly unstable and already starts to break up. Vortices are shed from the edges of the Mach disk and add to the mixing layer.

1.5 From the kinetic theory to MHD

1.5.1 Boltzmann's Equation

The motions of the gas particles may be described by the Boltzmann kinetic equation.

$$\frac{Df}{Dt} = \frac{\partial f}{\partial t} + \mathbf{v} \cdot \boldsymbol{\nabla}_x f + \mathbf{a} \cdot \boldsymbol{\nabla}_v f = \left(\frac{\partial f}{\partial t}\right)_{collisional} \tag{1.6}$$

where f is the single-particle distribution function in phase space (the probability to find a particle at point $\mathbf{x}$ travelling at $\mathbf{v}$ at a time t), $f(\mathbf{x}, \mathbf{v}, t)d^3xd^3v$ is the number of particles within an interval in phase space at time t. $\mathbf{v}$ is the total velocity (bulk and random components). $\mathbf{a}$ is the acceleration term, which represents the contribution made by external resultant forces such as gravity, $\mathbf{g}$ or the electromagnetic force $\left(\frac{q}{m}\left(\mathbf{E} + \mathbf{u} \times \mathbf{B}\right)\right)$.

Since collisions cannot contribute to the change of quantities such as mass, momentum and energy, whose total is conserved in the collisional process, the left-hand side becomes the collisionless Boltzmann or Vlasov equation.

$$\frac{\partial f}{\partial t} + \mathbf{v} \cdot \boldsymbol{\nabla}_x f + \mathbf{a} \cdot \boldsymbol{\nabla}_v f = 0 \tag{1.7}$$

Substituting $n\langle Q\rangle$ for f, where $\langle Q\rangle = n^{-1}\int Qfd^3v$ gives

$$\frac{\partial n\langle\chi\rangle}{\partial t} + \boldsymbol{\nabla}_x n\langle\mathbf{v}\chi\rangle + n\langle(\mathbf{a}\cdot\boldsymbol{\nabla}_v)\,\chi\rangle = 0 \tag{1.8}$$

where χ represents a conserved quantity such as mass, total energy or momentum.

1.5.2 Moment Equations

In this system, $\mathbf{x}, \mathbf{v}$ and t are all independent variables. In order to simplify the system, velocity, $\mathbf{v}$ may be removed by taking moments of the Vlasov equation. This results in an infinite chain of equations. After taking the zeroth, first and second moments the series may be truncated by the addition of a closure equation or equation of state.

$$\begin{pmatrix} \rho \\ \rho u \\ E \end{pmatrix} = \int \begin{pmatrix} m \\ m\mathbf{v} \\ m\left|\mathbf{v}\right|^2/2 \end{pmatrix} f(\mathbf{x},\mathbf{p},t)d^3v \tag{1.9}$$

1.5.2.1 Zeroth Moment: The Continuity Equation

Taking the zeroth moment, $\chi = m$, gives

$$\frac{\partial\rho}{\partial t} + \boldsymbol{\nabla}\cdot(\rho\mathbf{u}) = 0 \tag{1.10}$$

The familiar continuity equation, expressing the conservation of mass and the fact that it changes in a continuous fashion.

1.5.2.2 First Moment: The Momentum Equation

Taking the first moment, $\chi = m\mathbf{v}$, gives

$$\frac{\partial n\langle m\mathbf{v}\rangle}{\partial t} + \mathbf{v}.\boldsymbol{\nabla}_x n\langle m\mathbf{v}\rangle + n\langle\mathbf{a}\boldsymbol{\nabla}_v.m\mathbf{v}\rangle = 0 \tag{1.11}$$

Dividing $\mathbf{v}$ into bulk and random components $\mathbf{v} = \mathbf{u} + \mathbf{w}$, gives

$$\langle\mathbf{v}\rangle = \langle\mathbf{u}\rangle \tag{1.12}$$

and

$$\langle\mathbf{v}\mathbf{v}\rangle = \langle\mathbf{u}\mathbf{u}\rangle + \langle\mathbf{w}\mathbf{w}\rangle \tag{1.13}$$

$\rho\langle \mathbf{ww}\rangle$ is defined as the pressure tensor. It may be divided into an isotropic gas pressure and a viscous stress tensor. $\rho\langle \mathbf{ww}\rangle = P\overline{\overline{I}} + \overline{\overline{\pi}}$, where

$$P = \rho\frac{1}{3}|\mathbf{w}|^2 \tag{1.14}$$

$$\overline{\overline{\pi}} = \rho\frac{1}{3}|\mathbf{w}|^2 - \rho\langle \mathbf{ww}\rangle \tag{1.15}$$

Assuming the fluid is inviscid $\overline{\overline{\pi}} = 0$.

$$\frac{\partial}{\partial t}(\rho\mathbf{u}) + \boldsymbol{\nabla}_x \cdot \left(\rho\mathbf{u}\otimes\mathbf{u} + P\overline{\overline{I}}\right) + \rho\mathbf{a} = 0 \tag{1.16}$$

This equation describes the conservation of momentum.

1.5.2.3 Second Moment: The Total Energy Equation

Taking the second moment, $\chi = m|v|^2$, gives

$$\frac{\partial}{\partial t}E + \boldsymbol{\nabla}_x\left(\mathbf{u}\left(E+P\right)\right) + \rho\mathbf{ua} = 0 \tag{1.17}$$

The derivation is straightforward, but involves several steps - it is therefore relegated to Appendix B. This equation describes the conservation of energy.

1.5.3 Maxwell's Equations

The $\mathbf{a}$ term contains all the acceleration provided by gravitational and electromagnetic forces. The electromagnetic forces are described by Maxwell's equations.

$$\begin{aligned}
\boldsymbol{\nabla}\cdot\mathbf{D} &= \delta_Q \\
\boldsymbol{\nabla}\cdot\mathbf{B} &= 0 \\
\boldsymbol{\nabla}\times\mathbf{E} &= -\frac{\partial\mathbf{B}}{\partial t} \\
\boldsymbol{\nabla}\times\mathbf{H} &= \mathbf{J} + \frac{\partial\mathbf{D}}{\partial t}
\end{aligned}$$

$\mathbf{H}$ is the magnetic field strength. $\mathbf{D}$ is the electric flux density. δ_Q is the charge density. $\mathbf{B}$ is the magnetic field intensity. $\mathbf{E}$ is the electric field intensity. $\mathbf{J}$ is the current density. $\mathbf{B} = \mu\mathbf{H}$, where μ is the magnetic permeability. $\mathbf{D} = \epsilon\mathbf{E}$, where ϵ is the electric permittivity.

1.5.4 Quasi-Neutral Single Fluid Approximation

In order to solve Maxwell's equations and the equations of fluid dynamics it is first necessary to make the approximations of MHD. The assembly of particles (ions, electrons and neutrals) can be approximated as a fluid, if the mean free path is much smaller than the length scale of interest.

$$\lambda_{mfp} << L_{char} \tag{1.18}$$

Viscosity is assumed to be zero (high Reynolds number)

$$\eta \sim 0 \rightarrow Re =\sim \infty \tag{1.19}$$

The particles are collisionally coupled. The system can be simplified from the multiple fluids (electrons, ions of different species) to a single fluid approach if it assumed that charged particles are coupled to neutrals. The length scale of interest is 10^{15} cm, whereas the mean free path $l = (n\sigma)^{-1}$ is $l = 10^{13}$ cm (for cross-sectional area $\sigma_{csa} = 10^{-15}$ cm^{-2} and $n = 10^{2}$ cm^{-3}). It is further assumed that electrons and ions do not show a Hall separation and that the neutrals do not exert a drag on the charged particles. Assuming quasi-neutrality (the charge density, δ_Q is zero).

$$\delta_Q = 0 \tag{1.20}$$

Due to electrostatic attraction, each charged particle will be surrounded by other oppositely charged particles which will screen it (Debye screening). The radius at which the electrostatic force is negligible is the Debye-Hückel length.

$$L_D^{-2} \equiv \frac{4\pi e^2}{kT}(n_e + {Z_i}^2 n_i) \tag{1.21}$$

1.5.5 Ideal MHD Approximations

Following Jackson (1975), the displacement term in the Ampère-Maxwell law may be neglected,

$$\boldsymbol{\nabla} \times \mathbf{B} = \mu\mathbf{J} + \mu\frac{\partial \mathbf{D}}{\partial t} \tag{1.22}$$

Taking the equations:

$$\boldsymbol{\nabla} \times \mathbf{B} = \mu\mathbf{J} \tag{1.23}$$

$$\boldsymbol{\nabla} \times \mathbf{E} = -\frac{\partial \mathbf{B}}{\partial t} \tag{1.24}$$

Substituting in for $\mathbf{E}$ using Ohm's law $\mathbf{J} = \sigma(\mathbf{E} + \mathbf{u} \times \mathbf{B})$, where $\mathbf{J}$ is the current density and σ is the conductivity (and neglecting along the way the Joule dissipative term and the pressure gradient term from the generalised Ohm's law) - one obtains:

$$\frac{\partial \mathbf{B}}{\partial t} + \boldsymbol{\nabla} \times (\mathbf{B} \times \mathbf{u}) - \frac{1}{\mu\sigma}\boldsymbol{\nabla} \times (\boldsymbol{\nabla} \times \mathbf{B}) = 0 \tag{1.25}$$

For a stationary fluid letting $\mathbf{u} = 0$ and applying $\boldsymbol{\nabla}.\mathbf{B} = 0$ this reduces to

$$\frac{\partial \mathbf{B}}{\partial t} = \frac{1}{\mu\sigma}\boldsymbol{\nabla}^2\mathbf{B} \tag{1.26}$$

- a standard diffusion equation in which the field decay time is as follows:

$$\tau = \mu\sigma L^2 \tag{1.27}$$

and this is effectively infinite (about 10^{10} years) given large scales in astrophysical systems and high conductivity, Hence with high conductivity, magnetic Reynolds number $R_M = V\tau/L$ and magnetic field decay diffusion time are effectively infinite and magnetic lines of force are effectively "frozen" into the fluid. Alfvén's Theorem (1943): "In a perfectly conducting fluid $R_m \to \infty$, magnetic field lines move with the fluid: the field lines are 'frozen' into the plasma." The induction equations is then reduced to just two terms:

$$\frac{\partial \mathbf{B}}{\partial t} + \boldsymbol{\nabla} \times (\mathbf{B} \times \mathbf{u}) = 0 \tag{1.28}$$

This equation implies $\frac{d}{dt}\int_{\mathbf{S}} \mathbf{B}.d\mathbf{S} = 0$ which implies that the flux, $\mathbf{B}$, threading a surface, $\mathbf{S}$, does not change as $\mathbf{S}$ moves through the fluid. See Choudhuri (1998) or many standard texts for a proof of this.

1.5.6 Rankine-Hugoniot Conditions

The ideal magnetohydrodynamics (MHD) equations are a simplified model used to describe the behaviour of a magnetised fluid over time and space. They are coupled non-linear vector differential equations. They express the conservation laws, of mass, momentum, magnetic flux density, and energy. The approximations of MHD break down once in the shocked regime, however the conservation laws still apply. When one applies the conservation laws across a shock, the Rankine-Hugoniot conditions for shocks can be derived. de Hoffmann & Teller (1950) derived the Rankine-Hugoniot jump conditions for the magnetohydrodynamic case.

$$\begin{aligned}
s[\rho] &= [\rho u_x] \\
s[\rho u_x] &= [\rho u^2 + P - \frac{1}{2} {B_x}^2] \\
s[\rho u_y] &= [\rho u_x u_y - B_x B_y] \\
s[\rho u_z] &= [\rho u_x u_z - B_x B_z] \\
s[B_y] &= [u_x B_y - B_x u_y] \\
s[B_z] &= [u_x B_z - B_x u_z] \\
s[E] &= [u_x \left(E + P\right) - B_x \left(\mathbf{v} \cdot \mathbf{B}\right)]
\end{aligned}$$

The Rankine-Hugoniot Jump Conditions, where s is the shock speed, ρ is the density, $u_{x,y,z}$ the velocity components, $B_{x,y,z}$ the magnetic field, E the energy and P = $p_{thermal} + \frac{1}{2}\mathbf{B}^2$ the total pressure. A jump in a quantity is denoted square brackets

$$[x] = x_1 - x_2 \tag{1.29}$$

1.6 Numerical methods for solving equations

The evolution of an astrophysical gas is described by a set of coupled hyperbolic differential equations, the MHD equations. These equations are nonlinear, have no general analytical solution and in most cases must be solved numerically. Numerical solutions can be found using a large number different of schemes. In fact, numerical models are depicting jets in nature more and more accurately as more and more physics can be included (see section 1.6.1). One initial choice that can be made is to solve the equations in a fixed reference frame with a moving fluid (Eulerian) or a moving reference frame (Lagrangian). In many codes, the physical fluid is represented on a grid of cells with values at the cell centres and cell faces. This representation, where the co-ordinate system does not co-move with the fluid is called the Eulerian representation.

Existing schemes span a range of types from simple first-order schemes (e.g. Lax-Friedrichs) which, while perfectly adequate for smooth initial conditions, can smear the solutions of shocked initial conditions so common in modern astrophysical applications, to second-order schemes which often can capture steeper gradients at the expense of numerical oscillations (e.g. Lax-Wendroff), to high-order schemes which attempt to capture shocks with a minimum amount of approximation, to implicit schemes, e.g. Crank-Nicholson, which are computationally intensive and complex but

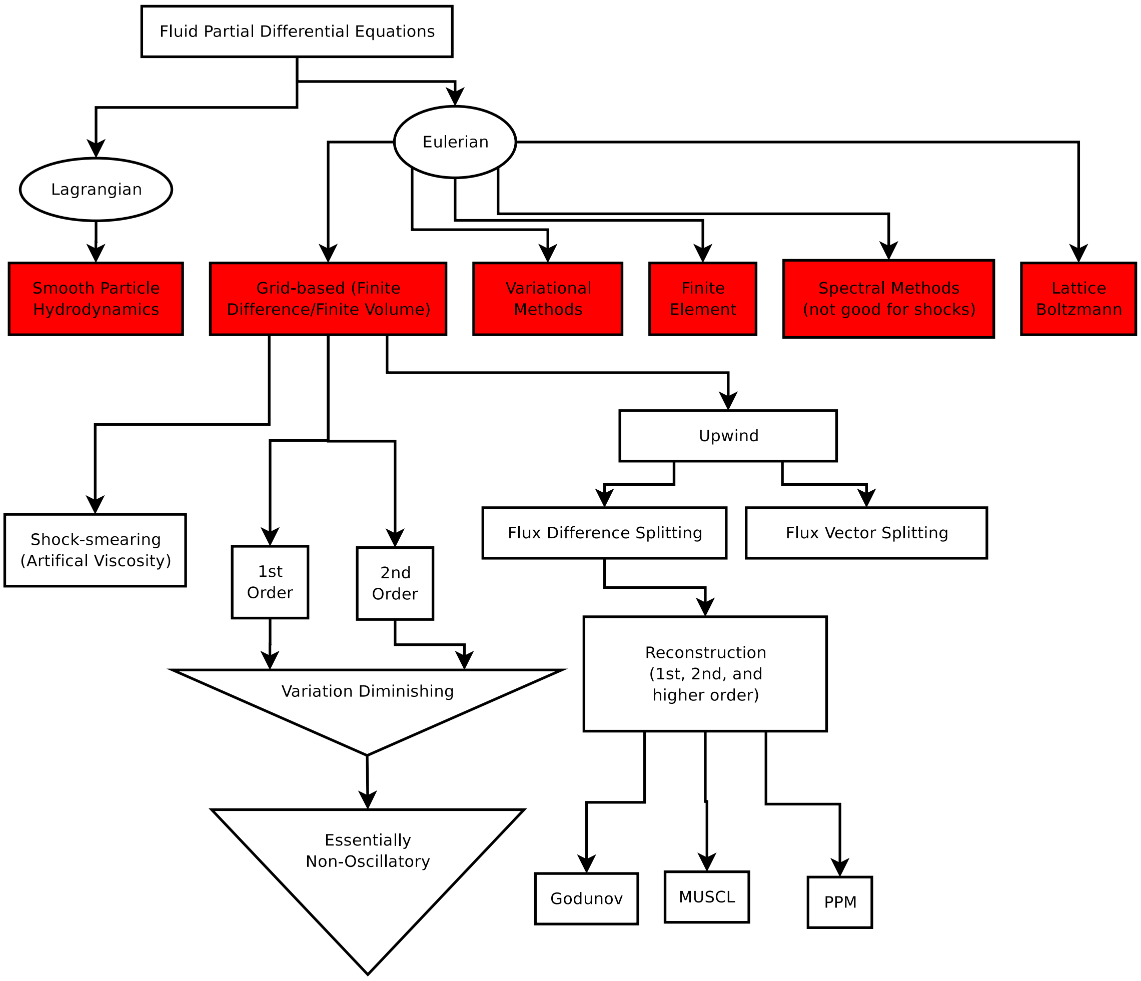
Fluid Partial Differential Equations
Lagrangian
Eulerian
Smooth Particle Hydrodynamics
Grid-based (Finite Difference/Finite Volume)
Variational Methods
Finite Element
Spectral Methods (not good for shocks)
Lattice Boltzmann
Upwind
Flux Difference Splitting
Flux Vector Splitting
Shock-smearing (Artifical Viscosity)
1st Order
2nd Order
Variation Diminishing
Reconstruction (1st, 2nd, and higher order)
Essentially Non-Oscillatory
Godunov
MUSCL
PPM

Figure 1-13: *Numerical methods for solving the fluid partial differential equations*

have stability advantages, to essentially non-oscillatory schemes, finite element, spectral methods, and variational methods.

Shocks are typically represented by steep gradients which, because the equations are non-linear, can cause simple second-order schemes to become rapidly unstable. To avoid instability a scheme based on an analytical solution which does exist is used - the Riemann solution to the shock tube problem. This is a self-similar solution for two uniform states of a fluid. By treating every boundary between two neighbouring cells as a one-dimensional Riemann problem, and solving either analytically or approximately, a solution can be spliced together.

Astrophysical problems on a large scale require a large amount of computational power and an efficient use of limited available facilities. More efficient use of available computational power can be made by concentrating on areas in the computational domain where changes are taking place and neglecting those where the solution is stationary over time. This can be achieved by using an adaptive mesh, which can refine the grid when the gradients become steep (where the physics is changing) and derefine the grid where high resolution is unneeded (where the solution is not changing).

For sufficiently large problems, especially three-dimensional, a single desktop PC is not sufficient to find a solution in a reasonable length of time. Performing a simulation in 3D, with for example 64x64x128 cells, even using adaptive mesh refinement to cut down on number of calculations required already exceeds the specifications of most PCs and requires the use of a parallel machine. Problems must be solved in parallel using a large number of machines, either with a shared-memory architecture or a distributed memory architecture.

1.6.1 History and current state of star formation jet simulations

Numerical models of optical jets have evolved over the past twenty years as the understanding and interpretation of observations increased. Most of the early jet simulations were of extragalactic jets. Early simulations were by Norman et al. (1981) of the Blandford & Rees (1974) twin-exhaust model. These were hydrodynamic slab-symmetric models which displayed the basic features of bow shocks, crossing shocks and cocoons. Pudritz & Norman (1983) and Pudritz & Norman (1986) applied the methods of Norman et al. (1981) to protostellar jets. Magnetic fields were introduced by Clarke et al. (1986). They used a toroidal field and advected the magnetic vector potential rather than the field strength in order to preserve $\nabla \cdot \mathbf{B} = 0$. One of the major physical differences between AGN jets and jets from young stars is the amount of cooling due to atomic and molecular processes. Atomic radiative cooling was introduced by Hartmann & Raymond (1984), Hartigan et al. (1987) and Raymond et al. (1988) using 1.5D bow shock models which explicitly tried to model observed features. Blondin et al. (1990) used an approximation to young stellar object parameters for radiatively cooling jets. A major step forward was made by Brio & Wu (1988) who derived an approximate Riemann solver for MHD. Now Godunov methods could be applied to astrophysical jet simulations. Time variations in the jet velocity were used by Raga et al. (1990) to explain the knots in Herbig-Haro objects. In order to increase the amount of resolution in the physically interesting regions, 2D local adaptive mesh refinement codes were applied to gas dynamics by Falle & Raga (1993) and Klein et al. (1994). Raga et al. (1995) introduced molecular cooling into jet simulations. 3D SPH models were performed by de Gouveia dal Pino & Benz (1993) which were the first jets to be both magnetised and include radiative cooling losses. Lim et al. (1999) added chemical networks for the first time. 3D adaptive mesh refinement codes were applied to gas dynamics by Truelove et al. (1998) and Lim & Steffen (2001). The state of the art jet simulation is now fully three-dimensional, with molecular and atomic cooling, adaptive mesh refinement, magnetic field and sometimes chemical networks and radiative transfer included.

1.7 Structure of this thesis

In this thesis the propagation of magnetised radiative jets from binary sources, and the propagation of jets in evacuated cavities is studied. For these studies a new numerical code is used.

In Chapter 2 the numerical methods used and the numerical code are introduced. In Chapter 3 the code is rigorously tested and compared against the results of other investigators.

In Chapter 4 the binary jet model is explored. Molecular outflows and jets are near ubiquitous in the star formation process. Multiplicity is a similarly identifiable trend as a large majority of stars appear to form in binaries or multiple star configurations. The question is then: why are most outflows not visibly binary outflows? A time-dependent model of a binary jet system can be used to examine the effects of source orbiting, magnetic fields and jet interaction on the morphology and propagation of the jets. Therefore numerical simulations of the two jet model are performed and the MHD parameters are based on observations of a specific object, LDN1551 IRS 5 (HH154).

In Chapter 5 the relationship between a jet and its environment is examined. The propagation of jets in evacuated cavities is investigated. The idea of a density gradient allowing the jet from a protostar to collimate has a venerable history, stretching back to Blandford & Rees (1974), Königl (1982), Fukue (1982), Sakashita et al. (1984), Ferrari et al. (1984) and Okuda & Ikeuchi (1986). Jets are collimated, episodic phenomena which possess a prehistory of outflows moulding the molecular cloud. In the current study a firm connection between a jet and its established prehistoric environment is demonstrated. Herbig-Haro jet phenomena are remarkable for their high velocities and unusually collimated morphologies, extending up to parsec scales with opening angles of $0 - 3°$ (Eislöffel et al. 2000). The physical cause of the collimation is as yet undetermined however major influences may be the environment in the immediate vicinity of the source and the prehistory of multiple episodic outflows from the same source. Close to sources, observations have shown strong energetic emission and strong ionisation, as measured by the ionisation fraction (Bacciotti & Eislöffel 1999). One potential source could be strong shocks due, for example, to recollimation.

Finally, conclusions are drawn and future work is mapped out.

"As a result of these discussions, I developed an intense fear of flows in which contact discontinuities were a possibility"

S.K. Godunov, Reminiscences about difference schemes. J Comp Phys, 153:1-5, 1999

"The first obstacle may be one of sentiment. It is said that in a certain grassy part of the world a man will walk a mile to catch a horse, whereon to ride a quarter of a mile to pay an afternoon call. Similarly, it is not quite respectable to arrive at a mathematical destination, under the gaze of a learned society, at the mere foot pace of arithmetic. Even at the expense of considerable time and effort, one should be mounted on the swift steed of symbolic analysis.
The following notes are written for those who desire to arrive by the easiest route, and who are not self-conscious about the respectability of their means of locomotion."

Lewis F. Richardson, How to solve differential equations approximately by arithmetic, Mathl. Gaz., 12:415-21, 1925.

2

Numerical Method

In this Chapter we present the numerical method used to solve the equations of ideal magnetohydrodynamics. The various numerical methods contained in the code, ATLAS are described, including the method for constraining the divergence of the magnetic field equal to zero, the Godunov method for capturing shocks, the corner transport upwind method for describing multidimensional flows, the atomic radiative cooling losses, the parallel structure and finally the method for adaptively refining the mesh in order to give highest resolutions in regions where shocks occur. A description of the computer cluster, Leda, built to perform some of the calculations in this thesis is given.

2.1 The Equations of Ideal Magnetohydrodynamics (MHD)

The ideal MHD equations are in terms of the eight variables in addition to time t which are conserved in a volume: density ρ, momentum, $\rho\mathbf{u}$, magnetic flux density $\mathbf{B}$ and energy density, E. These equations expressed in conservation form are as follows:

Conservation of Mass:

$$\frac{\partial \rho}{\partial t} + \boldsymbol{\nabla} \cdot (\rho\mathbf{u}) = 0 \tag{2.1}$$

Conservation of Momentum:

$$\frac{\partial}{\partial t}\left(\rho \mathbf{u}\right) + \boldsymbol{\nabla} \cdot \left[\rho \mathbf{u} \otimes \mathbf{u} + \left(p^*\right) \bar{\bar{\mathbf{I}}} + \mathbf{B} \otimes \mathbf{B}\right] = 0 \tag{2.2}$$

Conservation of Flux:

$$\frac{\partial \mathbf{B}}{\partial t} + \boldsymbol{\nabla} \cdot \left(\mathbf{u} \otimes \mathbf{B} - \mathbf{B} \otimes \mathbf{u}\right) = 0 \tag{2.3}$$

Conservation of Energy:

$$\frac{\partial E}{\partial t} + \boldsymbol{\nabla} \cdot \left[\left(E + p^*\right) \mathbf{u} - (\mathbf{u} \cdot \mathbf{B})\mathbf{B}\right] + L_{cooling} = 0 \tag{2.4}$$

where E is the total energy, kinetic, internal and magnetic

$$E = \frac{1}{2}\rho|\mathbf{u}|^2 + \frac{p}{\gamma - 1} + \frac{1}{2}|\mathbf{B}|^2 \tag{2.5}$$

and p^* is the sum of thermal and magnetic pressure:

$$p^* = p + \frac{1}{2}|\mathbf{B}|^2 \tag{2.6}$$

$L_{cooling}$ is the loss of energy due to cooling. The units are chosen so that $\mathbf{B}$ absorbs a factor of $1/\sqrt{4\pi}$. The adiabatic index is $\gamma = 5/3$ for a monatomic gas throughout the simulations. $\mathbf{I}$ is the identity tensor. There are eight equations and nine variables. In order to close the system one more equation is required, the equation of state. The equation of state is chosen to be the ideal gas equation.

2.2 Numerical constraints

There are several constraints imposed on any numerical scheme to produce meaningful physical results. Any numerical scheme must be *consistent* with the original differential equations. It must *converge* upon the analytical result. It must *conserve* energy, momentum and mass. It must be *accurate* to some predefined order of accuracy. Finally the scheme must be *stable*, meaning its numerical errors must be bounded for a fixed timestep. The numerical constraints do not end here, however as the simulation of large-scale multidimensional MHD shocked flows presents several more intricate numerical difficulties. For shocked flow the scheme must also capture shocks correctly (i.e. estimate their speed correctly). The scheme must be *upwind*, by which it is meant that information does not propagate at an unphysical velocity. For magnetised flow it is necessary to explicitly forbid the numerical creation of magnetic monopoles. (This is the well known constraint on the divergence of the magnetic field.) Modelling radiative cooling losses implies reducing the thermal pressure, which can sometimes result in an unphysical negative pressure, as well as a constraint on the timestep, since radiative cooling losses happen on a much shorter timescale than the dynamical timestep. In addition, since large scale, three-dimensional flows are in question, reproducing the physics at a required order of accuracy becomes more computationally intensive. One method for reducing the amount of computations is the use of adaptive mesh refinement.

2.2.1 Shock-capturing Scheme

The astrophysical shocks which manifest themselves in forbidden line emission from optical jets are represented in numerical codes in the form of steep discontinuities. For a scheme with second-order accuracy in space, it is necessary to approximate the spatial derivative. The discrete approximation will usually either overestimate or underestimate the derivatives near discontinuities and this results in unphysical oscillatory patterns somewhat like the Gibbs phenomenon. These oscillations are further amplified on the next timestep (when the derivative is approximated again). Therefore special care needs to be taken near discontinuous solutions. Traditionally there are three methods for dealing with discontinuities which arise in finite difference schemes.

- Shock-smearing (Artificial Dissipation)
- Linear hybrid schemes
- Godunov's method

2.2.2 Shock-smearing – Artificial Dissipative Terms

The addition of artificial dissipative terms was introduced in von Neumann & Richtmyer (1950), in order to "give the shocks a thickness comparable to (but preferably somewhat larger than) the spacing of the points". It models the high-order physical viscosity which causes real shocks to remain steep but smooth over a small distance. However the physical viscosity is a great deal smaller than the artificial viscosity. (There is also a numerical viscosity, since the shock has some finite width thanks to the discrete sampling.) This method has been superseded by more accurate representations of the shocks in the Godunov scheme. It results in unphysical smearing and lack of causality in a solution. However artificial viscosity is still useful to smear the solution on the computational grid. Balsara (1998) lists four good reasons to use (a small amount of) artificial viscosity. These include:

- Smearing the small oscillations due to the presence of a grid with slow strong shocks, as seen in Colella & Woodward (1984).
- The Quirk instability – observed when a strong shock is closely aligned to the grid, produces oscillations of the order of one grid cell perpendicular to the shock propagation direction.
- Turbulence simulations – where noise may affect short length scale structures.
- Grid noise may prevent convergence on a solution when trying to iterate towards a steady state.

2.2.3 Linear hybrid schemes

The idea behind the hybrid scheme is to use a high-order method for smooth regions and a low order method near discontinuities. The two methods are used in a weighted combination where the weight is related to some measure of the variation in the field. This method has been consistently improved from its early implementations. The earliest implementation was in the Flux-corrected transport scheme (Boris & Book 1973). This was later improved into the Total Variation Diminishing scheme (Harten 1983). It was further improved to the Essentially Non-Oscillatory scheme (Harten et al. 1987), and the Weighted Essentially Non-Oscillatory (Liu et al. 1994).

2.2.4 Godunov's Method

The numerical solution of problems involving discontinuities (shocks) is made difficult by the tendencies of high-order schemes to produce spurious oscillations in the region of shocks. In particular Godunov's theorem (Godunov 1959) states that for the linear advection equation there are no schemes of second order accuracy which satisfy the monotonicity condition. Similarly for first order schemes the tendency is to smear the shock wave across a number of cells, attaining monotonicity at the expense of a less accurate reproduction of the solution. (Godunov 1959) exploited the existence of discontinuities in a very physically insightful way. Godunov treated each cell interface as a Riemann problem, where the left and right states are given by the averaged values of theadjacent cells. cells. The key advantage of the Godunov scheme over the other schemes is that is upwind. The explicit computation of the direction of each wave guarantees that no information will propagate backwards in time. The disadvantage of this is that the computation is extremely expensive, far more than a simpler method (e.g. Lax & Wendroff 1960) would be.

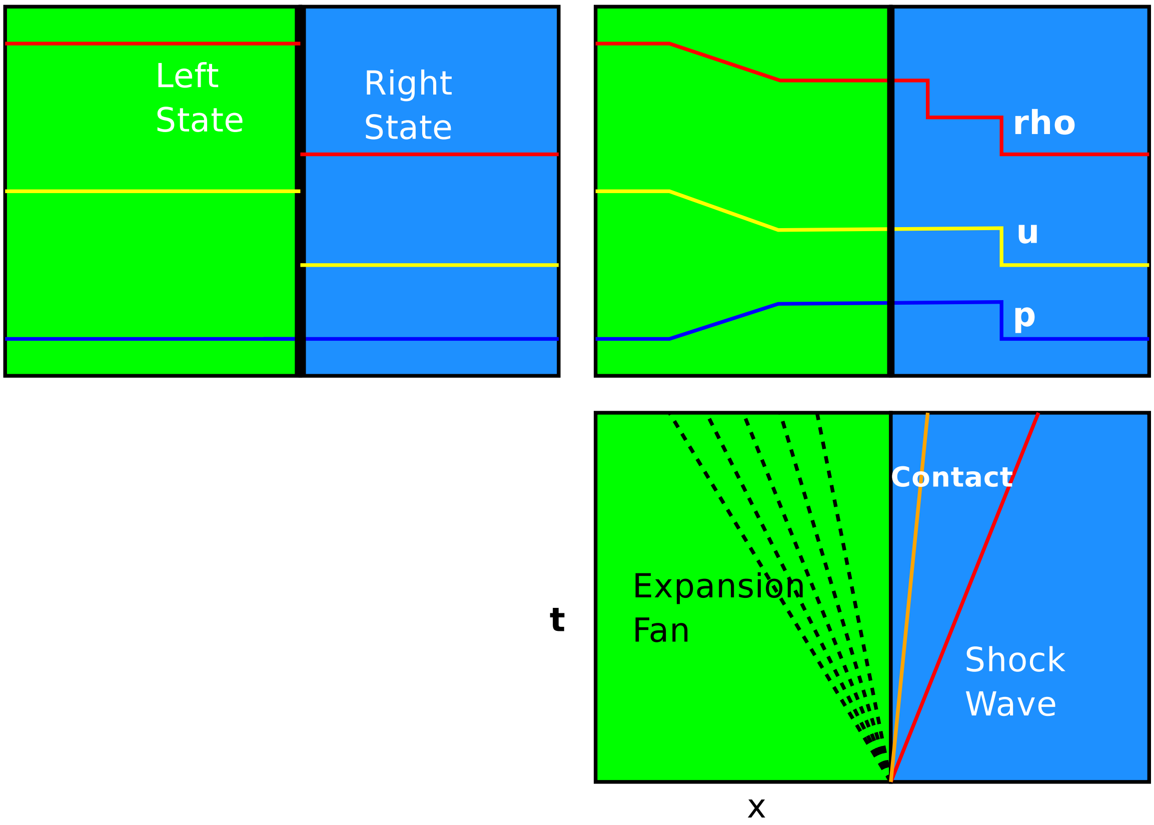

Figure 2-1: *The top two panels show the initial and final states for a purely hydrodynamical one-dimensional shock tube problem. The lower right panel shows the x-t characteristics for the same problem. (Figure from Haque 2006).*

2.2.4.1 The Riemann Problem

The Riemann problem is an initial value problem consisting of two states, “left” and “right” states separated by a discontinuity. Physically it may be pictured as a shock tube, where two gases with different densities and pressures are separated in a chamber by a thin membrane. At a time t, the membrane is removed. The subsequent motion of the gases was calculated by Bernhard Riemann in 1859. The problem has an exact analytical solution for the Euler and MHD equations for physically meaningful input conditions, which may be discovered by calculating the Rankine-Hugoniot jump conditions across the shock. This takes into account the physical direction of propagation of information, thereby ensuring that the solution uses only upwind information.

$$\begin{aligned}
s[\rho] &= [\rho u_x] \\
s[\rho u_x] &= [\rho u^2 + P - \tfrac{1}{2}{B_x}^2] \\
s[\rho u_y] &= [\rho u_x u_y - B_x B_y] \\
s[\rho u_z] &= [\rho u_x u_z - B_x B_z] \\
s[B_y] &= [u_x B_y - B_x u_y] \\
s[B_z] &= [u_x B_z - B_x u_z] \\
s[E] &= [u_x (E + P) - B_x (\mathbf{v} \cdot \mathbf{B})]
\end{aligned} \tag{2.7}$$

Rankine-Hugoniot Jump Conditions. s is the shock speed, ρ is the density, $u_{x,y,z}$ the velocity components, $B_{x,y,z}$ the magnetic field, E the energy and P = $p_{thermal} + \frac{1}{2}\mathbf{B}^2$ the total pressure.

2.2.4.2 Exact Solution of the Riemann Problem

The Godunov method requires that the fluxes across the boundaries be computed. In the hydrodynamic case this can be done exactly. An analytical solution of the nonlinear Riemann problem can be found by applying the Rankine-Hugoniot conditions across the shock. The analytical solution of the MHD equations exists for the nonlinear Riemann problem. The solution is implicit in five unknowns and requires an iterative method to compute the exact solution. Solving the Riemann problem exactly in order to merely determine the fluxes is computationally expensive and wasteful, since the solution is only required at one region (the cell interface). Exact iterative solutions to the Euler Riemann problem may be found in e.g. Toro (1997). Exact iterative solutions to the MHD Riemann problem have been computed by Brio & Wu (1988), Falle et al. (1998).

2.2.4.3 Linearised solution of the Riemann problem

Roe (1981) proposed an alternative approach for the Euler equations. To solve the system:

$$\frac{\partial \mathbf{U}}{\partial t} + \frac{\partial \mathbf{F}}{\partial x} + \frac{\partial \mathbf{G}}{\partial y} + \frac{\partial \mathbf{H}}{\partial z} = 0 \tag{2.8}$$

where $\mathbf{U} = (\rho, \rho u_x, \rho u_y, \rho u_z, E, B_x, B_y, B_z)$ and

and the vectors $\mathbf{F}$, $\mathbf{G}$ and $\mathbf{H}$ are the y and z components of the flux.

$$\mathbf{F} = \begin{pmatrix} \rho u_x \\ \rho u_x u_x + p - B_x B_x \\ \rho u_x u_y - B_x B_y \\ \rho u_x u_z - B_x B_z \\ (E+p)u_x - (\mathbf{u}.\mathbf{B})B_x \\ 0 \\ B_y u_x - u_y B_x \\ B_z u_x - u_z B_x \end{pmatrix} \tag{2.9}$$

$$\mathbf{G} = \begin{pmatrix} \rho u_y \\ \rho u_y u_x - B_y B_x \\ \rho u_y u_y + p - B_y B_y \\ \rho u_y u_z - B_y B_z \\ (E+p)u_y - (\mathbf{u}.\mathbf{B})B_y \\ B_x u_y - u_x B_y \\ 0 \\ B_z u_y - u_z B_y \end{pmatrix} \tag{2.10}$$

$$\mathbf{H} = \begin{pmatrix} \rho u_z \\ \rho u_z u_x - B_z B_x \\ \rho u_z u_y - B_z B_y \\ \rho u_z u_z + p - B_z B_z \\ (E+p)u_z - (\mathbf{u}.\mathbf{B})B_z \\ B_x u_z - u_x B_z \\ B_y u_z - u_y B_z \\ 0 \end{pmatrix} \tag{2.11}$$

$$\frac{\partial \mathbf{U}}{\partial t} + \frac{\partial \mathbf{F}}{\partial \mathbf{U}}\frac{\partial \mathbf{U}}{\partial x} + \frac{\partial \mathbf{G}}{\partial \mathbf{U}}\frac{\partial \mathbf{U}}{\partial y} + \frac{\partial \mathbf{H}}{\partial \mathbf{U}}\frac{\partial \mathbf{U}}{\partial z} = 0 \tag{2.12}$$

Roe decided to linearise the system and solve the linearised version exactly. The Jacobian matrices $\frac{\partial \mathbf{F}}{\partial \mathbf{U}}$, $\frac{\partial \mathbf{G}}{\partial \mathbf{U}}$ and $\frac{\partial \mathbf{H}}{\partial \mathbf{U}}$ are replaced by linearised matrices $\tilde{\mathbf{A}}, \tilde{\mathbf{B}}, \tilde{\mathbf{C}}$ according to some averaging scheme.

$$\frac{\partial \mathbf{U}}{\partial t} + \tilde{\mathbf{A}}\frac{\partial \mathbf{U}}{\partial x} + \tilde{\mathbf{B}}\frac{\partial \mathbf{U}}{\partial y} + \tilde{\mathbf{C}}\frac{\partial \mathbf{U}}{\partial z} = 0 \tag{2.13}$$

If this is accurate enough the exact solution to the nonlinear problem, with its attendant use of iterative solvers to find the roots of the implicit equation, is not required. Although Roe chose an average which returned the exact solution for a shock, it has been found that using the arithmetic average works just as well in many cases. Once this has been done the linearised system can be solved exactly.

The boundary state and therefore the flux on the boundary may be determined by adding the contributions from each linear wave. This can be done in terms of the conserved or primitive fluxes or variables. It is convenient to work in terms of the primitive variables, $\mathbf{P}$.

$$\mathbf{P} = \begin{pmatrix} \rho \\ u_x \\ u_y \\ u_z \\ p \\ B_x \\ B_y \\ B_z \end{pmatrix} \tag{2.14}$$

$$\mathbf{P} = \begin{cases} \mathbf{P_L} + \sum_{\lambda>0} \left(\mathbf{l} \cdot (\mathbf{P_L} - \mathbf{P_R})\right) \mathbf{r} \\ \mathbf{P_R} - \sum_{\lambda<0} \left(\mathbf{l} \cdot (\mathbf{P_L} - \mathbf{P_R})\right) \mathbf{r} \end{cases} \tag{2.15}$$

where $\mathbf{l}, \mathbf{r}$ are the left and right eigenvectors of the linearised matrix, and $\mathbf{P_L}, \mathbf{P_R}$ are the left and right states. This works well in the strictly hyperbolic hydrodynamic case but caution must be exercised for the MHD equations.

$$\lambda = \begin{pmatrix} u - c_f \\ u - c_a \\ u - c_s \\ u \\ u + c_s \\ u + c_a \\ u + c_f \end{pmatrix} \tag{2.16}$$

Unlike the HD equations, the MHD equations are not strictly hyperbolic (Brio & Wu 1988), at umbilic points their eigenvalues are not unique and the solution becomes singular or undefined. In particular in the case when B$_x$=0 and when ${B_t}^2 = {B_y}^2 + {B_z}^2$=0 the eigenvalues may coincide.

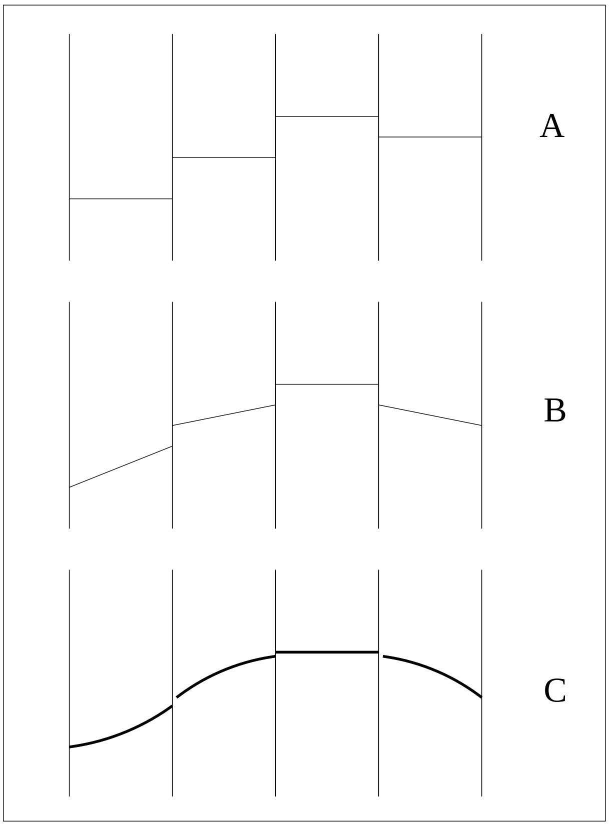

Figure 2-2: *Piecewise-constant, piecewise linear and piecewise parabolic reconstruction of the cell interface values.*

When $|B_x| = 0$ the Alfvén speed $c_a = B_x/\sqrt{\rho}$ is zero, the slow speed collapses to zero and there is a double eigenvalue. When $|B_t|$ is zero the fast speed collapses to the greater of the sound and Alfvén speeds and the slow speed collapses to the other. When $|B_t|$ is zero and the Alfvén speed is equal to the sound speed (the magnetosonic or triple umbilic case) the fast, slow and Alfvén speeds all collapse onto the sound speed. Brio & Wu (1988) found a linearisation for the case $\gamma = 2$. Roe & Balsara (1996) solved the system for an arbitrary value of γ. Falle et al. (1998) pointed out that ordinary gasdynamics may be used to solve at umbilic points.

2.2.5 Reconstruction-Evolution Method

Godunov's original method uses the cell centred values as inputs to the Riemann problem. This loses a lot of information about the original cell structure. Van Leer attempted to recover some of this information by *reconstructing* the cell as a linear function (using the neighbouring cell values). The problem with this is that it introduces new extrema into the solution, so the use of a limiter is required to remove any new extrema. Colella & Woodward (1984) added an extra order of accuracy by approximating the cell interfaces using parabola in the Piecewise Parabolic Method. In PPM, instead of treating a data point as a constant value and having a piecewise constant function, it interpolates between the points using parabola. This gives a more accurate (third-order) description of a smooth gradient than a piecewise constant function (only first-order accurate). It can be summarised in three main steps:

1. It takes an initial sample of the solution at a time t=0 and uses the sample points to reconstruct the left and right states using polynomial reconstruction. In the case of PPM the polynomials are quadratics, for the Piecewise Linear Method the polynomials are first order.
2. The reconstructed left and right states are used as inputs to the Riemann solver, which gives the interface state at time t+dt.
3. The interface states are conservatively differenced to find the average value at the cell centre at time t+dt.

This method is particularly good in one dimension, but loses some of its effectiveness when applied to two are more dimensions, hence a multidimensional correction is applied.

2.2.6 Multidimensional correction: The Corner Transport Upwind method

2.2.6.1 Operator Split Method: Strang splitting

The application of the inherently one-dimensional Riemann solver to a 2 or more dimensional domain leads to the checkerboard instability, where cells become decoupled after the pattern of a chess or checkerboard. There are two main approaches to including directional properties – operator split and unsplit schemes. An operator split scheme solves in each direction sequentially. Such a scheme needs to permute the sequence of directions after every timestep to get rid of a directional bias. In 2D dimensions the solver permutes, x-y, y-x, x-y. In 3D this becomes x-y-z, z-x-y, y-x-z etc. These alternating direction integration schemes are efficient, but because they are directionally operator-split it becomes difficult to enforce a divergence-free magnetic field. This is the major reason for using unsplit schemes. (Strang 1968).

2.2.6.2 Second Order Runge-Kutta

In order to correct for the extra dimension one must include the effects of the diagonal cells. For example, by taking a halfstep in time and working out the fluxes we indirectly include the effects of the diagonal cells which improves the directional properties. This is the Runge-Kutta second order in time scheme. It can be straightforwardly extended to higher order methods.

This method has good directional properties but is merely a composite scheme. It does not explicitly compute the flux contributions travelling at an angle to the grid. The method shows stability problems which become more limiting as the number of dimensions is increased (going from 1D to 2D the maximum stable timestep is decreased by one half and to 3D, by one third. The CFL number is inversely proportional to the dimensionality (can be shown by Von Neumann stability analysis).

The stability problem is rooted in the fact that the numerical domain does not contain the true domain of dependence of the partial differential equation. Waves from the corner cells (see Figure 2-4) are not being included in the solution. In particular the cross-derivative terms (q_{yx} and q_{xy}) in the Taylor series expansion are ignored.

$$q(x,y,t_{n+1}) = q(x,y,t_n)+u\Delta t q_x-v\Delta t q_y+\frac{1}{2}(\Delta t)^2\left[u^2 q_{xx}+uvq_{yx}+uvq_{xy}+v^2q_{yy}\right]+\mathcal{O}((\Delta t)^3) \tag{2.17}$$

2.2.6.3 The Corner Transport Upstream Method

To redress this shortcoming, several methods have been developed including the Weighted Average Flux scheme of Toro (1997), the Corner Transport Upwind (CTU) scheme due to Colella (1990) and the Method of Wave Propagation due to Leveque (1997). These three methods possess a single goal, to compute a properly upwinded flux in more than one dimension.

In higher-order Godunov methods – it is customary to construct a high-order approximation to the cell interface values to be used as inputs to the Riemann problem. The CTU method is no different, and constructs a second-order approximation to the half-state as

$$\begin{aligned} U_{i+\frac{1}{2}}^{n+\frac{1}{2}} &= U_i^n \pm \frac{\Delta x}{2}\frac{\partial \mathbf{U}}{\partial x}+\frac{\Delta t}{2}\frac{\partial \mathbf{U}}{\partial t} \\ &= U_i^n \pm \frac{\Delta x}{2}\frac{\partial \mathbf{U}}{\partial x}-\frac{\Delta t}{2}\left(\frac{\partial \mathbf{F}}{\partial x}+\frac{\partial \mathbf{G}}{\partial y}\right) \\ &= U_i^n + \left(\pm\frac{\Delta x}{2}-\frac{\Delta t A}{2}\right)\frac{\partial \mathbf{U}}{\partial x}-\frac{\Delta t}{2}\frac{\partial \mathbf{G}}{\partial y} \end{aligned} \tag{2.18}$$

It can be seen that in the approximation to the interface state has a contribution from both the x and y directions. The spatial derivative of the conserved flux, $\frac{\partial \mathbf{U}}{\partial x}$, may be approximated using either a central difference or a characteristic tracing. The transverse flux correction, $\frac{\partial \mathbf{G}}{\partial y}$, is computed using a Riemann solver. The transverse flux correction correspond to the contribution from the corner cells in Figure 2-4.

The corner transport upwind method has four steps.

1. Calculate approximations to the spatial derivative of the conserved variables, $\frac{\partial \mathbf{U}}{\partial x}$.
2. Construct left and right states at cell interfaces.
3. Solve the Riemann problem at cell interfaces.
4. Compute the time-updated state by straightforward conservative differencing.

The CTU method has better stability properties than the Runge-Kutta method. However it does come at a price, it computes many more Riemann problems per timestep than other methods. Each cell face requires four Riemann solves in 3D so twelve in total per cell. For an operator split-scheme only three Riemann solves per cell are required.

2.2.7 Satisfying and maintaining $\boldsymbol{\nabla} \cdot \mathbf{B} = 0$

The MHD equations include $\boldsymbol{\nabla} \cdot \mathbf{B}$ in their source terms. As these terms are analytically zero they are often omitted from the computation. Numerically, however, the field may be divergent and monopoles appear in the solution if the constraint equation is not explicitly imposed. One of the most challenging problems for an MHD code is the preservation of $\boldsymbol{\nabla} \cdot \mathbf{B} = 0$, which if not strictly maintained to machine accuracy can generate unphysical extra forces. There are four different approaches: advecting the magnetic vector potential, using a staggered mesh, Hodge projection method (and a Poisson solver), or the Powell method, which consists of adding an eighth wave to advect $\boldsymbol{\nabla} \cdot \mathbf{B} = 0$. All these methods have advantages and disadvantages. Advecting the magnetic vector potential is not useful in this context as it is not a conserved quantity and cannot be used for example with a Riemann solver. In addition it requires an extra spatial derivative (to compute $\mathbf{B} = \nabla \times \mathbf{A}$) reducing the order of accuracy of the solution by at least one. The Powell et al. (1999) method is based on idea of Godunov (1972) to convert the non-strictly hyperbolic MHD system to strict hyperbolicity using the concept of an imaginary eighth wave which advects the quantity $\boldsymbol{\nabla} \cdot \mathbf{B}$ at the velocity of the flow. The idea is that monopoles of positive and negative values are created in equal quantities and annihilate each other. Dedner et al. (2002) extends this scheme to advect the $\boldsymbol{\nabla} \cdot \mathbf{B}$ wave at the fast magnetosonic velocity, i.e. the fastest velocity available. The Poisson solver method simply computes a pseudo-potential "correcting scalar field" and subtracts the gradient of this field from the offending magnetic field components. This also produces a divergence free magnetic field. It is computationally expensive. The most elegant solution is the explicit use of Stokes' theorem to constrain the $\nabla \cdot \mathbf{B}$ to machine accuracy. $\nabla \cdot \mathbf{B} = 0$ is preserved using a staggered mesh algorithm (Balsara & Spicer 1999).

The divergence-free constraint is enforced by using a difference form of Stokes' theorem to advect the field:

$$\frac{\partial \phi_S}{\partial t} = \int_{\partial S} \mathbf{v} \times \mathbf{B} \cdot \mathbf{dl} = \int_{\partial S} \mathcal{E} \cdot \mathbf{dl} \tag{2.19}$$

In difference form the equation is

$$\frac{\partial \Phi}{\partial t} = -\mathcal{E}_{y,i,j}\delta y - \mathcal{E}_{z,i,j}\delta z + \mathcal{E}_{y,i,j}\delta y + \mathcal{E}_{z,i,j+1}\delta z \tag{2.20}$$

$$\frac{\delta \Phi_x}{\delta t} = -\mathcal{E}_{z,i,j}\delta z + \mathcal{E}_{z,i,j+1}\delta z \tag{2.21}$$

$$\frac{\delta \Phi_y}{\delta t} = +\mathcal{E}_{z,i,j}\delta z - \mathcal{E}_{z,i+1,j}\delta z \tag{2.22}$$

$$\frac{\delta \Phi'_x}{\delta t} = +\mathcal{E}_{z,i+1,j+1}\delta z - \mathcal{E}_{z,i,j+1}\delta z \tag{2.23}$$

$$\frac{\delta \Phi'_y}{\delta t} = -\mathcal{E}_{z,i+1,j+1}\delta z + \mathcal{E}_{z,i+1,j}\delta z \tag{2.24}$$

The expressions for $\frac{\delta \Phi'_x}{\delta t}$, $\frac{\delta \Phi'_y}{\delta t}$, $\frac{\delta \Phi_x}{\delta t}$ and $\frac{\delta \Phi_y}{\delta t}$ all sum to zero, indicating that the total flux is conserved over time. The above equations when divided by area give an advection scheme for the flux density which preserves the divergence free condition. This guarantees that the *time changes* in the flux will be numerically divergence-free.

In order to ensure that the initial field is non-divergent, $\mathbf{B}$, the magnetic field strength is computed from the curl of the magnetic vector potential $\mathbf{A}$, by definition $\mathbf{B} = \nabla \times \mathbf{A}$, which has no divergence by the vector identity $\nabla \cdot (\nabla \times \mathbf{A}) = 0$.

2.2.8 Modelling the Microphysics of Atomic Radiative Cooling

Protostellar jets are strongly cooled by optically thin radiation emitted in the high-temperature post-shock regions. Calculating radiative electron transitions directly is not feasible in the fluid approximation. Raga et al. (1997) identify three commonly-used approximations to the inclusion of radiative effects:

1. Assume equilibrium (Raga & Bohm 1987)
2. Non-equilibrium fully ionised (Blondin et al. 1990)

3. Non-equilibrium explicitly computed ionisation fraction (Falle & Raga 1995)

The third approach is used in the current work. The ionisation equation is:

$$\frac{\partial \rho x_e}{\partial t} + \boldsymbol{\nabla} \cdot (\mathbf{v} \rho x_e) = \rho^2 \frac{X_H}{m} \left[x_e (1 - x_e) \alpha(T) - {x_e}^2 \beta(T) \right] \tag{2.25}$$

where x_e is the ionisation fraction, X_H is the hydrogen abundance, m is the average particle mass, $\alpha(T)$ and $\beta(T)$ are the collisional ionisation and radiative recombination terms, and the other symbols have their usual meanings.

$$\alpha(T) = K_I T^{\frac{1}{2}} exp\left(-1.579 \times 10^5 T\right) \tag{2.26}$$

$$\beta(T) = K_R T^{-0.7} \tag{2.27}$$

$K_I = 6.417 \times 10^{-11}$ cm^3 s^{-1} K$^{-1/2}$ and $K_R = 2.871 \times 10^{-10}$ cm^3 s^{-1} K$^{0.7}$ are the collisional ionisation and radiative recombination rate coefficients (Falle & Raga 1995). [1]

The microphysics of energy lost due to radiative cooling is represented using a cooling function adapted from Sutherland & Dopita (1993) and depicted in Figure 2-6, which represents on a macroscopic scale the rate of energy loss at this temperature range for solar abundances. Sutherland & Dopita (1993) include the effects of electron collisional ionisation, radiative and dielectronic recombination and line radiation within their cooling function.

Cooling models the physical process where energy is dissipated. $L_{cooling}$ represents the cooling function in the conservation of energy equation.

$$\frac{\partial E}{\partial t} + \boldsymbol{\nabla} \cdot \left[(E + p^*) \mathbf{u} - (\mathbf{u} \cdot \mathbf{B}) \mathbf{B} \right] + L_{cooling} = 0 \tag{2.28}$$

As can be seen from Figure 2-6, the loss of energy due to cooling depends on temperature in a highly non-linear fashion. It represents several energy losing and gaining processes happening at atomic level in the fluid. There is no simple mathematical function which can concisely represent these processes.

Figure 2-7 contrasts 2D slab-symmetric jets with and without atomic radiative cooling. The jet morphology is entirely different; the cooled jet bow shock is much more irregular, as it has lost a lot of supporting thermal pressure. The propagation velocity of the jet is also lowered (consistent with the jet losing energy, Blondin et al. (1990)).

$$\frac{\partial E}{\partial t} = \frac{\partial F}{\partial x} + L_{cooling} \tag{2.29}$$

---

[1] Note that the recombination rate is incorrectly quoted in Falle & Raga (1995).

The cooling function tracks the rate of energy loss with temperature. It is possible to simply calculate the temperature value at each timestep and read off the rate of energy loss from the look-up table. However in general the cooling function is not smooth and in fact it changes quite rapidly. The timestep if limited by the cooling will become quite short and the solution will become diffusive. Since the cooling is localised at or near shocked regions the operator-split approach is extremely effective.

$$E^{t+dt} = E^t + \frac{\partial F}{\partial x}\Delta t + \int_t^{t+dt} L_{cooling}.dt \tag{2.30}$$

2.3 An MHD 3D numerical code: ATLAS

ATLAS is a new modular shock-capturing, multi-dimensional, staggered-mesh, adaptive-grid, directionally split, higher-order Godunov astrophysical MHD code, which uses a linearised Roe-type MHD Riemann solver. It was written by Daniel S. Spicer and Stephen O'Sullivan at the NASA Goddard Space Flight Center. ATLAS uses several leading alternative high-order Godunov schemes, including a scheme, MUSCL (van Leer 1979) modified to direct Eulerian form by Colella & Woodward (1984), a second-order scheme, the piecewise linear method (PLM) and a third-order scheme, the piecewise parabolic method (PPM; Colella & Woodward 1984).

2.3.1 Parallelisation

ATLAS/PARAMESH uses the SPMD (Single Program Multiple Data) approach. Each processor can access a copy of the same program but has its own separate data block to work on. Information at the boundaries of each block is stored in temporary guard/ghost cells. These represent an overhead in memory and CPU time. PARAMESH takes care of most of the interprocessor communication, by dividing the data up into blocks organised into a hierarchical tree. The blocks are divided among the available processors using a Morton ordering scheme – this ensures that neighbouring blocks are located on nearby processors. At every timestep, the blocks are redistributed among the processors which ensures that the load is efficiently balanced. By adjusting the amount of blocks on each processor and the size of each block, a crude measure of control over the scaling of the problem may be obtained. Simulations were carried out using the ATLAS code on a 64 node hyper-threaded "Beowulf"-type cluster. (Theoretical peak performance 150 GHz.) The individual nodes on the cluster were 16 2.66 GHz dual processors with hyper-threading enabled – a total of four processors, two real, two virtual. Shared memory was enabled on each node.

2.3.2 Achieving Higher Resolution using Adaptive Mesh Refinement

Simulations are by their nature only an approximation to reality. To get closer to the real physics it is necessary to keep increasing the precision. Infinite precision would require an infinite number of computers, so we compromise by only requiring high precision in areas where the physics needs to be well followed. In the case of shock physics, the shocked regions require the highest precision and other regions where changes take place slowly and smoothly require lower precision. A uniform high resolution or refinement is therefore a waste of limited and precious computing resources. A method of Adaptive Mesh Refinement (AMR) is used due to (Berger & Oliger 1984; Berger & Colella 1989), which allows the refined region to move with the shock. There are several methods for determining whether it is necessary to refine or not. One can refine

- if the cell value is over a threshold.
- By measuring the gradient of the solution, if it exceeds a predefined tolerance value the mesh is refined.
- Richardson Truncation Error Estimation – taking a short timestep at both the higher and lower levels and if the difference exceeds a certain tolerance, refining

In the wake of the shock the rest of the grid can use a lower level of resolution (derefine) and thus save on computing power. ATLAS uses a library implementation of adaptive grids, PARAMESH, (MacNeice et al. 2000) which is block-based – the domain is partitioned into blocks of cells which are refined and derefined according to the amount of activity within the block. The mesh itself is structured – cells do not change orientation or area. The co-ordinate system is Cartesian. The adaptive grid methods used in PARAMESH represent several simplifications from the original method of Berger & Oliger (1984); Berger & Colella (1989) by disallowing change of orientation, overlapping, arbitrary shaping and merging. The justification for these changes is the simpler hierarchical structure which simply bisects grid blocks in each direction when refinement is required (DeZeeuw & Powell 1993).

2.4 Leda, a parallel cluster

In order to be able to run these simulations, Stephane Dudzinski at the Dublin Institute for Advanced Studies and I built Leda, a parallel Beowulf-type cluster from computer parts. The 16 dual-processor machines were hyperthreading enabled on each processor, which meant that the cluster

Nodes	*Memory*	*Speed*
Worker	512 MB	2.66 GHz
Master	512 MB	2.4 GHz

Table 2.1: *Nodes on the Leda cluster*

had in total 64 processors. The specifications are shown in Table 2.1. Linux software was installed and message-passing software (the mpich package) was set up to allow communication between the nodes. A gigabit star-topology ethernet connection was used to connect the nodes. This cluster was used for much of the 1D and 2D simulation work in this thesis and also for the extinction mapping of the galactic plane. Large-scale parallel simulations were done on the IBM SP5 in CINECA, the Irish Centre for High End Computing (ICHEC) Bull cluster “Hamilton” and the ICHEC Opteron cluster “Walton”, the Trinity College High Performance Computing machine, and the “Rowan” EM64T cluster in University College Dublin. Grid-based simulations were performed at 18 sites around Ireland using the Grid-Ireland system.

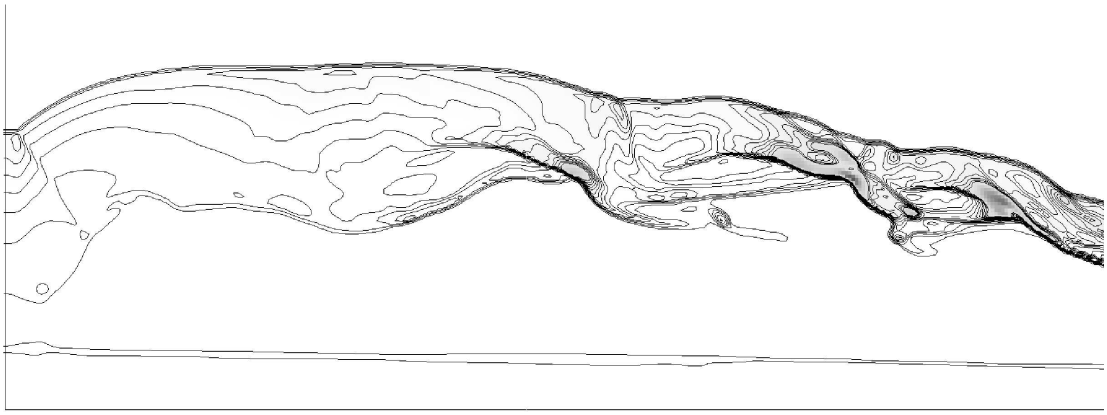

Figure 2-3: *Isopycnics for 300 km* s^{-1} *purely hydrodynamic jet with atomic radiative cooling at* $t = 317$ *years. The adiabatic atomic jet has a bow shock which has been broken up by cooling – causing loss of pressure which erodes the bow shape.*

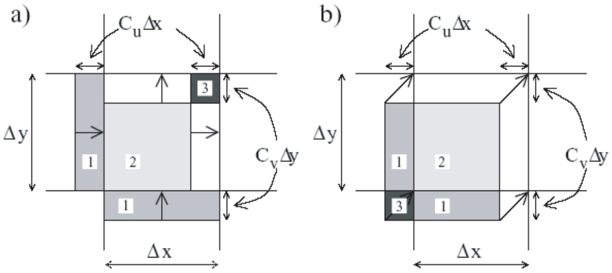
a)
b)
$C_u\Delta x$
$C_v\Delta y$
Δy
Δx
1
2
3

Figure 2-4: *A depiction of the corner transport upwind method for the advection equation in two dimensions. Using the method shown in the left panel results in the south west cell being unrepresented in the flow.*

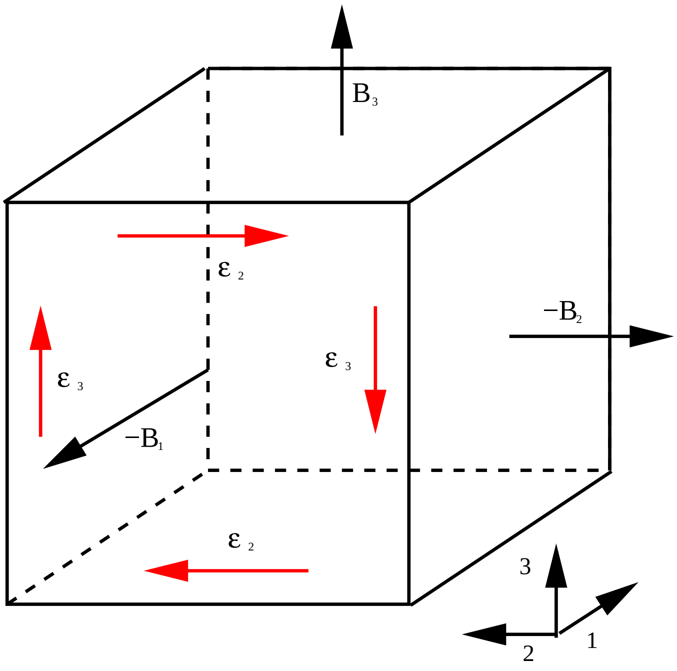
B_3
ε_2
ε_3
$-B_2$
$-B_1$
ε_3
ε_2
3
2
1

Figure 2-5: *The constrained transport method relies on the explicit use of Stokes' theorem, (Faraday's law), taking the path integral of the electric field, $\mathcal{E}$, around the closed contour, in this case the cell face shown by red arrows in the diagram.*

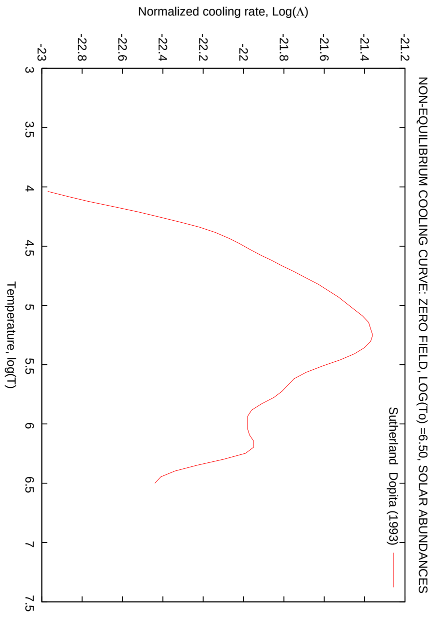

Figure 2-6: *Log normalised radiative cooling loss* Λ*, where* $L_{cooling} = \rho^2\Lambda$ *plotted against log temperature Sutherland & Dopita (1993).*

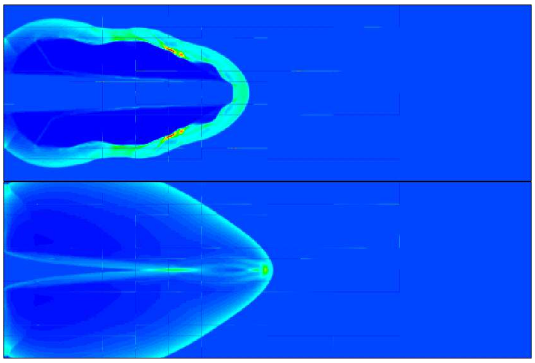

Figure 2-7: *Density comparison of 2D slab-symmetric jet propagating with cooling turned off (lower panel) and on (upper panel). Jet velocity = 300 km/s. Density, 120 cm*$^{-3}$*, temperature 1000 K. The jets are density and pressure matched to the ambient medium. Note the slower speed of the cooled jet, the distortion of the bow shock, and the shape of the core of the jet.*

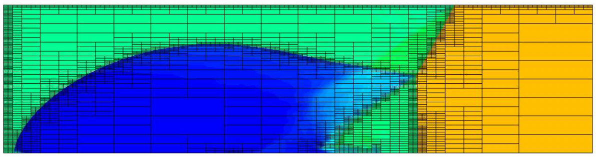

Figure 2-8: *7 levels of adaptive mesh refinement for a 2D integration.*

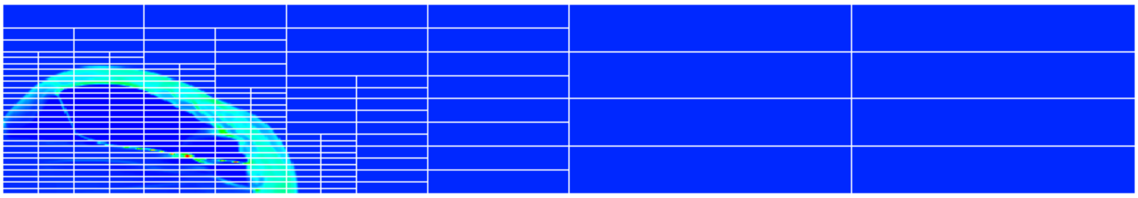

Figure 2-9: *Adaptive Mesh Refinement Example; this is an early stage of a 2D cylindrical symmetric jet simulation. Four levels of refinement are visible. The individual cells are not shown as they obscure the image - shown instead are the boundary boxes each of which bounds* 10x30 *cells.*

“Even though the computer code may be free of error to the extent that it operates exactly as its author intended, it is seldom possible to give a rigorous proof that these intentions were correct.”

P.L.Roe, Ann. Rev. Fluid Mech. 1986 18:337-65

3

Numerical Tests

In this Chapter the method for testing the performance of the code against experimental data and standard tests from the literature is outlined. The various tests are described. These include tests for problems in pure hydrodynamics and magnetohydrodynamics in one and two dimensions, also a test for the perfomance of the radiative cooling algorithm in the code. The code comparison between ATLAS and the PLUTO code for problems relevant to astrophysics is also described.

3.1 Introduction

It is not possible to ensure that any numerical code will provide a meaningful physical solution with arbitrary input but it is possible to establish confidence by *verifying* numerical calculations against

- experimental results
- analytical solutions
- results of other numerical calculations.

The process of *verification* is informally defined as “solving the equations right” (Roache 1976).

	HD	Cooling	MHD
1D	Shock Tube	Overstable Shock	Shock Tube
2D	Mach Reflection Blast	Jet -	Orszag Tang Blast

Table 3.1: *A Test Matrix for Shock-capturing codes*

The complementary procedure of *validation* is defined as “solving the right equations” (Roache 1976). A suite of standard tests has been built up over the past history of computational physics. Sod (1978) compiled a set of tests for 1D HD shocks. Chevalier & Imamura (1982) tested radiative cooling. Brio & Wu (1988) extended Sod’s work to include MHD. Toro (1997) extended Sod’s work to more exacting tests of HD shock-capturing. Ryu & Jones (1995) performed tests for multidimensional MHD flow. Toth & Odstrčil (1996) performed algorithm comparisons for HD and MHD problems. Dai & Woodward (1998) tested their algorithm in one and two dimensions. Liska & Wendroff (2003) provided more tests in 2D HD. The most important features of the ATLAS code are how it handles HD and MHD shocks in all directions, with and without radiative cooling. To test this, the following tests are implemented; shock tube tests, the overstable radiative shock, the double Mach reflection test and the Orszag-Tang vortex are implemented. Finally a code comparison is made with the astrophysics code PLUTO (Mignone et al. 2004). In Table 3.1 we show a test matrix for ATLAS.

3.2 HD Tests

3.2.1 One-dimensional Shock Tube

All shock tube tests were carried out using a grid of 500 cells in size, a Courant number of 0.5 and an adiabatic index of $\gamma = 5/3$. This test was taken from Laney, contains an expansion fan which is a good test of the Roe Riemann solver, a contact discontinuity and a shock.
Left State:

$$U_L = (\rho = 1, v_x = 0, v_y = 10, p = 20) \tag{3.1}$$

Right State:

$$U_R = (\rho = 1, v_x = 1, v_y = -10, p = 1) \tag{3.2}$$

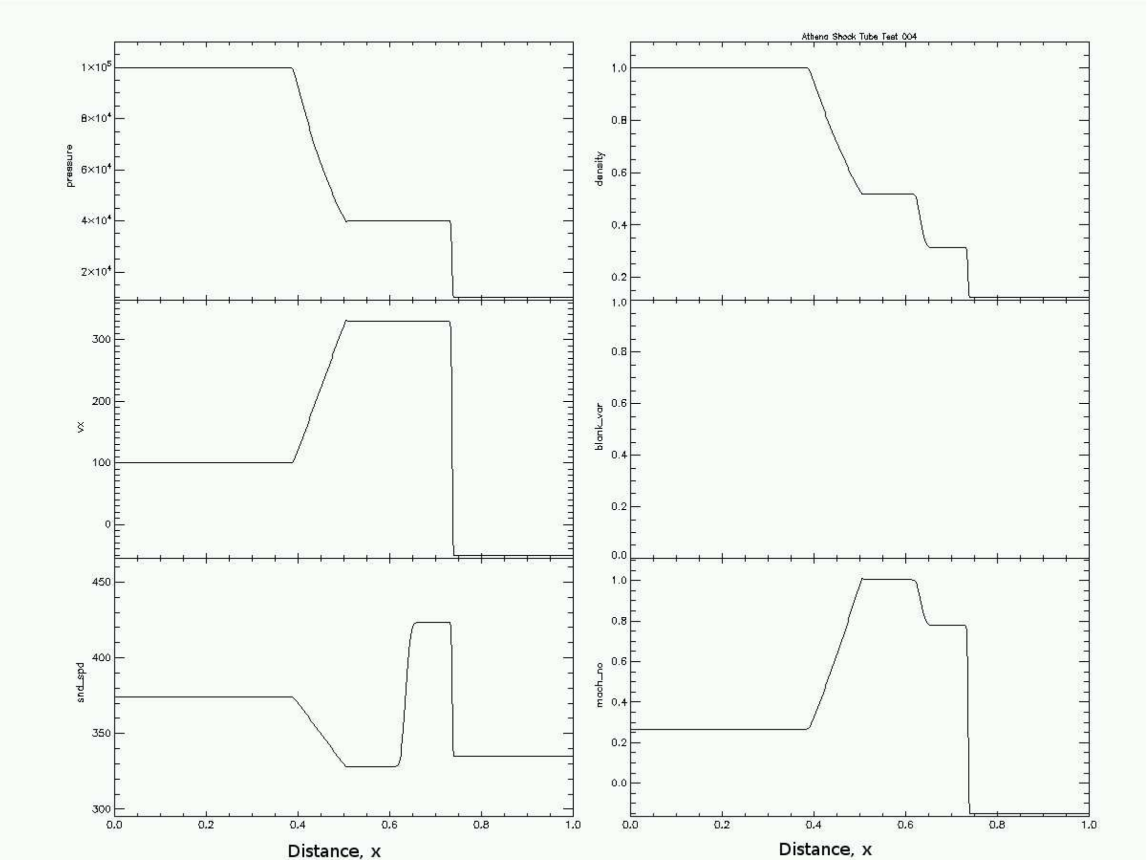

Figure 3-1: *Results of one-dimensional HD shock tube test at time t=0.8 for comparison with Laney (1998) Left panels show pressure, velocity, and sound speed. Right panels show density, entropy and Mach number. The simple features of the expansion fan, contact discontinuity, and shock have all been captured.*

3.2.2 Blast Wave

Pure hydrodynamic blast wave test for comparison with Londrillo & Del Zanna (2000, hereafter LDZ). This test has as its initial conditions a high pressure region in the centre of a plane. The results are shown in Figure 3-2. Here the important features are symmetry, correct wave speed evaluation, well-resolved shocks and preservation of the shape of the circular blast wave.

3.2.3 Double Mach Reflection (DMR) Test

3.2.3.1 Initial Conditions

A strong shock incident on reflecting wedge at an angle greater than the critical angle ϕ_{crit} will separate into a parallel component and a convex reflected component. The three shocks, (incident,

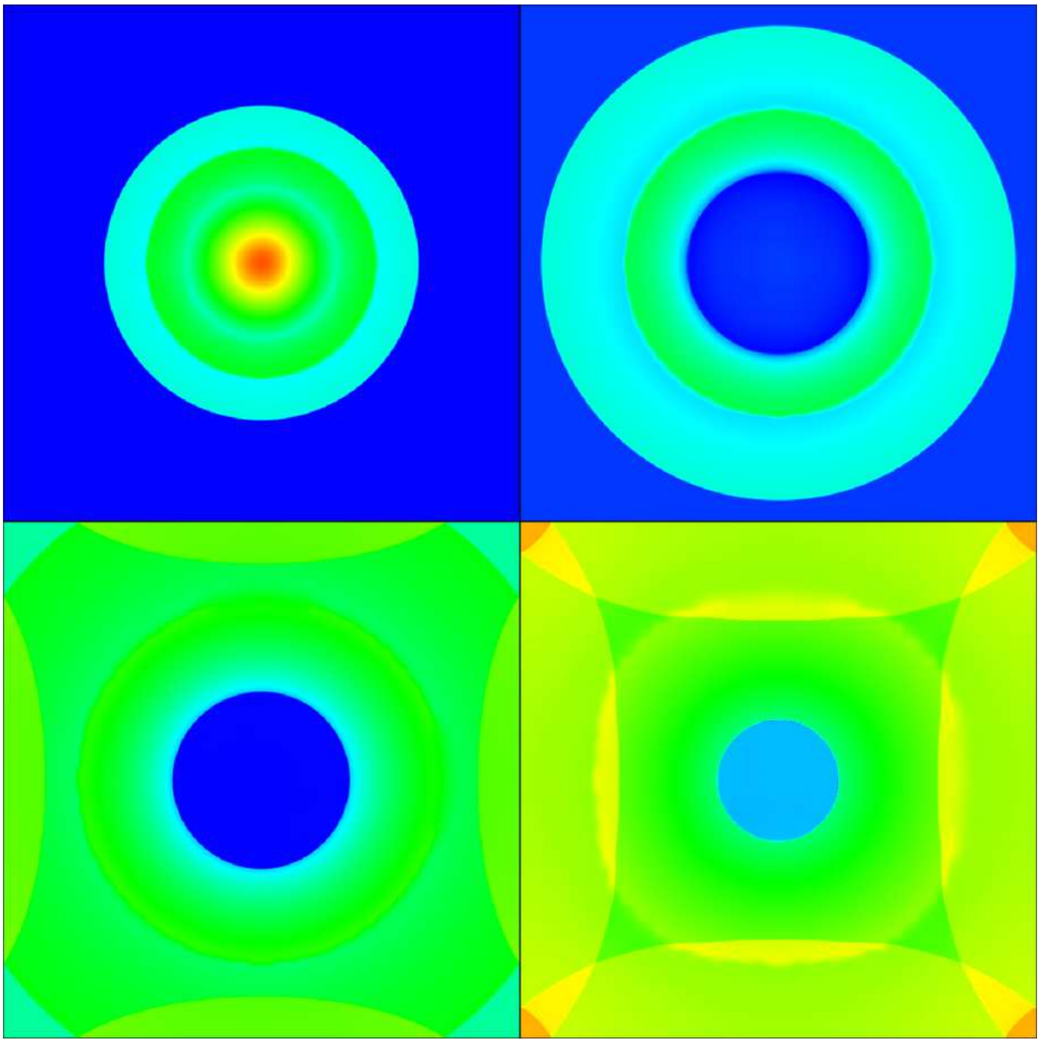

Figure 3-2: *The most important feature of the 2D blast wave test is its perfect symmetry. The shock is also well-resolved. Density colourmaps at times: t=3, 6, 9, 12. The units are arbitrary.*

parallel and reflected) meet at a point called the triple or lambda point (Landau & Lifshitz 1959). (The figure is thought to resemble the lower-case Greek letter lambda.) The complicated non-linear reflection and Mach stem formed during the double Mach reflection of a strong shock plus the Kelvin-Helmholtz instabilities which form along the contact discontinuity provides a challenging problem for the numerical code. It can be reduced to three parameters, γ, the adiabatic index, M, the Mach number and α, the angle of the wedge. Mach reflection has originally studied by Mach in 1878, by von Neumann in 1943 and has been the subject of much experimental work. Woodward & Colella (1984) introduced the DMR test to the literature. The test has since become standard for 2D HD shocks e.g. in Toth & Odstrčil (1996); Stone & Norman (1992), also to test AMR-based codes (Berger & Colella 1989). It models a strong (Mach 10) shock striking a wedge at a 60° angle. The

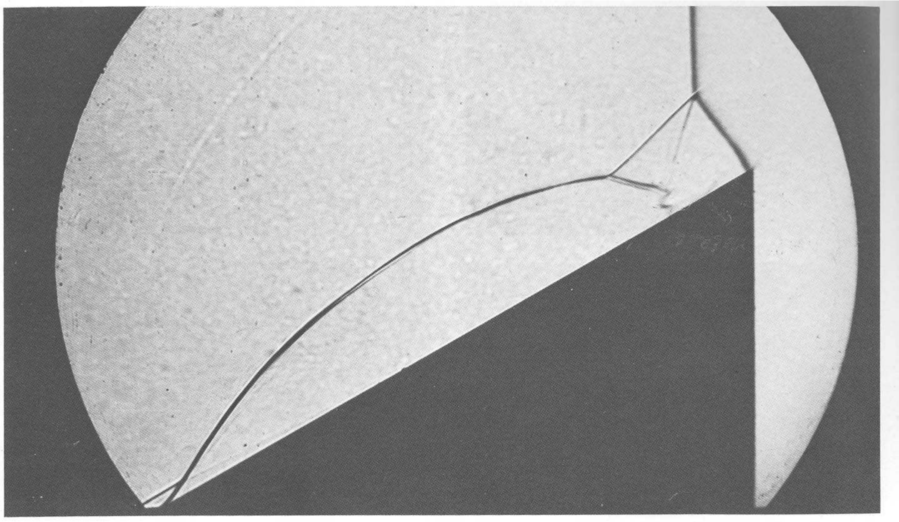

Figure 3-3: *A strong shock striking a reflecting wedge gives rise to a complicated pattern of shocks and contact discontinuities. Photograph taken from Van Dyke (1964).*

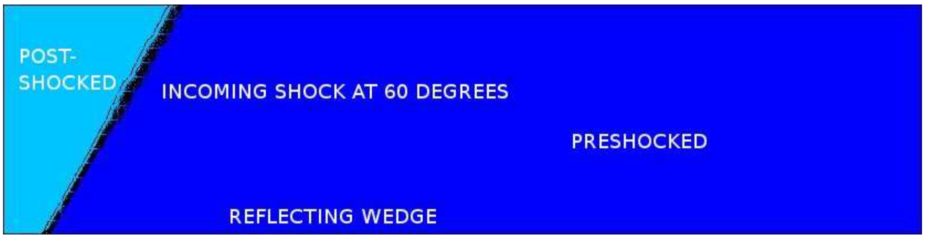

Figure 3-4: *Double Mach Reflection Initial Conditions.*

probelm is rotated so that the surface of the wedge is a on the lower x boundary (see Figure 3-4). It is implemented on a $4x1$ domain. The wedge is represented by a reflecting boundary condition from $x = \frac{1}{6}$ to $x = 4$. The upper boundary is a perfectly resolved Mach 10 moving shock (this introduces a small numerical error which is a feature of the problem). The initial conditions for the problem are as implemented in Toth & Odstrčil (1996); Woodward & Colella (1984) and are as follows.

Preshocked medium:

$$U = (\rho = 1.4, v_x = 0, v_y = 0, p = 1) \tag{3.3}$$

Postshocked medium:

$$\rho = 8, v_x = 8.25 \sin\left(\frac{\pi}{3}\right), v_y = -8.25 \cos\left(\frac{\pi}{3}\right), p = 116.5 \tag{3.4}$$

The adiabatic index, $\gamma = 1.4$. Seven levels of refinement are used to resolve as much of the instabilities as possible.

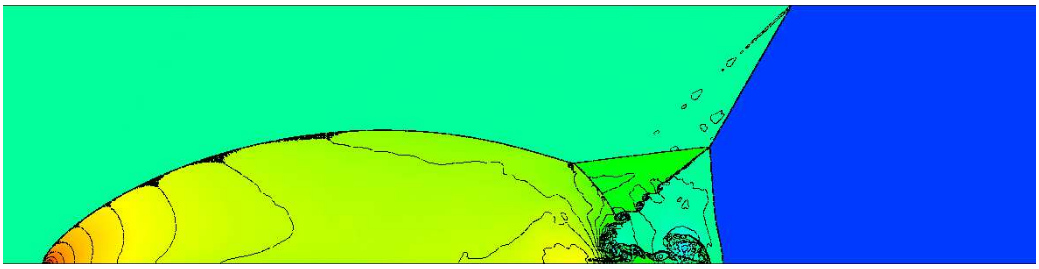

Figure 3-5: *Isopycnics for double Mach reflection, parameters are α=60° , γ=1.4, M=10. This compares well with published results using this test (Woodward & Colella 1984; Stone & Norman 1992; Berger & Colella 1989). Main features visible include the contact discontinuity roll-up along the lower right of the image, launching a jet of dense material towards the Mach stem and causing it to bulge outwards, the triple point or lambda point where the three shocks meet and the wall heating error where the perfect resolution at the a priori boundary condition contrasts with the slight smearing by the numerical code.*

3.2.3.2 Results

The results of the test problem (Figure 3-5) are similar to those in Toth & Odstrčil (1996); Downes (1996), Woodward & Colella (1984). This is consistent with the fact that all these methods are based n the PPM scheme. Stone & Norman (1992), using the ZEUS-2D code, which is not based on PPM, are also in agreement. The small numerical error visible behind the incident shock is caused by the perfect resolution of the shock at the boundary. The advection scheme spreads out this shock slightly and causes an overheated region to appear. In comparison with the experimental results, the experimental results do not show as much detail but the bulge in the outer wall is visible (see Figure 3-6) and part of the contact discontinuity rollup is also visible.

3.3 Cooling Tests

3.3.1 Overstable Radiative Shock

Under certain conditions, fast radiatively cooling flows have been shown to be unstable (Chevalier & Imamura 1982), where the size of the shock oscillates significantly. This instability turns on above a minimum pre-shock velocity and the onset and characteristics of this instability are powerful verifications of the correctness and general nature of any hydrodynamical code (Imamura et al. (1984), Gaetz et al. (1988), and Innes et al. (1987)).

The main characteristic, overstable oscillation occurs when a shock moving away from a wall

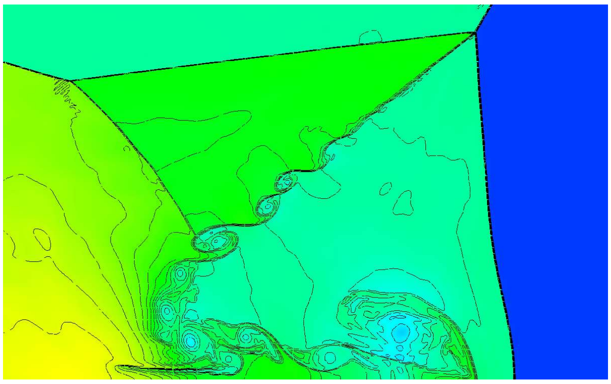

Figure 3-6: *Isopycnics for double Mach reflection. Detail of Figure 3-5 - notice the Kelvin-Helmholtz instability on the contact discontinuity. The triple points are evident at the upper left and right corners of the image. The jet of dense material which causes the Mach stem to bulge outwards is also visible.*

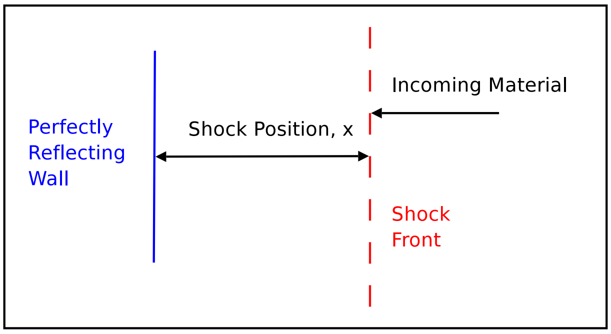

Figure 3-7: *Strong radiative shock reflected from a wall, oscillating back and forth.*

increases its cooling length so has a larger cooling region. The shock loses thermal pressure support and falls back towards the wall, which then repressurises it and drives it back out again.

The results shown for velocities of 140,160 and 170 km/s demonstrate that the stability limit lies in the range below 140 km/s.

3.4 MHD Tests

3.4.1 MHD Shock Tube

Shock tube tests from Ryu & Jones (1995) are used. All shock tube tests were carried out using a grid of 500 cells, a Courant number of 0.5 and an adiabatic index of $\gamma = 5/3$. Note that the adaptive mesh refinement is turned off so that the results can be compared with non-AMR codes.

The initial conditions for the MHD shock tube test are as follows:

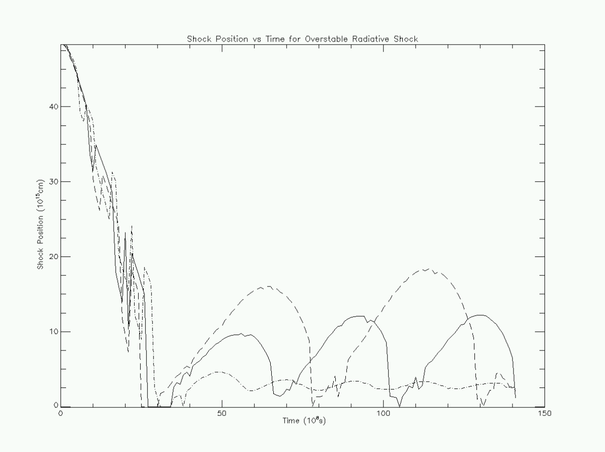

Figure 3-8: *Shock position vs. time plotted for overstable radiative shock test, for velocities, 140, 160, 170 km/s. The results shown for velocities of 140, 160 and 170 km/s demonstrate that the stability limit lies in the range below 140 km/s.*

Left State:

$$U_L = (\rho = 1, v_x = 0, v_y = 10, p = 20, B_x = 5, B_y = 5) \tag{3.5}$$

Right State:

$$U_R = (\rho = 1, v_x = 1, v_y = -10, p = 1, B_x = 5, B_y = 5) \tag{3.6}$$

The results of the simulation show the main features, fast shock, slow rarefaction, contact discontinuity, slow shock and fast shock have all been captured, however the contact discontinuity has been smeared over a few cells (see Figure 3-9).

The initial conditions for the second MHD shock tube test are as follows:

Left State:

$$U_L = (\rho = 1, v_x = 0, v_y = 0, p = 1, B_x = 3, B_y = 5) \tag{3.7}$$

Right State:

$$U_R = (\rho = 0.1, v_x = 0, v_y = 0, p = 10, B_x = 3, B_y = 2) \tag{3.8}$$

The results of the simulation show the main features, fast shock, slow shock, contact discontinuity, slow rarefaction and fast rarefaction have all been captured, there is a small oscillation near the fast rarefaction (see Figure 3-10).

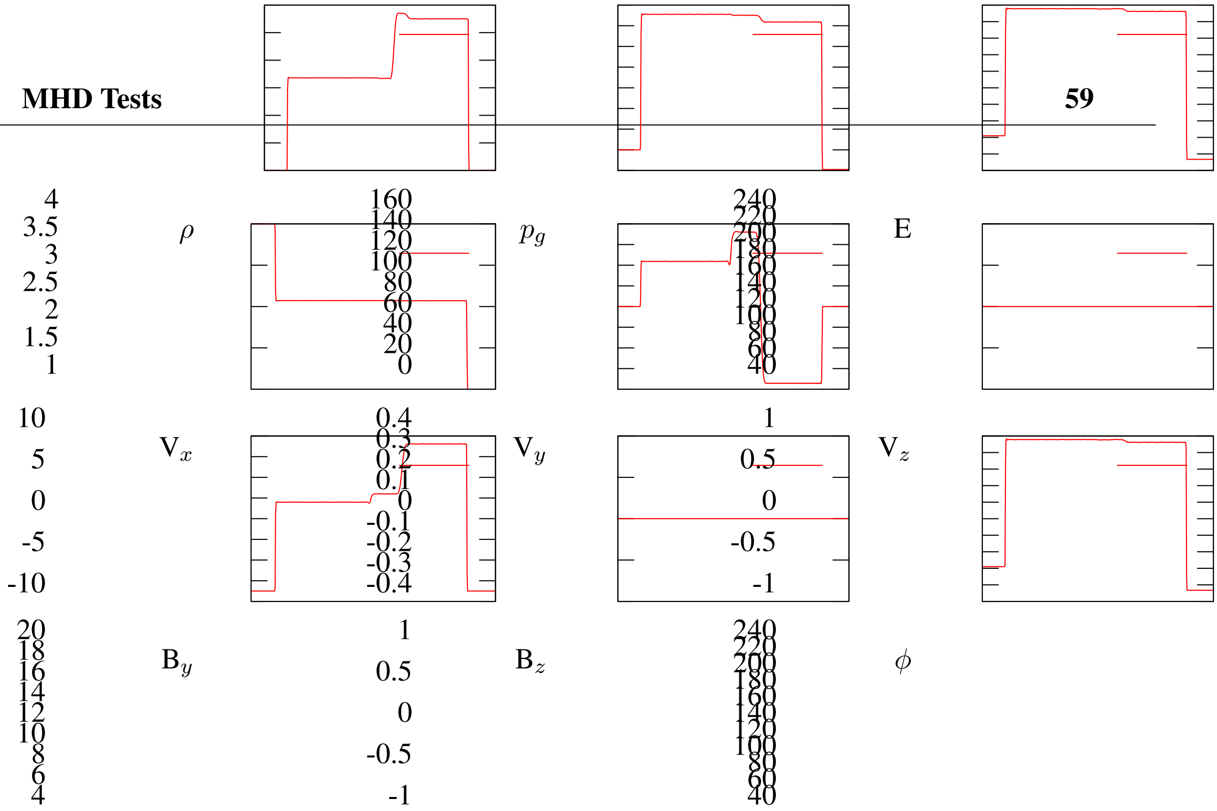

Figure 3-9: *Results of the first one-dimensional MHD shock tube Ryu & Jones (1995) test at time t=0.8 for comparison with Ryu & Jones (1995). The results of the simulation show the main features, fast shock, slow rarefaction, contact discontinuity, slow shock and fast shock have all been captured, however the contact discontinuity has been smeared over a few cells.*

3.4.2 Orszag-Tang Vortex

It is more difficult to find experimental results for regimes where the ideal MHD approximations apply. In this test a pure mathematical abstraction is used, to test the ability of the code to respond to oblique 2D MHD shocks during the decay to into MHD turbulence. The vortex of Orszag and Tang (Orszag & Tang 1979) is an excellent test of MHD shocks. It consists of a superposition of sinusoids of magnetic and velocity fields of different frequencies. It is a common test for 2D MHD (it is referred to as “frequently touted” in Hayes et al. (2006)) and has been used by among others Londrillo & Del Zanna (2000), O’Sullivan (1999), Dai & Woodward (1998), Ryu et al. (1998), Ryu

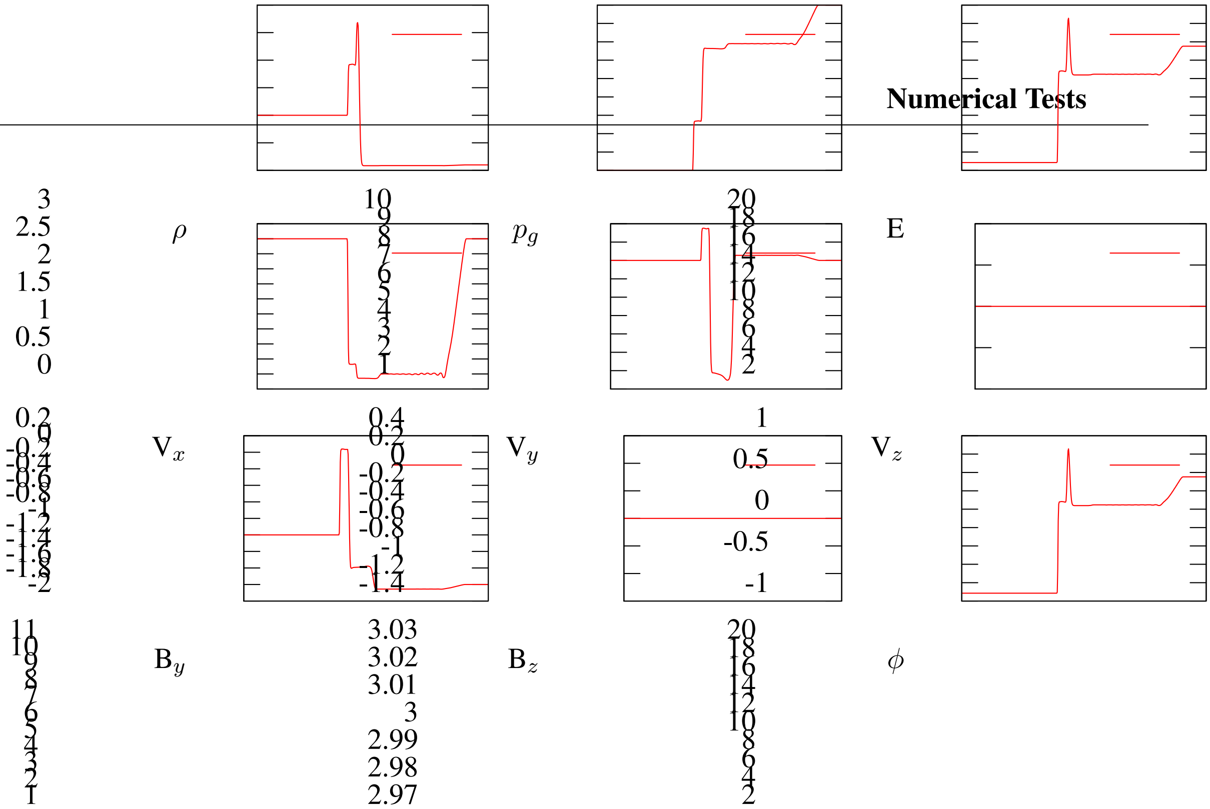

Figure 3-10: *Results of the second one-dimensional MHD shock tube Ryu & Jones (1995) test at time t=0.8 for comparison with Ryu & Jones (1995). The results of the simulation show the main features, fast shock, slow slock, contact discontinuity, slow rarefaction and fast rarefaction have all been captured, however the contact discontinuity and slow shockhave been smeared over a few cells. There are also some small oscillations near the fast rarefaction (at the extreme right).*

et al. (1995). The initial conditions are taken from O'Sullivan (1999)

$$U = \left(\begin{array}{c} \rho = \frac{25}{36\pi} \\ v_x = -\sin(2\pi y) \\ v_y = \sin(2\pi x) \\ v_z = 0 \\ B_x = -\sin(2\pi y) \\ B_y = \sin(4\pi x) \\ B_z = 0 \\ p = \frac{5}{12\pi} \end{array} \right) \tag{3.9}$$

Values for p, ρ, and γ are deliberately chosen, so that the speed of sound, $c = \sqrt{\gamma p/\rho} = 1$. Orszag-Tang tests how a code handles MHD shocks in the transition to 2D MHD turbulence.

The contours shown in Figure 3-11 demonstrate excellent agreement with preceding studies, e.g. RJF, LDZ both show excellent agreement which represents a good validation of the code.

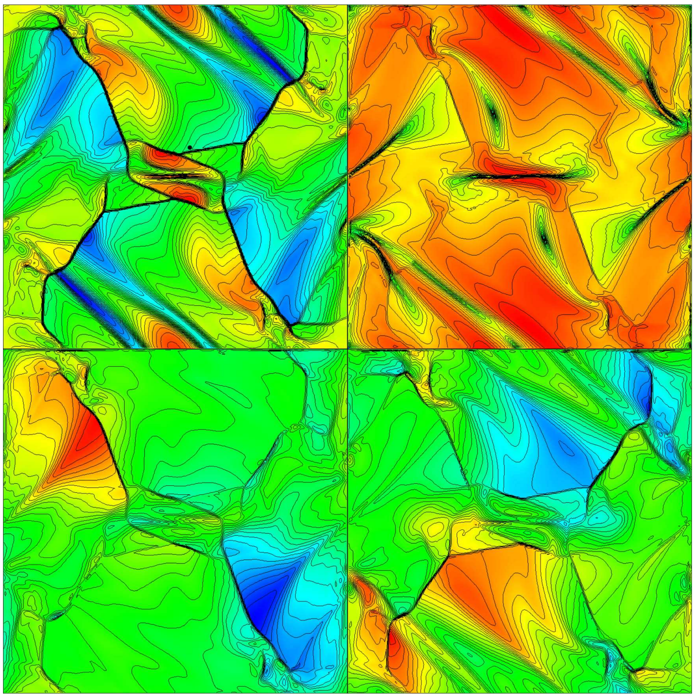

Figure 3-11: *Contours of magnetic pressure (upper left), thermal pressure (upper right), compressibility* $\nabla \cdot \mathbf{v}$ *(lower left) and vorticity* $\nabla \times \mathbf{v}$ *(lower right). Periodic boundary conditions were used on a domain of x=[0,1], y=[0,1] using 256x256 cells with a Courant number of 0.5. The initial configuration was set to match that of RJF and is* $\rho = \frac{25}{36\pi}, v_x = -\sin(2\pi y), v_y = \sin(2\pi x), v_z = 0, B_x = -\sin(2\pi y), B_y = \sin(4\pi x), B_z = 0, p = \frac{5}{12\pi}$ *The results show excellent agreement with Londrillo & Del Zanna (2000), O'Sullivan (1999), Dai & Woodward (1998), Ryu et al. (1998), Ryu et al. (1995).*

3.4.3 MHD Blast Wave

In the MHD blast wave test, a circular area of high pressure is embedded within a strong magnetic field. An explosive expansion results. This problem has been studied as a possible model for dynamical solar phenomenae, particularly Moreton waves and EIT waves (Chen et al. 2002). See Cliver et al. (1999) for a review of the topic. Gardiner & Stone (2005) studied this problem and the initial conditions from that paper are used in this test. In this case the magnetic field is set at an angle of 45°. Initial conditions for the entire grid are set to:

$$U = \begin{pmatrix} \rho = 1 \\ v_x = 0 \\ v_y = 0 \\ v_z = 0 \\ B_x = 10/\sqrt{(2)} \\ B_y = 10/\sqrt{(2)} \\ B_z = 0 \\ p = 1 \end{pmatrix} \tag{3.10}$$

The blast is represented by a pressure 100 times the ambient pressure. Its initial radius is 0.125. The simulation was performed on a grid of unit side with periodic boundary conditions. The density colourmap, the log magnetic pressure and the log pressure at time t=0.2 are shown in Figure 3-12. The field lines are overplotted onto the density colormap. The maximum density is 3.32, within 1% of the result of Gardiner & Stone (2005). Under the influence of the external magnetic field, the initial pressure wave loses its spherical symmetry as it propagates through the ambient medium. Two dense shells propagate parallel to the magnetic field (the red crescents in the density colourmap Figure 3-12). Perpendicular to the magnetic field, it can be seen from Figure 3-12 that the magnetic pressure dominates over the blast wave, and the field lines are only mildly bent.

3.5 Simulation

All simulations were carried out on a 32-node, 32-bit Beowulf-type cluster, Leda and on a 210-node 64-bit cluster, Rowan. The Fortran 90 code was compiled using the Intel optimisations for speed.

3.6 Code comparison and scheme comparison

In collaboration with the Torino astrophysics group a comparison of the astrophysics code ATLAS with PLUTO (Mignone et al. 2004) was undertaken.

3.6.1 PLUTO description

PLUTO is a versatile code which can integrate the MHD equations using the CTU method and the Roe solver. It has been used for a several jet simulations and supports Cartesian and curvilinear coordinates in 1, 2 and 3 dimensions. The code includes implementations of several numerical algorithms in the form of modules.

3.6.2 Performance

In all tests PLUTO was noticeably faster - this is partially because the AMR in ATLAS was turned off for the purposes of the simulation and still represents some overhead.

3.6.3 Comparison I: Underdense Adiabatic Jet

The first comparison problem is an adiabatic Mach 30 jet underdense ($\eta = 0.1$) jet propagating into an undisturbed ambient medium. The comparison between the results shown by the two codes is shown in Figure 3-13. As expected the jets have good agreement in speed and maximum density which agrees with the analytical result.

There are however several points of difference. The internal structure of the cocoon, the width of the bow shock and the structure of the crossing shocks along the length of the jet all show differences.

In the PLUTO simulation, two jets appear on either side of the main flow. They are much more clearly resolved than in the ATLAS solution.

3.6.4 Comparison II: Overdense Adiabatic Jet

The second comparison problem is an adiabatic Mach 10 jet overdense ($\eta = 10$) jet propagating into an undisturbed ambient medium. The comparison between the results shown by the two codes is shown in Figure 3-14.

There are several points of similarity, the minimum densities are the same and overall appearance of the bow shock and the jet beam are very similar.

As for the points of difference, there is difference in the propagation distance (this may be partially attributed to a slight difference in time between the two simulations) and the cocoon has a lower density feature in the ATLAS simulation. In the overdense jet case there is a difference in the velocities of the two jets. The maximum density is slightly higher in the PLUTO simulation.

The differences between the two results may result from the approximation to the spatial derivative of the conserved flux (see Section 2.2.6), which is fourth order in PLUTO and second order in ATLAS. This results in higher order accuracy in the PLUTO result.

3.7 Summary

The code has been tested thoroughly in one and two dimensions and shown to be accurate and robust. For the one-dimensional tests there is good agreement with the analytical results. For the two-dimensional tests, qualitatively there is good agreement with experimental results, providing some level of validation to the code for these problems. Quantitatively the results agree with the published results of numerical codes. From the code comparison with the astrophysics code PLUTO it may be seen that there is good agreement.

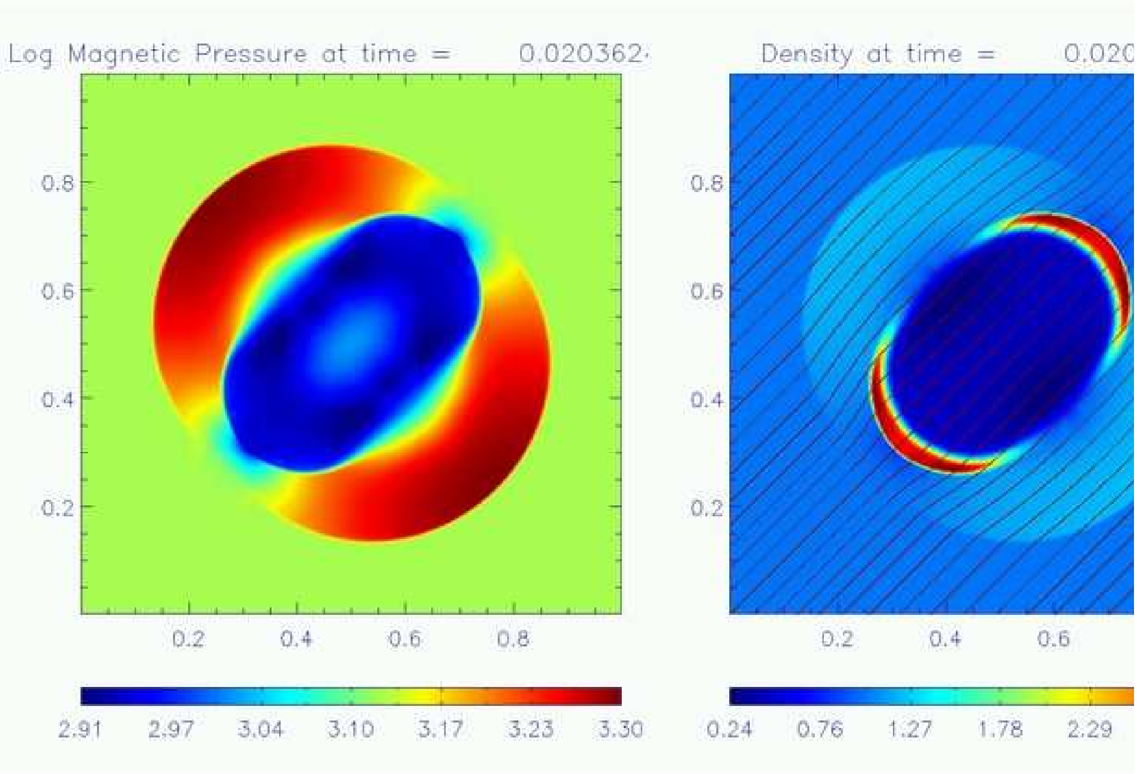

Figure 3-12: *Solution for the MHD blast wave log magnetic pressure, density and log thermal pressure at time t=0.2. The field lines are overplotted onto the density colourmap. The initial conditions are:* $\rho = 0.1, B_x = 10/\sqrt{(2)}, B_y = 10/\sqrt{(2)}, p = 0.1$. *The grid is of unit side with periodic boundary conditions.*

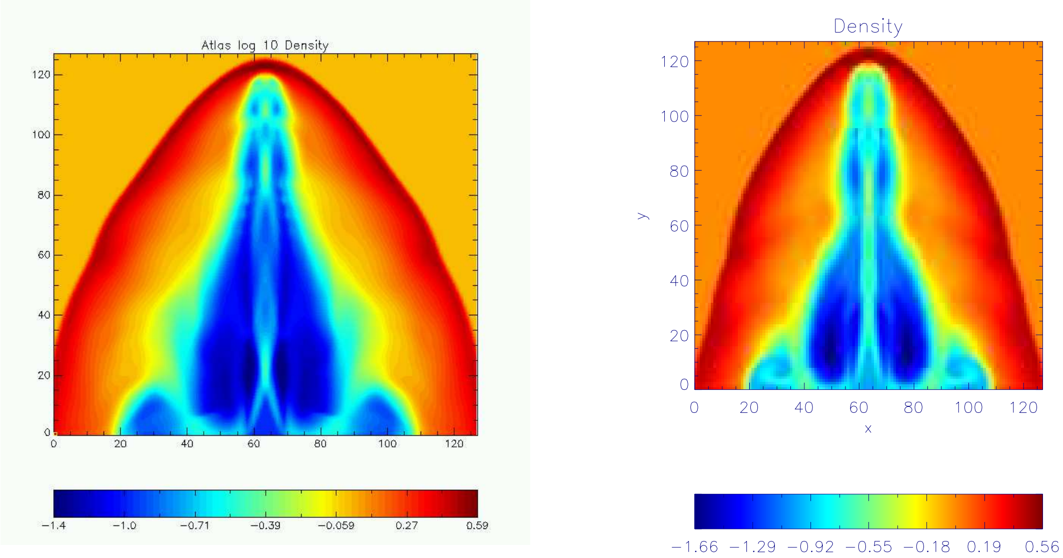

Figure 3-13: *Comparison of numerical codes ATLAS and PLUTO for an underdense ($\eta = 0.1$) jet, using directionally unsplit schemes and Roe solver.*

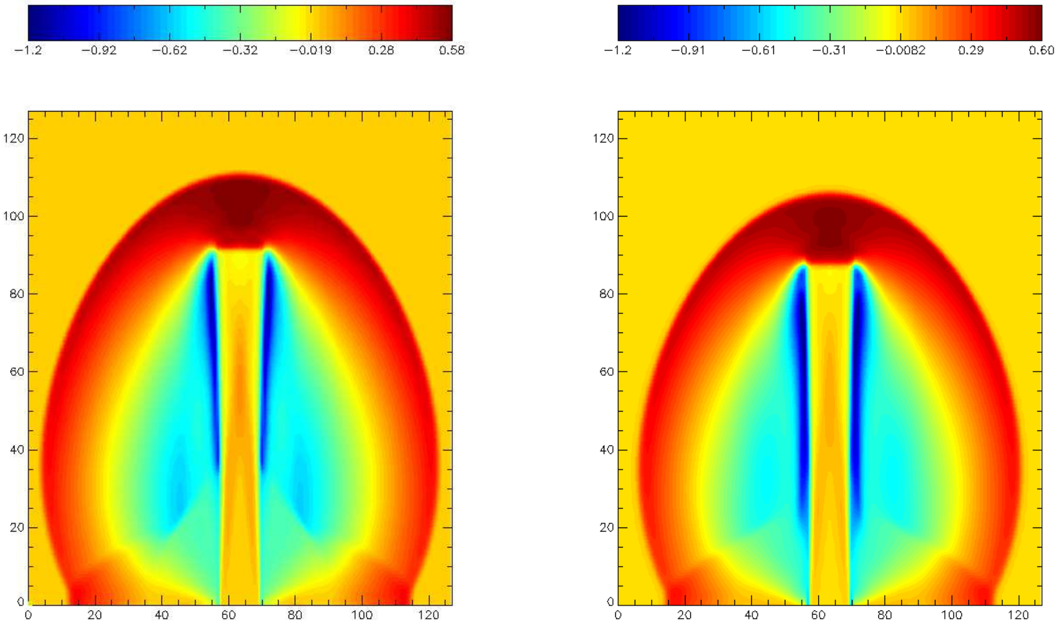

Figure 3-14: *Density colourmaps of a comparison of numerical codes ATLAS (left panel) and PLUTO (right panel) for a Mach 10 jet, using directionally unsplit schemes and Roe solver.*

4

Jets from Binary Protostars

In this chapter, we investigate potential models that could explain why multiple systems predominantly show single jets. During their formation, stars are supposed to produce energetic outflows and jets. However, binary jets have only been observed in a very small number of systems. We model numerically 3D binary jets for various outflow parameters. We also model the propagation of jets from a specific source, namely LDN1551 IRS 5, using recent observations as constraints for simulations with a new MHD code. We examine their morphology and dynamics, and produce synthetic emission maps. We find that the two jets interfere up to the stage where one of them is almost destroyed or engulfed into the second one. We are able to reproduce some of the observational features of LDN1551 such as the bending of the secondary jet. While the effects of orbital motion are negligible over the jets dynamical timeline, their interaction has significant impact on their morphology. If the jets are not strictly parallel, as in most observed cases, we show that the magnetic field can help the collimation and refocusing of both of the two jets.

4.1 Introduction

4.1.1 Jets and star formation

The majority of stars are binaries or part of multiple systems. During their formation, most stars are thought to produce energetic outflows and jets. However, binary jets have only been observed in a very small number of systems.

4.1.2 Binary Systems

The formation of binary systems is still poorly understood. It is well established that multiple sources can be the source of HH objects, e.g. T Tau, IRAS 04325-1419, Z Cma, Sz 68, SR 24, S Cr A, AS 353 (Reipurth et al. 1993). A multiple system may produce a single jet or outflow or a set of multiple outflows. Depending on the binary separation distance, the disk configuration may either be in circumstellar disks or circumbinary disks (Hartigan et al. 2000a). Few binary jets from binary protostars have been observed despite estimates which show large majorities of binary and multiple star systems among stellar populations (Patience et al. 2002; Simon et al. 1995; Ghez et al. 1993; Zinnecker et al. 1992; Duquennoy & Mayor 1991). In particular, for low mass pre-main sequence stars the binary fraction was estimated to be 60($\pm$17%) (Ghez et al. 1993). This implies that there should be “many” visible binary jets. The examples known to the author are compiled in Table 4.1. The frequency of existing binary jets is low compared to the large number of protostellar binary sources.

4.1.3 Models for Binary jets

In the models of Ferreira (1997); Shu et al. (1987a) and Shu et al. (1987b) a single circumstellar disk produces a bipolar outflow or jet. However, observations have shown that multiple or quadrupolar jets may occur. Reipurth et al. (1993) discovered a second flow HH144 from the same source as HH1-2. Gredel & Reipurth (1994b) observed a second flow (HH121) from the same source as the well-known HH111 outflow. In both cases there are large angles of separation between the two jets. However observations of apparent double jets can also be explained by other means: Avery et al. (1990) imaged the outflow in L723 and found a distinct multi-polar morphology. They concluded that the lobes of the jets were in fact shell walls of two cavities swept clear by a single bipolar outflow. Anglada et al. (1991) discovered a double radio source at the centre of the outflow structure and this led to a reappraisal of the of the double outflow theory (Anglada et al. 1996;

Table 4.1: *Evidence of Binary Jets and Outflows?*

Outflow (Source)	Cloud	RA (J2000)	Dec (J2000)	Reference
HH154 (LDN1551 IRS 5)	Tau-Aur	04 31 34.20	+18 08 04.8	Liseau et al. (2005)
HH1-2 - HH144	Orion	05 36 22.85	-06 46 06.6	Reipurth et al. (1993)
HH111 - HH121	Orion	05 51 46.07	+02 48 30.6	Gredel & Reipurth (1994a)
BHR71	N.A.	12 01 37	-65 08 53.5	Parise et al. (2006)
L723 (IRAS 19156+1906)	Cep	19 17 53.16	+19 12 16.6	Anglada (2004)
HH288 (IRAS 00342+6347)	Cep	00 37 11.07	+64 03 59.8	Gueth et al. (2001)
HH377 (IRAS 23011+6126)	Cep E	23 03 13.9	+61 42 21	Ladd & Hodapp (1997)
IRAS 16293-2422	ρ Oph E	16 32 22.8	-24 28 33	Hirano et al. (2001)
IRAS 20050+2720	Cyg Rift	20 07 06.7	+27 28 53	Bachiller et al. (1995)

Girart et al. 1997; Anglada et al. 1998; Hirano et al. 1998; Palacios & Eiroa 1999; Shirley et al. 2002; Estalella et al. 2003; Anglada 2004). Other example of multiple molecular outflows include IRAS 16293-2422, IRAS 20050+2720.

There are several possible explanations for the apparent paucity of binary jets and outflows. One possible explanation is simply that the number of binary systems has been overestimated (Lada 2006). However this still leaves a large number of known binaries without binary jets or outflows. Another possibility is that the dust extinction from the circumbinary material may block the smaller outflow from view in some cases. A third possibility is that the two jets - which launched from roughly the same regions - merge into a single jet. A detailed model of binary jets presented here will show the effect of their relative sizes and speeds on their interaction. If the disks are not coplanar (Mathieu 1994) it reasonable to assume that binary outflows can have quite large angular separations. The current study is confined to pairs of jets with small angular separations e.g. the binary jet from LDN1551 IRS 5.

Numerical simulations of the binary jet model are performed using a specific object, LDN1551 IRS 5 (HH154) as a starting-point for the model.

A full examination of the interaction of binary jets is impossible to model using axisymmetry. Therefore a fully three-dimensional binary jet system is modelled using ATLAS, the code introduced in Chapter 2.

This chapter is structured as follows: in part 4.2 the observations of the source are summarised,

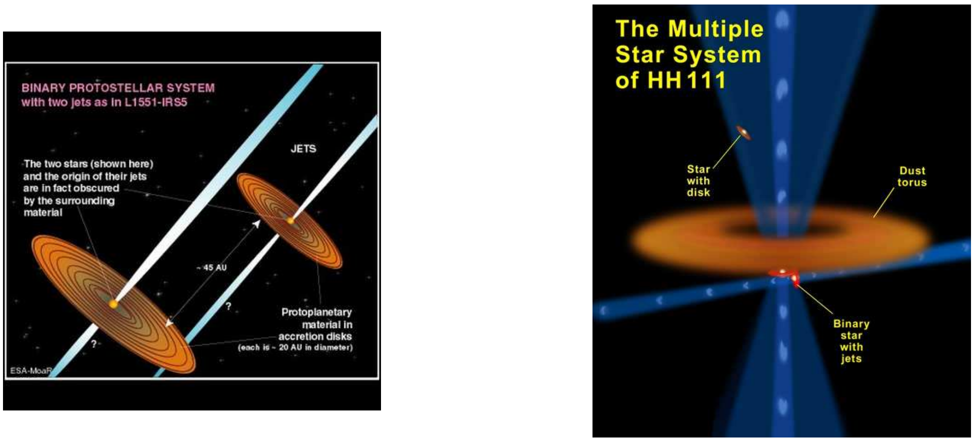
BINARY PROTOSTELLAR SYSTEM
with two jets as in L1551-IRS5
JETS
The two stars (shown here) and the origin of their jets are in fact obscured by the surrounding material
~ 45 AU
?
?
Protoplanetary material in accretion disks
(each is ~ 20 AU in diameter)
ESA-MoaR
The Multiple Star System of HH 111
Star with disk
Dust torus
Binary star with jets

Figure 4-1: *Left panel: Cartoon of LDN1551 IRS 5 jets. Right panel: Cartoon of H111 and HH121 jets.*

in part 4.3 the method is described, in part 4.4 the results of the simulation are presented, and finally in part 4.5 the consequences of the model are discussed.

4.2 Observations of jets from the binary protostar IRS 5

Using both the Hubble Space Telescope and SUBARU, two optical jets have been observed emanating from LDN1551 IRS5, located 140 parsecs away in the Taurus molecular cloud complex. The optical jets extend southwest and disappear at approximately 1400AU from the IRS5, where the large knot of [Fe II] emission is at y=12 arcsec in the upper panel of Figure 4-2. As for the origin of the two jets, the north and south jets appear to be launched from the south and north disks respectively of the binary system in LDN1551 IRS 5. The disks are not seen edge-on, the inclination angle has been estimated at about 45°.

Strom et al. (1976) observed the near-infrared source IRS 5 within the Lynds molecular cloud 1551 (LDN(=Lynd's Dark Nebula) 1551). Cudworth & Herbig (1979) discerned two fast Herbig-Haro objects, HH28 and HH29, near the IRS 5 source. Snell et al. (1980) saw for the first time in CO the "remarkable double-lobed structure" in LDN1551, molecular bipolar outflows extending for 0.5 parsecs in opposite directions, with velocities of 15 km s^{-1}. This was among the first molecular bipolar outflows discovered. Bieging & Cohen (1985) identified IRS 5 as a binary source. Moriarty-Schieven & Wannier (1991) and Pound & Bally (1991) identified a second outflow from the same source. Mundt et al. (1991) also observed two independent rows of knots although these were interpreted as edges of a limb-brightened cavity, and were only identified as jets by Fridlund &

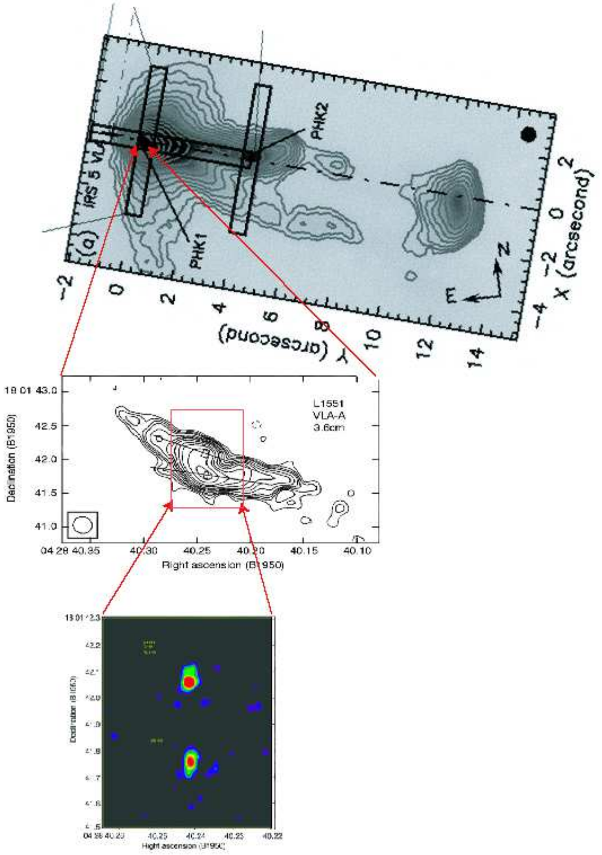

Figure 4-2: *Observations of LDN 1551 IRS 5. The upper panel shows an image of the jet pair in [FeII] from Pyo et al. (2002). The middle panel is a radio image at* 3.6 *cm of the binary jet which shows the blue and red lobes of the binary jets from Rodríguez et al. (1998). The two rectangles at the centre of the image mark the positions of the two disks. The solid lines show the estimated directions of the two disks. The lower panel is a radio image of the pair disks which drive the binary jets at*7 *mm from Rodríguez et al. (1998).*

Liseau (1998) (hereafter FL). FL opined that only one jet is currently active. They also estimated that the jets were almost completely ionised. FL determined that the angular separation between the jets is approximately 20°. Rodríguez et al. (2003) confirm the jet binarity at radio wavelengths. Rodríguez et al. (1998) confirmed that LDN1551 IRS 5 was a binary system and show the first images of the circumbinary disks and the red lobes of the two jets. Additionally they suggested that there is a circumbinary structure and a large-scale envelope around LDN1551 IRS 5. Lay et al. (1994) observed a large circumbinary disk of $\sim$ 160 AU in diameter. Liseau et al. (2005) provide a value for binary separation of 40 AU. An excellent review of the observations until 1997 can be found in Fridlund et al. (1997).

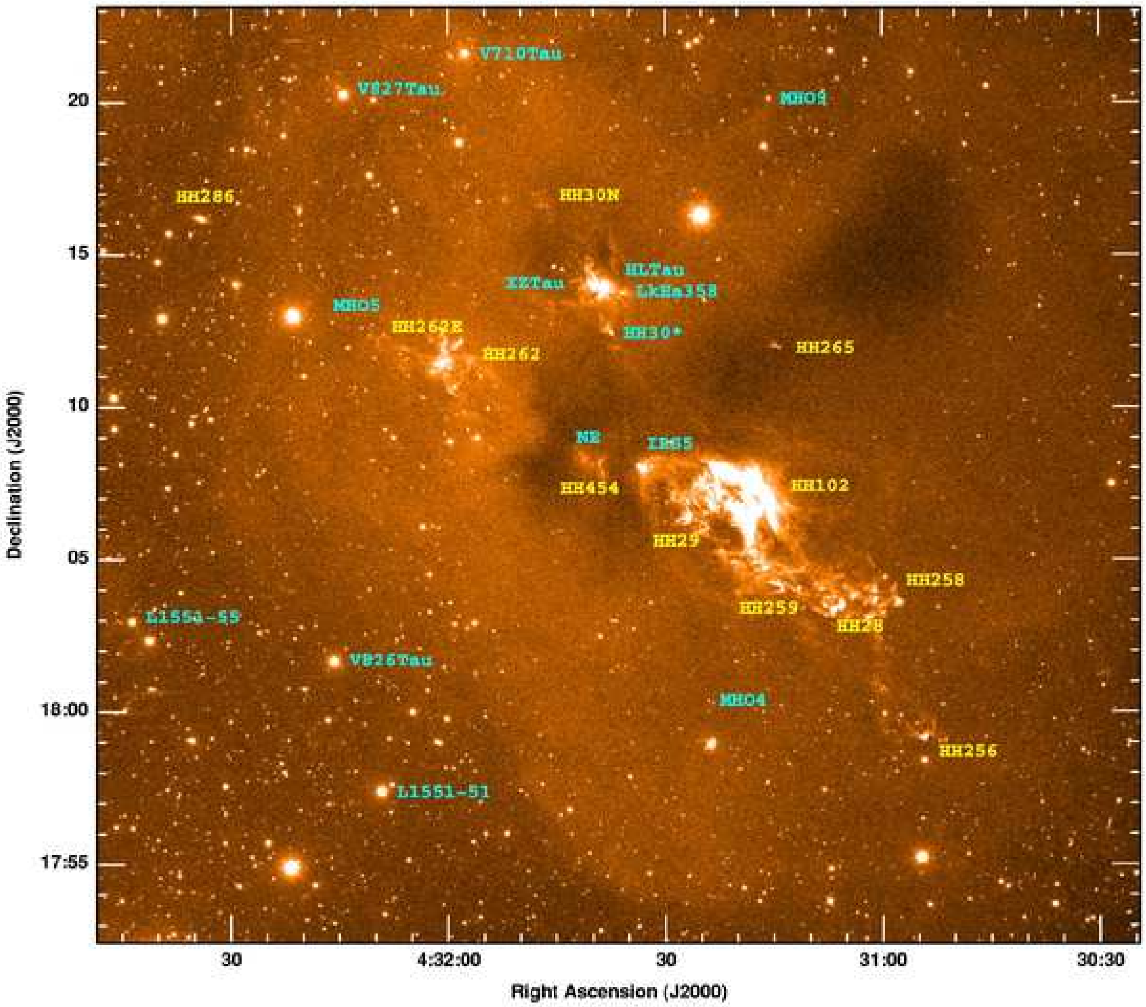
V710Tau
V827Tau
MHO8
HH286
HH30N
XZTau
HLTau
LkHa358
MHO5
HH262E
HH262
HH30*
HH265
NE
IRS5
HH454
HH102
HH29
HH258
HH259
HH28
L1551-55
V826Tau
MHO4
HH256
L1551-51
20
15
10
05
18:00
17:55
Declination (J2000)
30
4:32:00
30
31:00
30:30
Right Ascension (J2000)

Figure 4-3: *Observations of LDN 1551 molecular cloud in [SII] on the Cerro Tololo Telescope, from Moriarty-Schieven et al. (2005). The infrared source of the binary jets, IRS 5 is located at RA 04 31 34.20 DEC +18 08 04.8.*

4.2.1 Morphology

Itoh et al. (2000) observed "a pair of twisted jets of ionised iron" from the LDN1551 IRS 5. They argued that the orbital period of the sources, if equated to the precession of the two jets, is too long to be responsible for the observed twisted morphologies of the jets. Possible other mechanisms can be magnetic in nature e.g. the Lorentz forces may be strong enough to deflect a jet with a potentially small momentum (Fendt & Zinnecker 1998, 2000).

4.2.2 X-ray emission

Soft X-ray emission with a peak at 1 keV from the region of the head of the north jet was observed by Favata et al. (2002). Bonito et al. (2004) carried out a numerical simulation of the north jet, using a velocity of 1.4×10^3 km s^{-1} for the initial jet velocity and reproduced the jet head X-ray emission. Bally et al. (2003) performed a higher angular resolution study, finding a source of X-rays in LDN1551 IRS 5 which they attributed to either fast shocks or reflected x-rays from IRS 5 scattered out through the outflow cavity. Bally et al. (2003) put forward several models to explain the X-ray emission, including the intriguing possibility of a quasi-stationary X-ray luminous shock maintained by interacting colliding winds between the two protostars.

4.2.3 Polarimetry

Scarrott (1988) observed optically a magnetic field perpendicular to the jet axis, and concluded that it could be explained by a toroidal field in the cloud around the outflow. Lucas & Roche (1997) also observed this “peculiar pattern of alignment”. The physical cause for the polarimetry pattern remains unexplained.

According to Liseau et al. (2005) the northern jet is faster with velocity strictly higher than 430 km s^{-1} whereas the southern jet has velocity at most 65 km s^{-1}. Recent observational evidence has suggested that the source may have a small third companion (Lim & Takakuwa 2005).

The picture being built up over 25 years of observations is that of a pair of YSOs each with its own associated disk and outflow, the whole structure embedded in a larger circumbinary structure, possibly a disk.

4.3 Method

The main goal is to model binary jets to examine the nature and extent of the interaction between the jets. Analytical models of single jets have been produced by e.g. Shu et al. (1994a), most of those models remain axisymmetric. However, axisymmetry assumes rotational symmetry in the jet axis and this is not true for binary jets; binary jet propagation and interaction require a full 3D model. A numerical study becomes necessary, and requires the use of a fully three-dimensional time-dependent model with magnetic field and radiative cooling. Constraints on current computational capacity require us to make certain approximations however so the ideal magnetohydrodynamic (MHD) approximations are used in order to include the effects of the magnetic field. The

Parameter	Value
N Jet Velocity	200-430 km s^{-1}
S Jet Velocity	65 km s^{-1}
Disk Separation	45 AU
Angle Between Jets	20°
Orbital Period	255 years
Ambient Density	5000 cm^{-3}
Jet Density	500 cm^{-3}
Jet Length	1400 AU
Jet Ion Frac	$\sim$1

Table 4.2: *Observed data for LDN1551 IRS 5*

non-ideal physics of optically thin atomic radiative cooling losses are included, and the ionisation fraction is tracked in the simulation. The ideal magnetohydrodynamics (MHD) equations are evolved in time. The equations are laid out in Section 2.1. Simulations were carried out using ATLAS (see Chapter 2 for a description) on a 64 node "Beowulf" cluster.

4.3.1 Initial and boundary conditions

A distance of 140 parsecs to the jets is assumed. Values for the density, temperature and velocities are based on the observations discussed above. A sinusoidally varying injection velocity (Raga et al. 1990) is assumed, with an amplitude of ±30% in the velocity and a period of 8 years for each jet. The ambient medium is modelled with a uniform density ($\rho_a = 5 \times 10^3$ cm^{-3}) and temperature ($10^2 K$) and the jets are modelled with density $\rho_{jet} = 0.1\rho_a$, temperature 10^4K and velocities of 65 and 300 km s^{-1} respectively (Liseau et al. 2005). A compromise figure of 300 km s^{-1} is chosen between the estimates of Liseau et al. (2005) and Hartigan et al. (2000b). The separation distance between the jets is 2×10^{15} cm. The launching of the two jets is also staggered, the faster northern jet is launched 150 years after the slower southern jet. (The launch times are predicted from the dynamical ages of the jets.) The velocity radial profile is a positive cosine - with its maximum, v_{jet} at r=0 in the jet centre, dropping to zero at r_{jet}. This profile is chose based on the observations of Bacciotti et al. (2000), where the highest velocities are thought to be located in the centre of the jet. The sheared profile is also consistent with the core/sheath morphology seen in Hardee & Rosen (2002) and Frank et al. (2000).

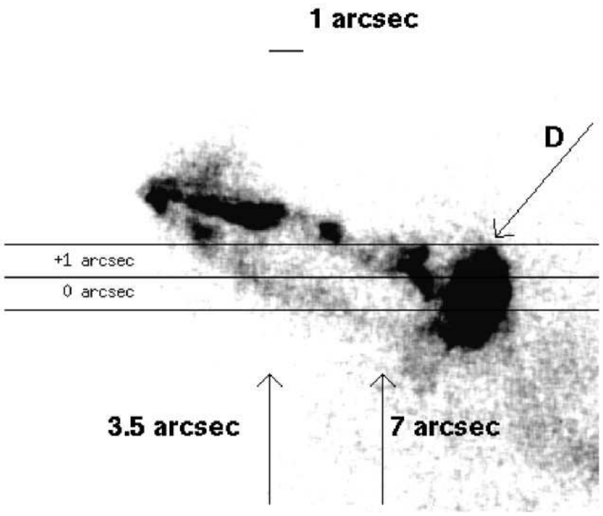

Figure 4-4: *Fridlund & Liseau (1998) provide a HST R-band image of the two jets from the binary protostar LDN1551 IRS 5, located in the constellation Taurus. (Image courtesy of Fridlund & Liseau (1998))*

The boundary conditions are inflow for $r < r_{jet}$, reflecting for $r > r_{jet}$ along the inner x-boundary (x=0) and outflow along all other boundaries.

4.4 Results

Results from fully 3D HD and MHD simulations of the jets from the binary protostar LDN1551 IRS 5 are presented, which approximate the physical conditions producing the morphology in the emission.

4.4.1 Case I: HD

For the hydrodynamic case it is assumed the jets are initially parallel, which is how the LDN1551 jets appear. The jet interaction and its effect on the propagation of both jets is modelled.

The density slice from the 3D HD simulation (see Figure 4-5) clearly shows that the slow, secondary jet appears to bend close to the inlet. Such a bend or kink is also observed in the slow, southern jet of LDN1551 IRS 5 about $4''$ (560 AU at a distance of 140 pc from the source (Itoh et al. 2000)). In the simulation shown in Figure 4-5 a kink in the slow southern jet is also visible - both in the density midplane cut shown in Figure 4-5 and in the derived emission maps shown in 4-8. This is caused by the bow shock of the fast jet interacting with the beam of the slow jet. The northern jet has a Mach number ~ 3 times higher than the slow southern jet and simply pushes it out of

Domain	$-240\text{AU}< y,z < 240$ AU
	$0< x <$1440 AU
Coarsest grid	$\Delta x = \Delta y = \Delta z = 268$ AU
Finest grid	$\Delta x = \Delta y = \Delta z = 4$ AU
Refinement	5 levels
N Jet velocity	$v_{jet} = 300$ km s^{-1}
S Jet velocity	$v_{jet} = 65$ km s^{-1}
Jet density	$\rho_{jet} = 500$ cm^{-3}
Ambient density	$\rho_a = 5000$ cm^{-3}
Jet Temperature	$T_{jet} = 10^4 K$
Jet Radii	$r_{jet} = 4 \times 10^{14}$ cm
Jet Separation	$s_{jet} = 2 \times 10^{15}$ cm
N Jet Mach Number	M=60
S Jet Mach Number	M=12
Ambient Temp	$T_a = 100K$

Table 4.3: *Initial conditions*

the way. This reproduces the observed kink at $4''$ - without the need for magnetic fields. There is no noticeable reaction by the fast jet - possibly indicating that the estimated velocity is too high. By using simple hydrodynamical models the bent morphology of the LDN1551 IRS 5 outflow is reproduced using jet interaction.

4.4.2 Case II: MHD

In the second case, the jet behaviour closer to the source is explained. The parallel approximation is removed and an angular separation estimated at 20° is used. To redirect the two jets would require either a density contrast e.g. the wall of a conveniently shaped cavity or a magnetic hoop stress (Bally et al. 2003).

The magnetic field configuration based on the observations of Scarrott (1988) is used. Scarrott (1988) observed optically a magnetic field perpendicular to the jet axis, and concluded that it could be explained by a toroidal field. The toroidal field may be produced by the circumbinary material twisting the frozen-in local magnetic field lines.

In the ambient medium a toroidal field with a maximum value of B=10 μG is initialised. The

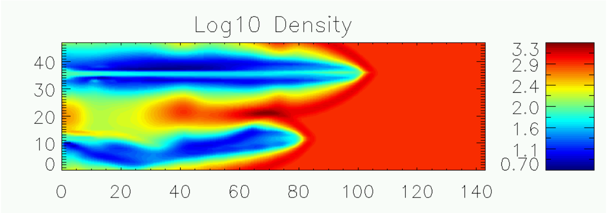

Figure 4-5: *The bent morphology of the southern (lower) jet is visible in this midplane colour density map of 3-D binary jet simulation at* $t = 245$ years*. The scale of the grid is* 1500AU *by* 400AU.

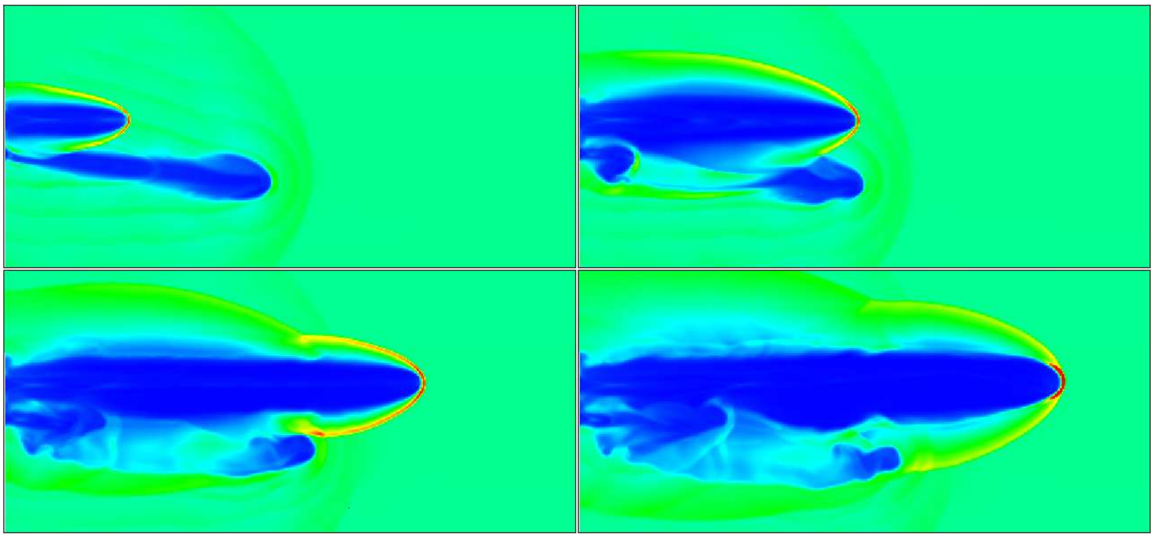

Figure 4-6: *Time evolution of MHD binary jets at t=125, 155, 170, 185 years. The images shown are 2D midplane cuts through the 3D grid. Blue is low-density, red is high density. Note that the angle between jet axes is quite discernable in the earliest panel, but not so much later, which shows the bending of the slow, southern jet over time.*

magnetic vector potential $\mathbf{A}$, where $\mathbf{B} = \boldsymbol{\nabla} \times \mathbf{A}$, had the analytical form $\mathrm{A}_x \propto \cos 2\pi y + \cos 2\pi z$. This is consistent with the observations (Scarrott 1988).

Figure 4-6 shows a series of density slices from the 3D MHD simulation. The binary outflow is modelled in full 3D with a toroidal magnetic field. Compared to the previous HD simulation, where the jets were parallel, the angle between the two jets is initially set to 20°. As a consequence, one might expect some divergence of the two jets. On the contrary, the slower jet is refocused along the faster jet and bends towards it. Eventually, the jet material from the slower jet gets merged into the faster one.

The observations of LDN1551 show both jets diverging from the source until about $4''$ from

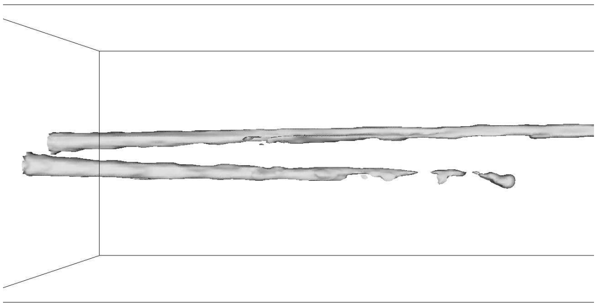

Figure 4-7: *Surface plot of 3-D binary jet simulation at* $t = 1648$ years. *The scale of the grid is* $4 \times 10^{17}\mathrm{cm} \times 10^{17}\mathrm{cm} \times 10^{17}\mathrm{cm}$ *A longitudinal magnetic field of* $10^{4}\mu$*G is used.*

the source when they change direction to pursue a roughly parallel course. The change in direction is most pronounced for the southern jet. In the simulation over the time evolution the southern jet slowly changes its direction to move parallel to the axis of the toroidal field. Hence, it appears that the hoop stress from the ambient toroidal field slowly changes the direction of the jets. Thus, magnetised binary jets will tend to collimate and refocus along the direction of the fastest or strongest jet.

4.4.3 Case III: Orbiting binary jet

The effects of orbital motion on the survival of the binary jets are now explored. Figure 4-7 shows a model of a binary jet from an orbiting source. The model made of two sources consists of one protostar disk orbited by a less massive companion - both driving jets. The jets have similar velocities and parameters. It is found that, from time-scale arguments in LDN1551 IRS 5, the orbital period of the binary (∼260 years) is too long to have much effect on the fast northern jet (dynamical age ∼90 years). The orbit of a binary source may in principle cause the jet to be unstable in the case of wide binaries with relatively short orbital periods. Hence, disks orbiting each other are less likely to drive coherent visible optical jets, while longer period close binaries may drive jets with a visible wiggle e.g. XZ Tau. Short-period orbits with a large binary separation may cause the binary jet configuration to be unstable. This is evidently not the case for LDN1551 IRS 5. However the binary period represents a powerful constraint on the formation of binary jets.

4.4.4 Emission maps

In order to predict the line emission produced by the binary jet model and compare against observations the density, temperature and the fraction of ionised hydrogen as computed in the numerical simulations is used. Solar abundances for the forbidden line elements in the fluid are assumed. Following Bacciotti (2002), the emissivity ϵ is:

$$\epsilon_{Z^i,\nu} = A_\nu \frac{hc}{\lambda} x_e n_H^2 \left(\frac{Z^i}{Z}\right) \left(\frac{Z}{H}\right) \left(\frac{n_{upper}}{n(Z^i)}\right) \tag{4.1}$$

where A_ν is the transition probability, n_H is the hydrogen nuclear number density, x_e is the ionised fraction of hydrogen. $\frac{Z^i}{Z}$ is the fraction of the element Z ionised at level i. This is set equal to 1 for S, assuming S is all singly ionised in low-excitation nebula. For O and N the fractional ionisation may be determined as a function of x_e and T_e assuming the O and N are in ionisation equilibrium with H, and using the equilibrium rate equations. $\frac{Z}{H}$ is the abundance of element Z and $\frac{n_{upper}}{n(Z^i)}$ is the fractional population of the upper level - this is determined by a 5-level linear system of equations in T_e and n_e. A more complete description of the method can be found in Bacciotti et al. (1995); Bacciotti & Eislöffel (1999) and Bacciotti (2002).

It is clear from the emission map shown in Figure 4-8 that the interaction has a strong observational signature. The second jet is virtually obliterated but remains visible at the point where the northern jet's bow shock impinges on the beam of the southern jet.

4.5 Discussion

4.5.1 The source of X-ray emission

Bally et al. (2003) find a source of X-rays in LDN1551 IRS 5 which they attribute to either strong shocks *near the base of the jet* or reflected x-rays scattered out through the outflow cavity. The strong shocks may be caused by jet collimation which could be magnetic in nature. Bonito et al. (2004) correctly predicted the proper motion of the X-ray source. In the binary jet model the X-ray source could possibly come from the colliding winds as suggested in Bally et al. (2003). The Bally

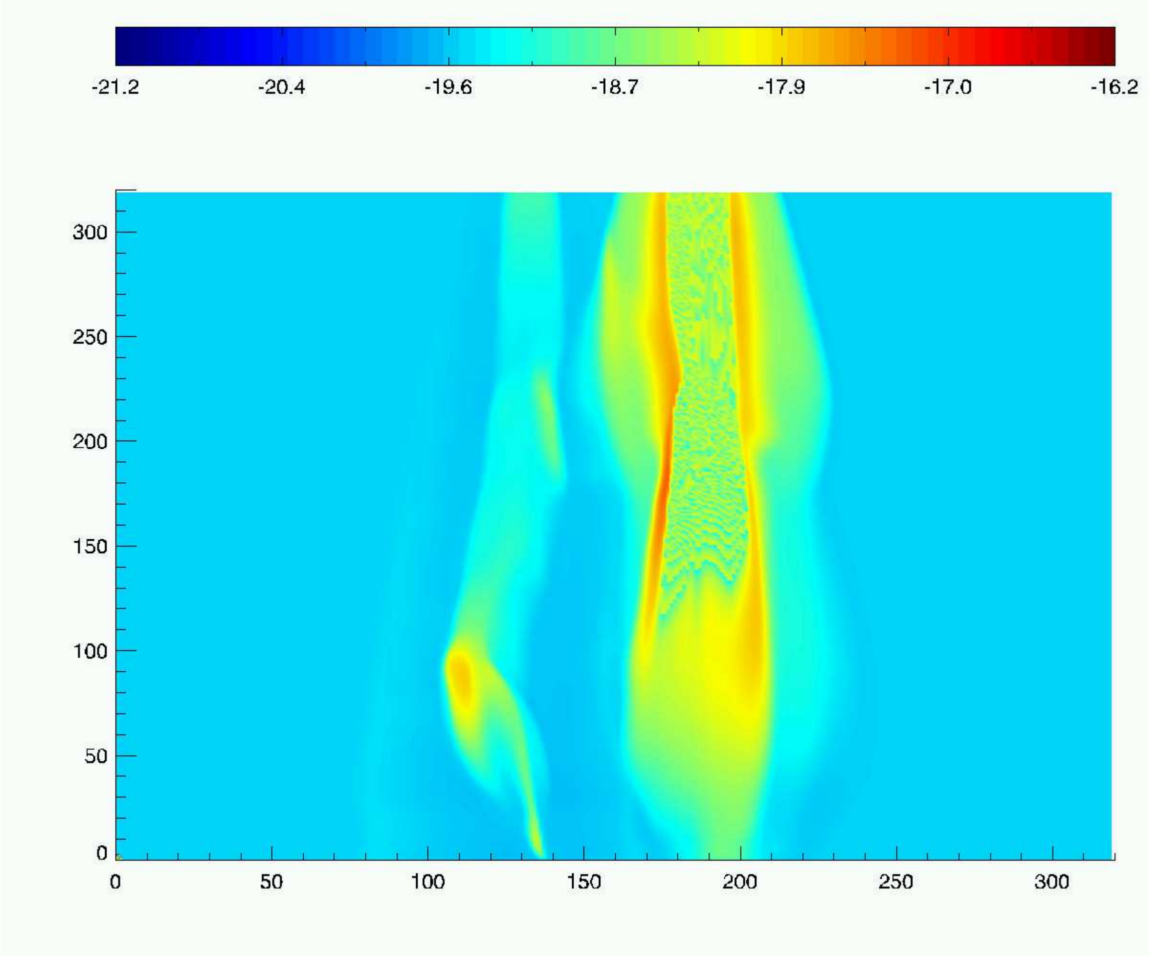

Figure 4-8: *[SII] line emission map to compare with observations of the LDN1551 IRS 5 jet (HH154). The image shows the lower part of the two jets at a time t=190.2 years. The emission map is quite different to what is seen in the density contour and shows that the second jet is almost obliterated by the faster jet. There is a peak in emission where the bow shock is striking the beam.*

model suggests that the X-rays come from a moving source at the base of the jets. If the density ratio is $n_{jet}/n_{ambient} = 0.1$ then the shock speed will be about 430/4=107 too slow to achieve X-ray emission temperatures. If on the other hand the density ratio is higher (e.g. 10) the jet is moving into a less dense region swept out by the slower jet the shock velocities will be higher 430*0.75 = 322. To get up to the observed shock velocity the density contrast would need to be much lower than observed e.g. 0.01 would give a velocity in the range required. The X-ray emission may then be more likely to originate in the binary source. Another possibility is that the X-ray emission is caused by magnetic reconnection in the interval between the two jets where the field is compressed by the pair of bow shocks.

4.5.2 Magnetic field effects

Magnetic field direction has a strong effect on the direction and magnitude of jets. Strom et al. (1986) and Tamura & Sato (1989) showed magnetic fields near young stars appears to be preferentially aligned with jet axes, where jets exist. On the other hand Ménard & Duchêne (2004) have suggested that magnetic fields are orientated randomly. In the case of LDN1551 IRS 5, the observations of the perpendicular magnetic field projected in the plane of the sky imply a toroidal field in the ambient medium surrounding the jet. The results from Section 4.4.2 show that such a toroidal field would affect the motion of the southern jet; and that both the magnetically driven change in direction together with the interaction of the bow shock of the fast jet with the beam of the slow jet contribute to the distinctive morphology.

4.5.3 Source orbiting effects

An orbiting source can cause jet precession. Indeed, Masciadri & Raga (2002) have used this effect to explain the wiggling of the jet associated with HH30. However in the particular case of LDN 1551 IRS 5, the period of oscillation is too long to have a very significant effect on either of the two jets over the length scale and timescale of interest here. However the LDN 1551 IRS 5 jets drive a massive ($\sim$0.5 parsec) molecular outflow, and the stirring motion produced by the 300 km s^{-1} two jets orbiting the source may contribute to the morphology of the 15 km s^{-1} molecular outflow. Decreasing the orbital period contributes to the jet breaking up – as the jet orbits it has to do extra work moving the ambient medium in a lateral direction. This has the effect of a transverse wind, shredding the jet. Obviously this is effect is small enough for the observed jets so they may be observed. However a short period binary should not be able to produce a stable jet especially if it is a wide binary. This is a major constraint on the production of binary jets.

4.5.4 Jet merging

In the case of LDN1551 IRS 5 the two jets appear to merge into a single bow shock at about 1400 AU from the source. However this effect is only apparent and although the jets appear to be bent either by the local variations in the density or the surrounding toroidal field they do not merge into a single jet.

The LDN1551 IRS 5 jet pair can be seen as both a pathological object unlike any other observed at such close range and as an ideal candidate for attempted explanation of the observed phenomena using a hydrodynamical code. The effects of source orbiting, density parameters, magnetic fields all play a role in sculpting this most unusual object which is the nearest protostellar jet visible in the optical.

4.6 Conclusions

From the three-dimensional numerical simulations of interacting binary jets, several results are apparent.

- For the underdense jets in this simulation, when the jets interfere, either they survive as two jets if the sources have a large spatial or angular separation, or merge into one single jet if the sources have a small spatial separation. Dense ballistic jets are however much less likely to interact than light jets.
- Using the observed parameters as far as possible, the kink and projected bending of the secondary jet has been reproduced as observed for LDN1551 IRS 5.
- Over a long time-scale, precession induced by the orbital motion of the source is seen. On the short lifetime of the jets from LDN1551, this effect is negligible.
- If the jets are not strictly parallel, as in most of the limited set of observed binary protostellar jets, it is shown that the toroidal magnetic field like the one simulated here, in the ambient medium though which the jets propagate, can help the collimation and refocusing of both the jets.
- In the comparison of the emission maps against the observations it is shown that the kink structure of interacting jets is still apparent in the synthetic observations.

"You cannot step in the same river twice"

Heracleitus, quoted in Plato, Cratylus, 402a

5

Jet Recollimation and Acceleration in an Evacuated Cavity

In this Chapter, we present simulations of jet propagation through an ambient medium which we have envisioned as being evacuated by a previously propagating jet or is a natural cavity in an inhomogeneous molecular cloud. We show the collimative and accelerative effects on the jet and compare with the standard case of a uniform density medium propagation. We have investigated the effects of ambient material on the collimation and internal structure (specifically shocks) of the jet. We explore a parameter space of the jet-to-ambient density ratio and the size of the density decrement in the cavity, as well as the inclusion of (atomic) radiative cooling. We demonstrate that the presence of a cavity can strongly recollimate the jet - although this effect is lessened if radiative cooling is present. The cavity also strongly accelerates radiative and non-radiative jets alike by up to fifty per cent.

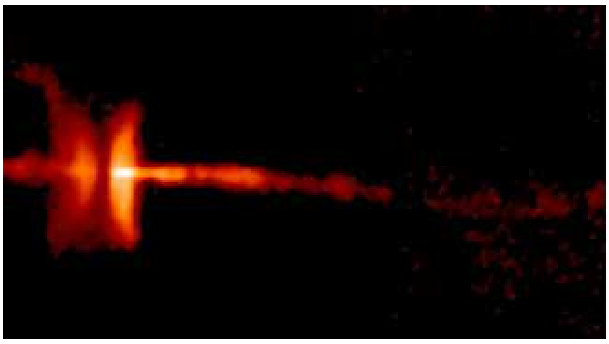

Figure 5-1: *HH30, a high velocity (v_{jet} ~ 200 km s^{-1}), highly collimated (opening angle ~ 2° degrees) jet from a young star. Image from Alan Watson (UNAM, Mexico), Karl Stapelfeldt (JPL), John Krist (STSI) and Chris Burrows (ESA/STSI)*

5.1 Introduction

Jets from young stellar objects are remarkable for their high velocities and unusually collimated morphologies, extending up to parsec scales with opening angles of $0 - 3°$ (Eislöffel et al. 2000). The magnetic field anchored in the disk is thought to be responsible for both phenomena. By means of the Lorentz force, the magnetic field accelerates matter escaping from the disk from breakup velocity to the typical optical jet velocities of 300 km/s. Additionally the YSO jets are thought to be self-collimated by means of their own magnetic field. The jet, on entering the molecular cloud is greeted with a complex environment shaped by turbulence, magnetic fields, gravitational infall and the effects of other outflows and jets. The molecular cloud may exert a strong influence on the formation, acceleration and collimation of the jet. The effect of gravitational infall may be examined analytically by means of the circulation or transit flow model. The effect of previous outflows from the same source may be explored using numerical simulations.

5.1.1 Motivation: Circulation Model

The circulation or transit flow model is an analytical self-similar solution to the steady-state MHD equations. Fiege & Henriksen (1996), Lery et al. (1999), Lery et al. (2002) and Combet et al. (2006) have solved the self similar equations. They have shown a number of features including a strong density gradient towards the z-axis. The density gradient is found for both weakly magnetised and strongly magnetised solutions. The density gradient is naturally created by the infalling material encountering a higher thermal pressure near the central object causing the infall to deviate into an outflow. The circulation model is one dimensional and collapses two spatial dimensions (r,θ) onto

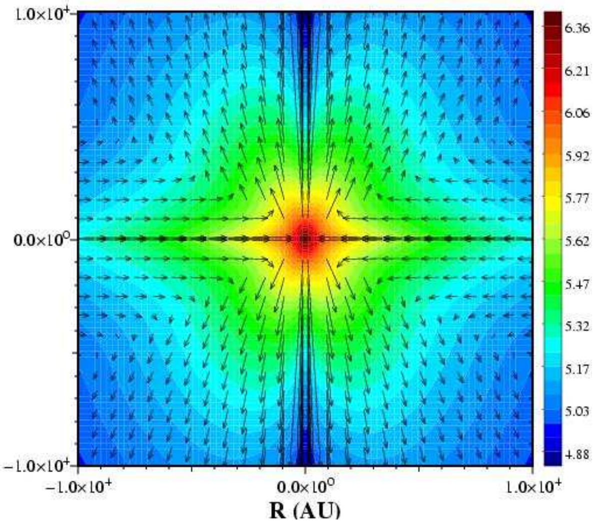

Figure 5-2: *The circulation model: the densities are shown in log scale colour and the velocity field is shown by the arrows. From Combet et al. (2006).*

one self-similar variable. Hence the solution cannot strictly reach either the z-axis or the equator and can only be applied between θ_{max} and θ_{min}, where ($\theta_{min} > 0$ and $\theta_{max} < \frac{\pi}{2}$). Nevertheless the solutions indicate evidence for a density decrease towards the axis precisely where the jet will propagate. The density gradient towards the z-axis as derived in the circulation model is shown in Figure 5-2 (Combet et al. 2006). The idea of the simulation is to launch a jet into the solution of the transit flow and see its effects on the jet morphology and dynamics.

5.1.2 Motivation: Prehistory of Jets and Outflows from the Source

The prehistory of outflows from the same source generates channels which affect the succeeding outflows from the same source. Quillen et al. (2005) show that such a channel will take 10^6 years for the molecular cloud to diffuse back into the channel. Therefore the cavity will remain open long enough for successive outflows to propagate into and along it.

5.1.3 Recollimation

Jets may be collimated by external hydrodynamic pressure or by the toroidal pressure of a wound-up magnetic field. Far from the protostar the magnetic field diminishes by orders of magnitude and it is reasonable to assume that magnetic forces play a smaller role in recollimation at distances of ~ 100 AU. Some collimation of the jet may be caused by its environment; there are a number of theories e.g. toroidal magnetic fields existing in the ambient medium, the pressure exerted by the molecular cloud collapsing inwards, or just the presence of a cavity surrounded by dense walls which force the jet to become collimated. As far back as Königl (1982) and Raga & Canto (1989) de Laval nozzles were thought to be responsible for the initial collimation of an outflow. More recently Mellema et al. (1991); Icke et al. (1992a) and Icke et al. (1992b) investigated "shock-focused" inertial confinement, where oblique inward facing shocks are produced by jet interaction with a toroidal density distribution in the ambient medium (Frank et al. 1998) in the context of planetary nebulae and Frank & Noriega-Crespo (1994) applied this to jets in young stellar objects (YSOs). Frank & Mellema (1996) (hereafter FM) modelled a central wind from a YSO interacting with a toroidal density distribution. Mellema & Frank (1997) (hereafter MF) explored the same problem this time including the effects of atomic radiative cooling. Gardiner et al. (2003) (hereafter GFH) simulated wide-angle winds interacting with a collapsing environment and a toroidal magnetic field. Opher et al. (2004) (hereafter OLV) modelled the formation of a jet by a de Laval nozzle effect, which includes lateral variations in the magnetic field. FM, MF and GFH all used 2D simulations, either axisymmetric or spherically symmetric. OLV performed a fully 3D simulation however they used a magnetic field to perform the collimation rather then a density gradient. In this chapter the possibility of additional collimation of a jet by a reduced density in the environment and the observational consequences to the underlying flow is investigated.

5.2 Method

5.2.1 Numerical method

In this study, we will primarily vary two parameters, the ratio of the jet density to ambient density η and the reduction of density of the ambient medium in the centre of the cavity, the density decrement, δ. The parameter space is explored using the numerical code FLASH (Calder et al. 2002). Using these results a larger simulation is carried out using the numerical code ATLAS described in Chapter 2. The hydrodynamical equations are evolved in time, in 2.5D and 3D.

5.2.2 System of equations

The simulation code solves the ideal hydrodynamics (HD) equations. The equations are expressed in terms of the 3 quantities (1 vector and two scalar) in addition to time t which are conserved in a volume: density ρ, momentum, $\rho\mathbf{u}$, and energy density, E.

$$\frac{\partial \rho}{\partial t} + \nabla \cdot (\rho \mathbf{u}) = 0 \tag{5.1}$$

$$\frac{\partial}{\partial t} (\rho \mathbf{u}) + \nabla \cdot \left[\rho \mathbf{u}\mathbf{u} + (p)\, \bar{\bar{\mathbf{I}}}\right] = 0 \tag{5.2}$$

$$\frac{\partial E}{\partial t} + \nabla \cdot [(E + p)\, \mathbf{u}] + L_{cooling} = 0 \tag{5.3}$$

$$E = \frac{1}{2}\rho u^2 + \frac{p}{\gamma - 1} \tag{5.4}$$

$L_{cooling}$ represents the losses due to optically thin radiative cooling. The units are chosen so that $\mathbf{B}$ absorbs a factor of $1/\sqrt{4\pi}$. The adiabatic index is $\gamma = 5/3$ for a monatomic gas throughout the simulations. The equation of state is the ideal gas equation (p=nkT). The same atomic radiative cooling function is used in both ATLAS and FLASH, and is described in Section 2.2.8.

5.2.3 Initial and boundary conditions

The values of the hydrodynamic variables are set to those appropriate for Class I protostellar jets. The main parameters of these solutions are described in Table 5.1.

5.2.3.1 Initial conditions

The ambient medium is initialised with a uniform density (1×10^{-22} g cm^{-3}) and temperature (10 K) and the jet is initialised with the temperature of 1000K and density of $\eta \times 10^{-22}$ g cm^{-3} and velocity of 300 km s^{-1}, a typical YSO jet velocity (Eislöffel et al. 2000). For the 3D simulation only a velocity radial profile similar to the one used in Chapter 4 is used. The velocity radial profile is a positive cosine - with its maximum, v$_{jet}$ at r=0 in the jet centre, dropping to zero at r$_{jet}$.

The evacuated cavity is parametrised using the sinusoidal function:

$$\rho\,(x) = \rho_0 \left(\frac{\delta + 1}{2\delta}\right) \left(1 + \cos\left(\frac{\pi}{2}\frac{x}{r_{jet}}\right)\right) \tag{5.5}$$

where the density decrement, δ is the parameter chosen to represent the size of the cavity, δ =1, or 10.

Domain	$8 \times 10^{16}\text{cm} \times 3.2 \times 10^{17}\text{cm}$
Jet velocity	$v_{jet} = 300$ km s^{-1}
Jet density	$\rho_{jet} = 1\eta \times 10^{-22}$ g cm^{-3}
Ambient density	$\rho_a = 1 \times 10^{-22}$ g cm^{-3}
Jet Temperature	$T_{jet} = 10^3 K$
Jet Radius	$r_{jet} = 1 \times 10^{16}\text{cm}$
Ambient Temperature	$T_a = 10K$

Table 5.1: *Parameters used in the numerical calculations*

	η	Cooling	Pulsed
Case I	10	N	Y
Case II	0.1	N	Y
Case III	1	Y	N
Case IV	1	Y	Y

Table 5.2: *Parameter Space*

5.2.3.2 Boundary conditions

For the 3D simulation, the boundary conditions are inflow for $r < r_{jet}$, reflecting for $r > r_{jet}$ along the inner r-boundary (z=0) and outflow along all other boundaries.

For the axisymmetric simulations, the boundary conditions are identical, except for an extra reflecting boundary condition on the z-axis.

5.3 Results

5.3.1 Parameter space exploration

A jet entering an evacuated cavity is modelled. The jet is forced inwards by the steep density gradient of its environment. The parameters varied are, the density ratio, η and the density decrement, δ, which is defined above. The effects of rapid velocity variation (pulsing) and radiative cooling are examined.

5.3.2 Case I: Pulsed, overdense adiabatic jets in cavities

The first case is an overdense jet propagating into an evacuated environment. (see Figure 5-3). This case includes two simulations with a constant density ambient medium and a density decrement of 10. In both simulations the jet was initialised as cylindrical, with a nominal Mach number with respect to the ambient sound speed of 800. The inlet velocity is pulsed with an amplitude of 30% in order to reproduce the knots visible in observations. It expands in typical adiabatic fashion and has a low length-to-width ratio ∼2.5. The effect of adding an evacuated cavity, with a density decrement, δ = 10 is to produce increased collimation well behind the bow shock. The length-to-width ratio is ∼5. The jet is compressed toward the axis and small structures are visible. However behind the head of the jet the jet evolves similarly to the CDAM jet, so the effect is only a transient one, and only the first few “knots” see the cavity. The dense “interstellar bullets” at the head of the jet effectively plough the cavity structure out of the way.

5.3.3 Case II: Pulsed, underdense adiabatic jets in cavities

The second case was an underdense jet propagating into an evacuated environment. (see Figure 5-3). This simulation has much in common with the first case. However for the underdense jet case, the jet behaves more like an expanding bubble and is more strongly and dramatically affected by the cavity, the aspect ratio increases from 2.5 in the CDAM to 6.4 in the evacuated case. The jet in the cavity has a bow shock advance speed of $0.5v_{jet}$, and at t=634 years, the cavity jet has already crossed the grid, whereas the CDAM jet has an advance speed of only 0.25 v_{jet}. Characteristics associated with Kelvin-Helmholtz instabilities are highly visible in the cocoon. The initially flat, top-hat profile pulses become distorted as the jet propagates further into the cavity.

5.3.4 Case III: Steady, radiatively cooling jet in cavity

In the third case strong radiative cooling has been enabled in the simulation. For clarity, the 30% variation in the inlet velocity has been removed. The effect of the evacuated cavity on cooling instabilities inside the cocoon and on the bow shock surface is shown in Figure 5-5. The pressure gradient compresses the cocoon and narrows the cavity swept out by the fast jet. The distinctive tendril features evident in right panel of Figure 5-5 (between 5×10^{16} cm and 1×10^{17} cm) are absent in the cavity case. The strong acceleration of the bow shock is still present. The effect of the radiative cooling is to drain thermal pressure from the cocoon and collapse the bow shock. The radiative jets are thus more narrow, the aspect ratios increase to 8 for the cavity case and 4.4 for the CDAM case. There is a relative decrease in the amount of collimation from the adiabatic to the non-adiabatic case, which could possibly be attributed to the formation of a dense plug of material at the head of the jet, which cannot be much further compressed by the ambient medium (visible on the y-axis at 3×10^{17} cm).

5.3.5 Case IV: Pulsed, non-adiabatic jet in cavity

In the fourth case strong radiative cooling has been enabled in the simulation. The 30% variation in the inlet velocity has been restored. A much more varied morphology is present in both the CDAM and the cavity case. The aspect ratio increases from 4 to 6.1 in the evacuated case.

5.3.6 Pulsed, non-adiabatic, three-dimensional jet in cavity

Using the code ATLAS (see Chapter 2) a full three-dimensional simulation is performed. In the 3D case the resolution is lower than can be achieved in 2.5D. As a result the jet appears smoother and less instabilities. The comparison between the cavity and CDAM jets again shows the basic differences of acceleration, cooling and recollimation (see Figure 5-7). By calculating the emissivity in each cell and integrating through the 3D domain, emission maps of the Hα line are produced. In the 3D simulation with the density decrement of δ=10 shown in Figure 5-7 the jet narrows sufficiently so that it is only spanned by 20 or so cells. This results in some false structures which are visible in the lower part of the emission map (Figure 5-8).

5.4 Discussion

5.4.1 The effects of collimation and acceleration

In the adiabatic cases, both Case I and Case II, there is extremely strong recollimation of the jet by the environment. However in the overdense case, the dense bullets quickly overrun the evacuated cavity so the morphology is really only affected near the leading part of the jet. In the underdense case the same argument applies. However, including radiative cooling, (Case II and IV) the collimation is not so pronounced and the development of instabilities is hindered by the cavity. This may be due to a combination of the pressure gradient compressing the jet towards the axis and the fact that the jet travels more quickly, so the instabilities have less time to develop and are more elongated when they do develop.

5.4.2 Observational signatures of the circulation model

There are three possible main observational signatures of evacuated cavities. The actual jet recollimation is quite gradual and would require high-resolution imagery over long distances for confirmation. The acceleration by the cavity is also not a promising observational signature, as it require monitoring the jet over a long time period. The decrease in radiative cooling losses may make the jet harder to observe when it enters a cavity.

5.4.3 Prehistory of jets

The effects of collimation and acceleration caused by the evacuated cavity in the ambient medium are shown for both 2.5D (see Figure 5-6) and 3D (see Figure 5-7).

5.5 Conclusions

- Strong recollimation is demonstrated for parameters appropriate to Class I protostellar jets.
- Strong acceleration is obtained far from the protostar for parameters appropriate to Class I protostellar jets.
- A dependence of acceleration and collimation on η and density decrement, δ is established.
- New possible methods for detecting the observational signatures of the circulation model are proposed.
- For the investigated parameters, the density and pressure gradient appears to compress the cocoon and the density reduction in the path of the bow shock decreases the amount of vortex shedding and mixing, resulting in a less morphologically rich cocoon environment.

	Density Decrement	Aspect Ratio	Bow Shock Advance Speed
Case I	1	2.5	240 km/s
	10	5	340 km/s
Case II	1	2.5	73 km/s
	10	6	156 km/s
Case III	1	4.4	151 km/s
	10	8	223 km/s
Case IV	1	4	136 km/s
	10	7.1	223 km/s

Table 5.3: *Jet aspect ratios and bow shock advance speeds for cases I-IV*

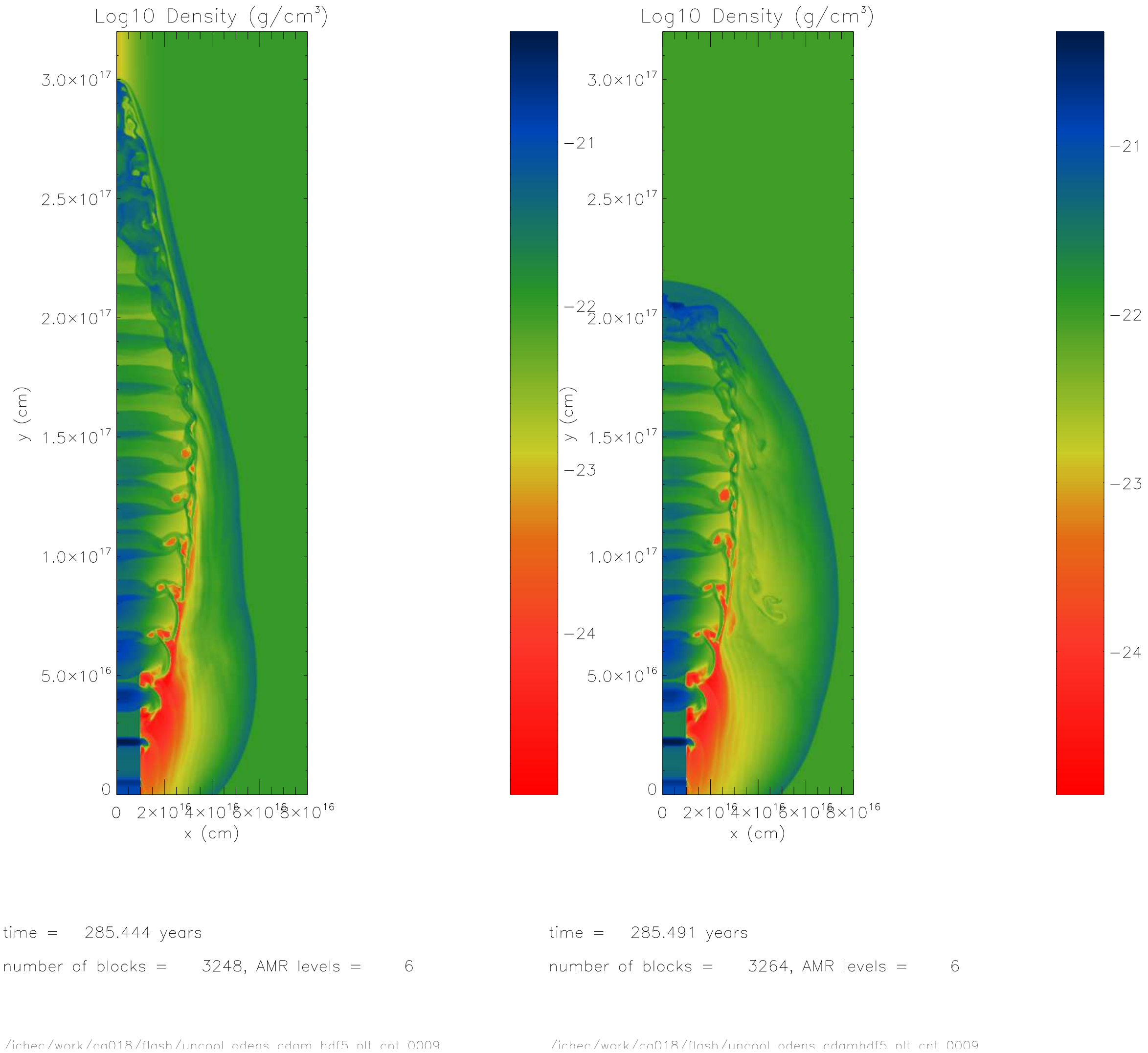

Figure 5-3: *Overdense (η=10), 300 km s^{-1}, Mach 800 adiabatic jet, velocity-pulsed with an amplitude of 30% and a period of 9.6 years (3×10^8 s) injected into (left panel) an evacuated cavity, with density decrement, δ=10. Strong recollimation and rapid acceleration are evident, compared with the right panel, which shows an identical jet in constant density ambient medium (CDAM). The box is an axisymmetric rectangle 3$\times$10^{17} cm by 8$\times$10^{16} cm. An adaptive grid is used with 6 levels of refinement, and a resolution equivalent to 256x1024-sized uniform mesh.*

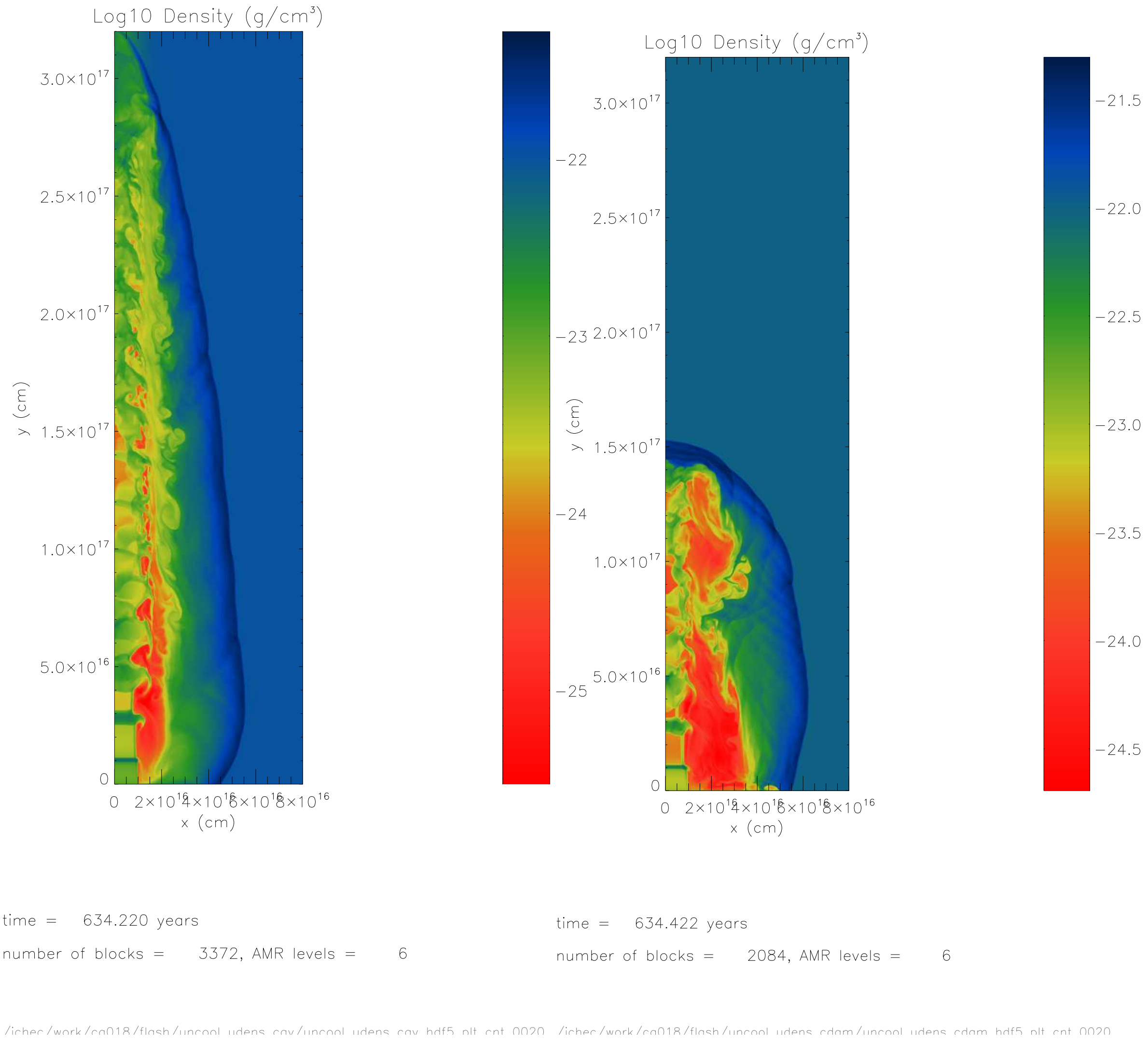

Figure 5-4: *Underdense (η=0.1), 300 km s^{-1}, Mach 800 adiabatic jet, velocity-pulsed with an amplitude of 30% injected into (left panel) an evacuated cavity with density decrement, δ=10, (right panel) a constant density ambient medium (CDAM). The acceleration is most pronounced in this case.*

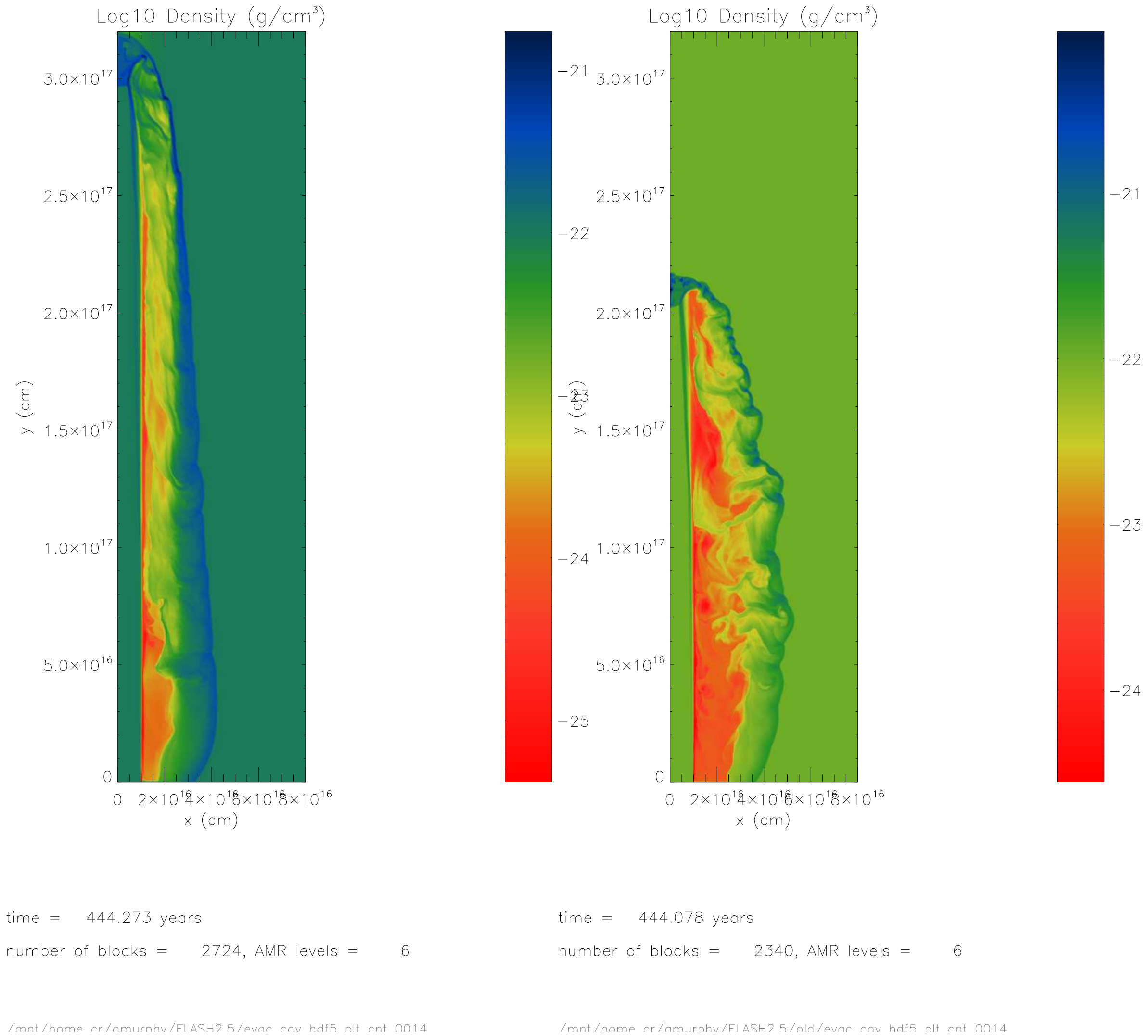

Figure 5-5: *Left panel: Steady, radiatively-cooled jet in evacuated cavity, with density decrement, δ=10 and η=1 Right panel: Identical jet in constant density ambient medium, with η=1 With strong radiative cooling typical of protostellar jets, recollimation is less apparent. The cooling instabilities are much less evident.*

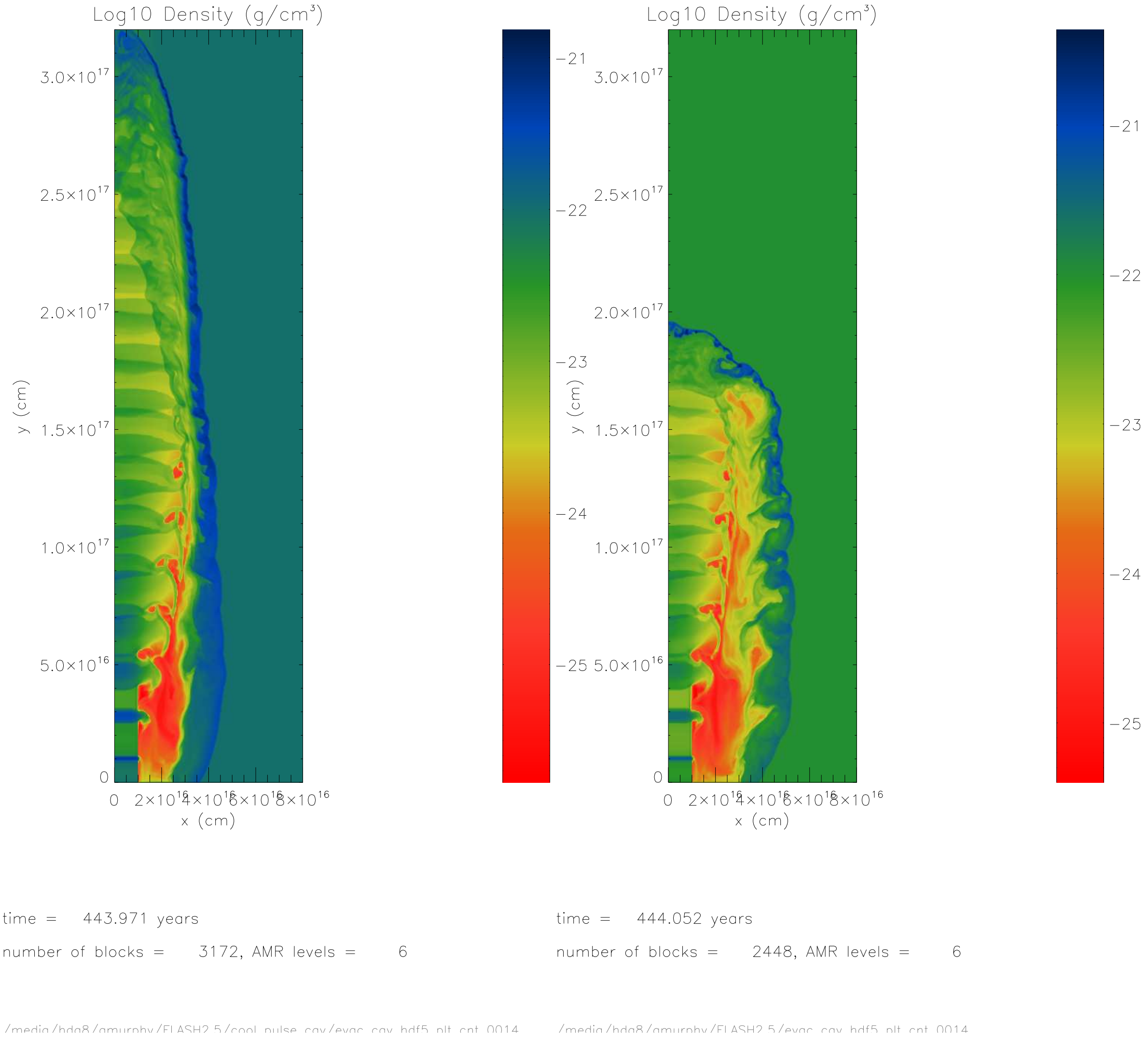

Figure 5-6: *Left panel: Jet in evacuated cavity, with density decrement, δ=10 and η=1 Right panel: Jet in constant density ambient medium, with η=1 With strong radiative cooling typical of protostellar jets, recollimation is less apparent. The cooling instabilities are much less evident.*

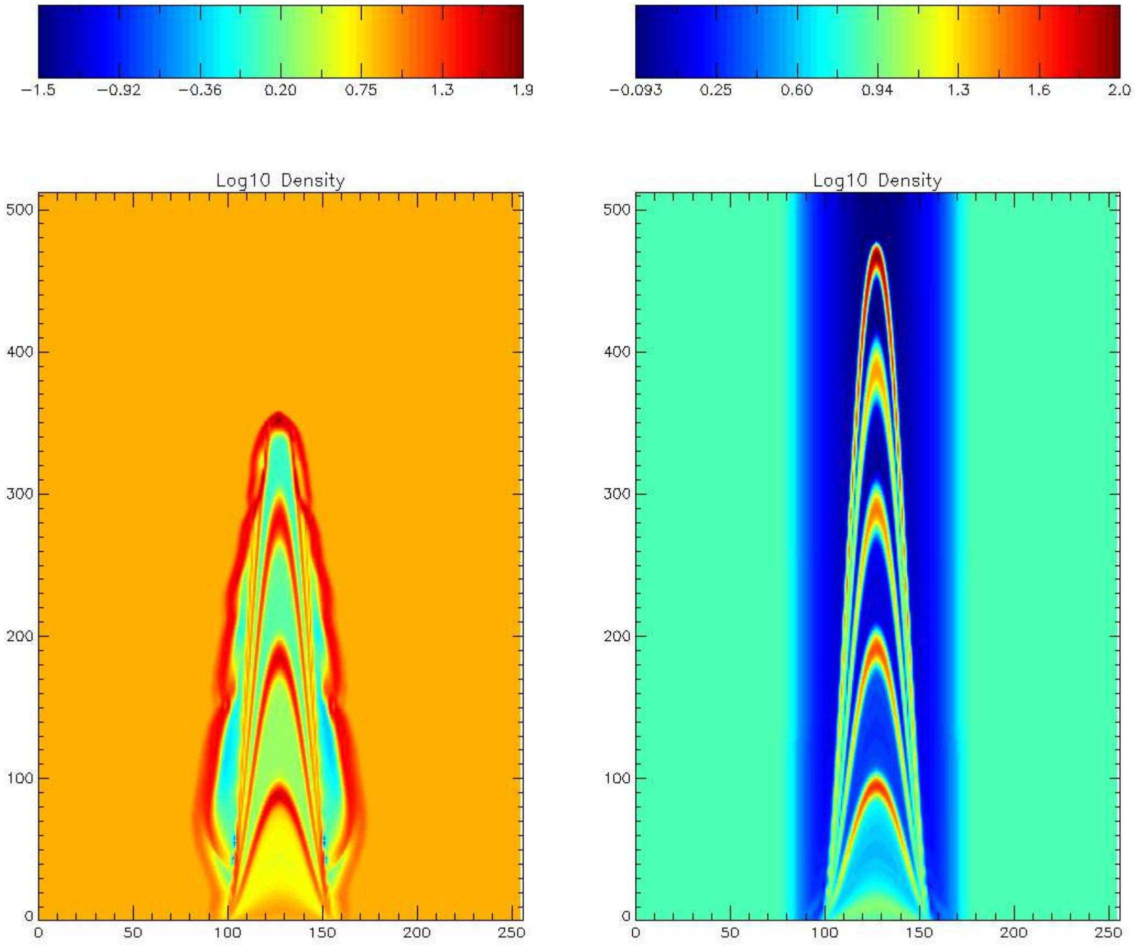

Figure 5-7: *Left panel: Logscale density for 3d jet simulation without evacuated cavity at time t=588 years. Right panel: Logscale density for 3d jet simulation in evacuated cavity at the same time.*

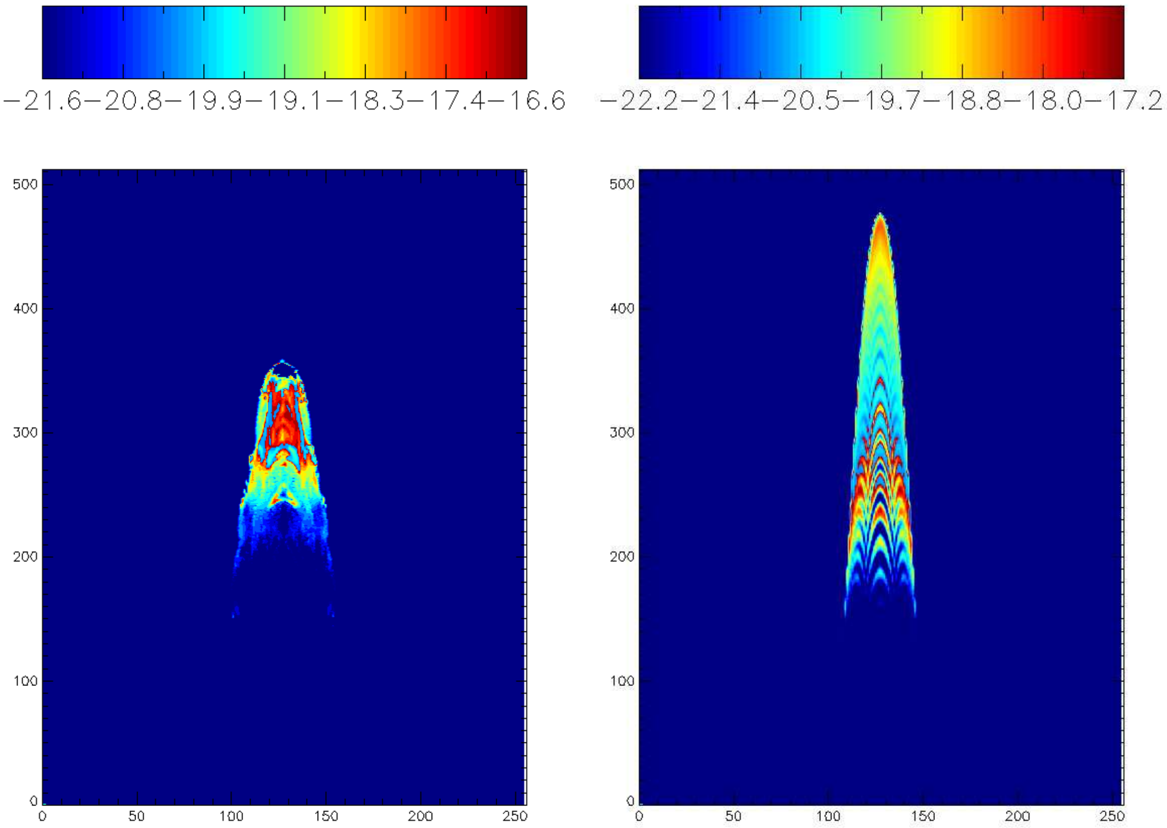

Figure 5-8: *Left panel: Logscale Hα line emission for 3d jet simulation without evacuated cavity Right panel: Logscale Hα line emission for 3d jet simulation in evacuated cavity*

“ ... omnium rerum simulatio vitiosa est (tollit enim iudicium veri idque adulterat) ... delet enim veritatem”

Marcus Tullius Cicero, *Laelius De Amicitia*, 44 BC

6

Conclusions and Future Work

In this chapter we present a synopsis of the thesis work and give an outline of further work to be done.

6.1 Code Testing and Code Comparison

A new MHD code was modified to include the effects of radiative cooling and to be able to simulate binary jets from orbiting sources in three dimensions (see Chapter 2). The code was comprehensively tested using both experimental results and standard tests from the literature. The tests included both purely hydrodynamical results in one and two dimensions and magnetohydrodynamical problems. A simulation of the Orszag-Tang vortex was compared with published results to test the ability of the code to maintain divergence of magnetical field equal to zero. Furthermore, a code comparison was performed to establish the veracity of our results for problems relevant to astrophysical jets.

6.2 Jets from Binary Protostars

The propagation and evolution of binary jets was studied for a range of conditions (see Chapter 3). Previous work on simulations of jets from young stars (see Chapter 1 for a summary) have mainly been focused on single jets, although a significant proportion of stars are binaries. The frequency of binary jets is low compared to the frequency of single jets observed from protostars. In Chapter 3 we examined the effect of having a source in orbital motion using a numerical simulation. The orbiting jets have to do extra work moving the ambient medium in a transverse direction, which has the effect of a transverse wind shredding the jet. We found that while orbital motion could contribute to a twisted morphology and eventual breakup, the source motion required exceeds the observed values (e.g. for the case of the young binary LDN1551 IRS 5) by an order of magnitude.

The lateral expansion of a jet can have a significant effects for a young binary jet. If the sources are close together, as in a close binary, the bow shock of one jet can distort the beam of the secondary jet. For the hydrodynamic case, it was shown that jets from LDN1551 IRS 5 interact strongly due to thermal pressure of the fast jet's bow shock upon the beam of the slow jet. In order to compare this result against observations, the fraction of ionized hydrogen in each cell was tracked during the simulation and the [SII] line emission was calculated. A peak in the emission where the bow shock strikes the beam was found. This is at approximately the same location as a bright "knot" seen in the HST [SII] images.

To study the effect of the magnetic field on the jet interaction a toroidal magnetical field was introduced. Observations of a high degree of polarization in LDN1551 at optical, infrared and submillimetre wavelengths imply an ambient magnetic field is present. It is shown that the effect of the toroidal field is to exert a hoop stress on the jet pair and thus force together the diverging pair of jets. This effect is seen in the observations of LDN1551 IRS 5 where the jets initially diverge but then turn to pursue a roughly parallel course.

In summary, the results of this section show that orbital motion has little effect on the stability and lifetime of a binary jet. However when two jets are present, a faster one can dominate its slower companion and this can account for the paucity of binary jets in the observations. The presence of a magnetic field in the observed configuration can provide further redirection and enhance the interaction of the two jets until they appear to almost merge.

6.3 Jets in Evacuated Ambient Media

The propagation in jets in partially evacuated ambient media was studied (see Chapter 5). The aim of the Chapter was to show that the prehistory of the outflows and jets from the same source affects the current outflow. A secondary aim was to show the effects of a jet on the circulation model. Although much previous work on jet propagation has been done, many studies assume that the jet is the first to propagate into its environment without assuming any prehistory of jets. In addition many studies assume a uniform density and pressure without lateral variation. This assumption is removed in the present work, which models a jet entering a cavity. We study the effects of the cavity on jets of different densities, with and without pulsing and cooling and try an identify the effect of such a cavity on observable quantities such as the speed, the aspect ratio and the morphology. A range of simulations were performed in both axisymmetry and 3D. The effects of varying the presence of cooling, velocity variation in the input, and different jet-to-ambient density ratios for cavities of different sizes were examined. The density function of the cavity was parametrised in order to provide a measurable quantity. This thesis shows three major effects of the evacuated cavity on the collimated jet.

- Recollimation. Using the aspect ratio to measure the amount of collimation, we find consistently large increases up to 140% for one case. This results clearly shows that the prehistory and ambient environment can have a large effect on the recollimation of a jet as it propagates outward from the source.

- Acceleration. In all cases where a cavity is present, advance speeds are increased, consistent with analytical predictions from one-dimensional ram pressure balances.

- An overall decrease in the amount of structures associated with instabilities in the cocoon is seen. Linear theory implies the growth rate for the Kelvin-Helmholtz instability is inversely proportional to the Mach number, so this results is consistent with the increased Mach number of the accelerated, recollimated jets. number of the jet.

The hydrodynamic pressure exerted by the walls of the cavity compresses and focuses the cocoon in all cases. The centre of the cavity also has much less material to resist the incoming shock and there is a resulting acceleration in the jet. The combination of compression and acceleration greatly reduces the amount of cooling instabilities. Signs of jets entering cavities such as these may be used to identify examples of circulation flow in observations.

6.4 Future Work

6.4.1 Jets from Binary Protostars

The propagation and interaction of jets is a very broad area and contains several practical future research directions. There are still several outstanding problems with binary jets from young stars. An important question is whether the results based on observed quantities of LDN1551 IRS 5 can be generalised. A major requirement for further progress in direct simulation is a larger number of observational samples of binary jets. The number of observations remains low - approximately 10 sources. An observational search for binary jets in star forming regions would be able to add extra constraints to the model. In particular, a better constraint on the geometry of the magnetic field, which may be obtained using polarimetry, is desirable. While the best resolution available was used in this thesis along with modern adaptive grid techniques, resolution is still relatively low in three dimensions. A higher resolution study would give a more accurate quantitative estimate of the emission from the interaction region. Furthermore, in order to compare results with observations properly, it would be desirable to include a chemical network in the code, so emission maps for additional species, such as CO, could be produced. A future study could include the effects of precession as well as orbital motion. Precessing jets will have enhanced interaction and are likely to show increased dynamical instability.

Another open question concerns the production of X-rays from binary jets. As discussed in Chapter 4, the generation of X-rays from shocks in the case of L1551 IRS 5 requires velocities which are greater than those inferred from observations at other wavelengths. Imagining the binary jet system as a pair of mutually orbiting flux tubes, the probability of reconnection events occurring immediately springs to mind. For a physically meaningful study of reconnection processes within the binary jet, use of non-ideal MHD techniques such as e.g. Hall-MHD would be desirable. Some progress, however can be made studying using resistive MHD. As a preliminary step towards this, we have modelled 3D reconnection processes in a current sheet, over a range of perturbation modes. The purpose of the study is to constrain the large amount of thermal energy released in the reconnection process. For wave modes with $k > 1/a$, where k is the wave number and a is the current sheet thickness, along with the release of thermal energy, we observe in early simulations the formation of magnetic islands on the current sheet, which are usually associated with the tearing mode instability. Encouragingly, the critical value is in agreement with that found through the MHD analysis in the linear regime by Furth et al. (1963). Three-dimensional studies of the nonlinear regime are ongoing.

6.4.2 Jets in Evacuated Cavities

The evacuated cavity model for jet recollimation can be further enhanced by including a treatment of the magnetocentrifugal wind launching mechanism. This is a non-trivial problem, and necessitates the inclusion of gravity and magnetic field. An internal boundary is necessary around the gravitational source to prevent numerical difficulties when the radius approaches zero. Non-ideal effects such as resistivity are needed to allow accreting matter to slip through the magnetic field lines and gravitate towards the central object. Cooling is required within the disk to compensate for the effect of Joule heating, which tends to puff up the disk. Zanni et al. (2007) give a comprehensive treatment of the subject. We have performed such a simulation in order to calculate the size of the cavity generated by such a wind. We have also increased the domain of the simulation to study the long term evolution of the MHD wind model, examine the effects of boundary conditions on the jet collimation, and compare against observations of rotation in star formation jets. This required the use of a stretched grid in order to keep the simulation down to a manageable amount of computational time and data. The simulation also requires a greatly increased number of timesteps (an order of magnitude greater then in previous work), due to the much larger Keplerian rotation period in the outer edges of the disk. In Figure 6-1 a plot of the large-scale MHD disk wind simulation is shown. The bow shock, collimated disk wind and the disk itself are all present. The cavity formed may be clearly seen to the left of the image. It expands initially but then is recollimated along with the rest of the jet near to the bow shock. The simulation is still dynamically evolving and has not reached a quasi-stationary state yet. An important further study is to compare the results of the simulation to measurements of the jet rotation using Doppler gradients.

Another important application of this model is outside the star formation regime, for microquasars and AGN jets. In the two-flow scenario, a classical MHD wind of the type shown in Figure 6-1 confines a highly relativistic electron-positron pair plasma beam (Henri & Pelletier 1991). The MHD outflow plays a dual role in the model. It provides a cavity in which the electron-positron beam can propagate. The outflow also prevents catastrophic Compton cooling from decelerating the electron-positron beam by reheating it through second-order Fermi mechanism thus allowing it to reach velocities approaching light speed (typically 92-99%, Renaud & Henri 1998). This acceleration mechanism can explain the apparently superluminal motions near black-hole X-ray binaries observed by Mirabel et al. (1992). See Mirabel & Rodríguez (1999) for a review of observations of galactic superluminal sources. The goal of this study is investigate the feedback between the two flows, in particular the effect of a strongly heated and episodic set of outburst on a collimating MHD wind. The MHD model is used to calculate the mean magnetic field and the radius of the inner cavity as a function of height. These constraints are then used to calculate the particle density and thermal energy of the plasma inside the cavity using a relativistic particle code (Saugé & Henri 2006). An internally consistent model for ejections from black-hole X-ray binaries will then be obtained.

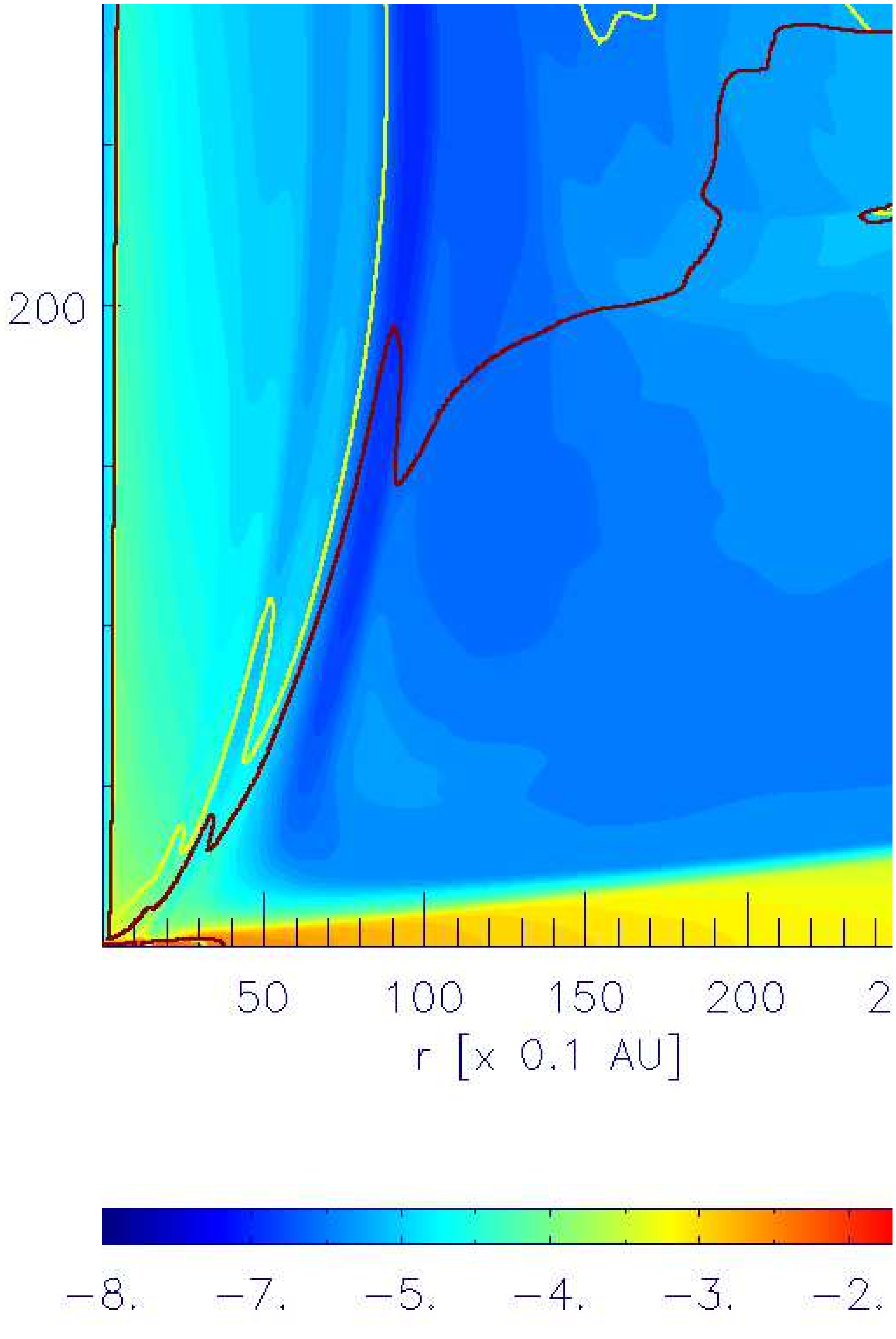

Figure 6-1: *Log density colourmap of axially symmetric MHD disk wind simulation at t=63. (Time units are Keplerian periods a the disk inner radius) As the disk wind moves upward from the disk it becomes collimated. The fast magnetosonic and Alfvén surfaces are plotted as yellow and black contours respectively.*

Bibliography

Andre, P., Ward-Thompson, D., & Barsony, M. 1993, ApJ, 406, 122

Anglada, G. 2004, in Revista Mexicana de Astronomia y Astrofisica Conference Series, 100–103

Anglada, G., Estalella, R., Rodriguez, L. F., et al. 1991, ApJ, 376, 615

Anglada, G., Rodriguez, L. F., & Torrelles, J. M. 1996, ApJ, 473, L123+

Anglada, G., Rodriguez, L. F., & Torrelles, J. M. 1998, in ASP Conf. Ser. 132: Star Formation with the Infrared Space Observatory, 303–+

Avery, L. W., Hayashi, S. S., & White, G. J. 1990, ApJ, 357, 524

Bacciotti, F. 2002, in Revista Mexicana de Astronomia y Astrofisica Conference Series, 8–15

Bacciotti, F., Chiuderi, C., & Oliva, E. 1995, A&A, 296, 185

Bacciotti, F. & Eislöffel, J. 1999, A&A, 342, 717

Bacciotti, F., Mundt, R., Ray, T. P., et al. 2000, ApJ, 537, L49

Bachiller, R. 1996, ARA&A, 34, 111

Bachiller, R., Fuente, A., & Tafalla, M. 1995, ApJ, 445, L51

Balbus, S. A. & Hawley, J. F. 1991, ApJ, 376, 214

Bally, J., Feigelson, E., & Reipurth, B. 2003, ApJ, 584, 843

Balsara, D. S. 1998, ApJS, 116, 133

Balsara, D. S. & Spicer, D. S. 1999, Journal of Computational Physics, 149, 270

Berger, M. J. & Colella, P. 1989, Journal of Computational Physics, 82, 64

Berger, M. J. & Oliger, J. 1984, Journal of Computational Physics, 53, 484

Bertout, C. & Regev, O. 1992, ApJ, 399, L163

Beuther, H., Churchwell, E. B., McKee, C. F., & Tan, J. 2005, Protostars and Planets V, 815

Bieging, J. H. & Cohen, M. 1985, ApJ, 289, L5

Blandford, R. D. & Payne, D. G. 1982, MNRAS, 199, 883

Blandford, R. D. & Rees, M. J. 1974, MNRAS, 169, 395

Blondin, J. M., Fryxell, B. A., & Königl, A. 1990, ApJ, 360, 370

Bonito, R., Orlando, S., Peres, G., Favata, F., & Rosner, R. 2004, A&A, 424, L1

Bonnell, I. A., Bate, M. R., Clarke, C. J., & Pringle, J. E. 1997, MNRAS, 285, 201

Bonnell, I. A., Bate, M. R., & Zinnecker, H. 1998, MNRAS, 298, 93

Bonnell, I. A., Vine, S. G., & Bate, M. R. 2004, MNRAS, 349, 735

Boris, J. & Book, D. 1973, Journal of Computational Physics, 23, 38

Brio, M. & Wu, C. C. 1988, Journal of Computational Physics, 75, 400

Calder, A. C., Fryxell, B., Plewa, T., et al. 2002, ApJS, 143, 201

Camenzind, M. 1990, Reviews of Modern Astronomy, 3, 234

Chen, P. F., Wu, S. T., Shibata, K., & Fang, C. 2002, ApJ, 572, L99

Chernin, L. M. & Masson, C. R. 1991, ApJ, 382, L93

Chernin, L. M. & Masson, C. R. 1995, ApJ, 455, 182

Chevalier, R. A. & Imamura, J. N. 1982, ApJ, 261, 543

Choudhuri, A. R. 1998, The physics of fluids and plasmas : an introduction for astrophysicists / (The physics of fluids and plasmas : an introduction for astrophysicists / Arnab Rai Choudhuri. New York : Cambridge University Press, 1998. QB466.F58 C46 1998)

Clarke, D. A., Norman, M. L., & Burns, J. O. 1986, ApJ, 311, L63

Cliver, E. W., Webb, D. F., & Howard, R. A. 1999, Sol. Phys., 187, 89

Colella, P. 1990, Journal of Computational Physics, 87, 171

Colella, P. & Woodward, P. 1984, Journal of Computational Physics, 54, 174

Combet, C., Lery, T., & **Murphy**, G. C. 2006, ApJ, 637, 798

Cudworth, K. M. & Herbig, G. 1979, AJ, 84, 548

Curtis, H. D. 1918, Publications of Lick Observatory, 13, 55

Dai, W. & Woodward, P. R. 1998, ApJ, 494, 317

de Gouveia dal Pino, E. M. & Benz, W. 1993, ApJ, 410, 686

de Hoffmann, F. & Teller, E. 1950, Physical Review, 80, 692

Dedner, A., Kemm, F., Kröner, D., et al. 2002, Journal of Computational Physics, 175, 645

DeZeeuw, D. & Powell, K. G. 1993, Journal of Computational Physics, 104, 56

Downes, T. P. 1996, Ph.D. Thesis

Draine, B. T. 1980, ApJ, 241, 1021

Draine, B. T. & McKee, C. F. 1993, ARA&A, 31, 373

Duquennoy, A. & Mayor, M. 1991, A&A, 248, 485

Dyson, J. E. & Williams, D. A. 1980, Physics of the interstellar medium (New York, Halsted Press, 1980. 204 p.)

Eislöffel, J., Mundt, R., Ray, T. P., & Rodríguez, L. F. 2000, Protostars and Planets IV, 815

Estalella, R., Palau, A., Girart, J. M., et al. 2003, in Revista Mexicana de Astronomia y Astrofisica Conference Series, 135–135

Falle, S. A. E. G., Innes, D. E., & Wilson, M. J. 1987, MNRAS, 225, 741

Falle, S. A. E. G., Komissarov, S. S., & Joarder, P. 1998, MNRAS, 297, 265

Falle, S. A. E. G. & Raga, A. C. 1993, MNRAS, 261, 573

Falle, S. A. E. G. & Raga, A. C. 1995, MNRAS, 272, 785

Favata, F., Fridlund, C. V. M., Micela, G., Sciortino, S., & Kaas, A. A. 2002, A&A, 386, 204

Fendt, C. & Zinnecker, H. 1998, A&A, 334, 750

Fendt, C. & Zinnecker, H. 2000, in IAU Symposium, 112P–+

Ferrari, A., Habbal, S. R., Rosner, R., & Tsinganos, K. 1984, ApJ, 277, L35

Ferreira, J. 1997, A&A, 319, 340

Fiege, J. D. & Henriksen, R. N. 1996, MNRAS, 281, 1038

Figer, D. F., Najarro, F., & Kudritzki, R. P. 2004, ApJ, 610, L109

Frank, A., Lery, T., Gardiner, T. A., Jones, T. W., & Ryu, D. 2000, ApJ, 540, 342

Frank, A. & Mellema, G. 1996, ApJ, 472, 684

Frank, A. & Noriega-Crespo, A. 1994, A&A, 290, 643

Frank, A., Ryu, D., Jones, T. W., & Noriega-Crespo, A. 1998, ApJ, 494, L79+

Fridlund, C. V. M. & Liseau, R. 1998, ApJ, 499, L75+

Fridlund, M., Huldtgren, M., & Liseau, R. 1997, in IAU Symp. 182: Herbig-Haro Flows and the Birth of Stars, 19–28

Fukue, J. 1982, PASJ, 34, 483

Furth, H., Killeen, J., & Rosenbluth, M. 1963, Physics of Fluids, 6, 459

Gaetz, T. J., Edgar, R. J., & Chevalier, R. A. 1988, ApJ, 329, 927

Gardiner, T. A., Frank, A., & Hartmann, L. 2003, ApJ, 582, 269

Gardiner, T. A. & Stone, J. M. 2005, Journal of Computational Physics, 205, 509

Ghez, A. M., Neugebauer, G., & Matthews, K. 1993, ApJ, 106, 2005

Girart, J. M., Estalella, R., Anglada, G., et al. 1997, ApJ, 489, 734

Godunov, S. 1959, Mat. Sb., 47, 271, in Russian, translation in: *US Joint Publ. Res. Service, JPRS*, 7226 (1969)

Godunov, S. 1972, Numerical Methods for Mechanics of Continuum Medium (Siberian Branch of USSR Acad. of Sci., 1972), 1, 26, in Russian, translation by Linde

Goodson, A. P., Böhm, K., & Winglee, R. M. 1999, ApJ, 524, 142

Goodson, A. P. & Winglee, R. M. 1999, ApJ, 524, 159

Goodson, A. P., Winglee, R. M., & Boehm, K. 1997, ApJ, 489, 199

Gredel, R. & Reipurth, B. 1994a, A&A, 289, L19

Gredel, R. & Reipurth, B. 1994b, A&A, 289, L19

Gueth, F., Schilke, P., & McCaughrean, M. J. 2001, A&A, 375, 1018

Hardee, P. E. & Rosen, A. 2002, ApJ, 576, 204

Haro, G. 1952, ApJ, 115, 572

Harten, A. 1983, Journal of Computational Physics, 49, 151

Harten, A., Engquist, B., Osher, S., & Chakravarthy, S. R. 1987, Journal of Computational Physics, 71, 231

Hartigan, P., Bally, J., Reipurth, B., & Morse, J. A. 2000a, Protostars and Planets IV, 841

Hartigan, P., Morse, J., Palunas, P., Bally, J., & Devine, D. 2000b, AJ, 119, 1872

Hartigan, P., Raymond, J., & Hartmann, L. 1987, ApJ, 316, 323

Hartmann, L. & Raymond, J. C. 1984, ApJ, 276, 560

Hawley, S. L. 1993, PASP, 105, 955

Hayes, J. C., Norman, M. L., Fiedler, R. A., et al. 2006, ApJS, 165, 188

Henri, G. & Pelletier, G. 1991, ApJ, 383, L7

Henriksen, R. N. & Rayburn, D. R. 1971, MNRAS, 152, 323

Herbig, G. H. 1951, ApJ, 113, 697

Hirano, N., Hayashi, S. S., Umemoto, T., & Ukita, N. 1998, ApJ, 504, 334

Hirano, N., Mikami, H., Umemoto, T., Yamamoto, S., & Taniguchi, Y. 2001, ApJ, 547, 899

Hollenbach, D. & McKee, C. F. 1979, ApJS, 41, 555

Icke, V., Balick, B., & Frank, A. 1992a, A&A, 253, 224

Icke, V., Mellema, G., Balick, B., Eulderink, F., & Frank, A. 1992b, Nature, 355, 524

Imamura, J. N., Wolff, M. T., & Durisen, R. H. 1984, ApJ, 276, 667

Innes, D. E., Giddings, J. R., & Falle, S. A. E. G. 1987, MNRAS, 224, 179

Itoh, Y., Kaifu, N., Hayashi, M., et al. 2000, PASJ, 52, 81

Jackson, J. D. 1975, Classical electrodynamics (92/12/31, New York: Wiley, 1975, 2nd ed.)

Kahn, F. D. 1974, A&A, 37, 149

Kant, I. 1755, Universal Natural History and Theory of the Heavens (Internet), 1–10

Klein, R. I., McKee, C. F., & Colella, P. 1994, ApJ, 420, 213

Kominsky, P. 2006, Derivation of MHD Equations

Königl, A. 1982, ApJ, 261, 115

Königl, A. 1989, ApJ, 342, 208

Königl, A. 1991, ApJ, 370, L39

Lada, C. J. 1987, in IAU Symp. 115: Star Forming Regions, 1–15

Lada, C. J. 2006, ApJ, 640, L63

Ladd, E. F. & Hodapp, K.-W. 1997, ApJ, 474, 749

Landau, L. D. & Lifshitz, E. M. 1959, Fluid mechanics (Course of theoretical physics, Oxford: Pergamon Press, 1959)

Laney, C. B. 1998, Computational gasdynamics (Cambridge: Cambridge University Press), xiv+613

Laplace, P.-S. 1796, Exposition du systeme du monde, Vol. VI (Paris: Bachelier), 500–509

Lax, P. & Wendroff, B. 1960, Commun. Pure Appl. Math., 13, 217

Lay, O. P., Carlstrom, J. E., Hills, R. E., & Phillips, T. G. 1994, ApJ, 434, L75

Lery, T., Henriksen, R. N., & Fiege, J. D. 1999, A&A, 350, 254

Lery, T., Henriksen, R. N., Fiege, J. D., et al. 2002, A&A, 387, 187

Leveque, R. 1997, Journal of Comutational Physics, 131, 327

Li, Z. & Shu, F. H. 1996, ApJ, 468, 261

Lim, A. J., Rawlings, J. M. C., & Williams, D. A. 1999, MNRAS, 308, 1126

Lim, A. J. & Steffen, W. 2001, MNRAS, 322, 166

Lim, J. & Takakuwa, S. 2005, Journal of Korean Astronomical Society, 38, 237

Liseau, R., Fridlund, C. V. M., & Larsson, B. 2005, ApJ

Liska, R. & Wendroff, B. 2003, SIAM J. Sci. Comput., 25, 995

Liu, X.-D., Osher, S., & Chan, T. 1994, Journal of Computational Physics, 115, 200

Londrillo, P. & Del Zanna, L. 2000, ApJ, 530, 508

Lovelace, R. V. E., Romanova, M. M., & Bisnovatyi-Kogan, G. S. 1995, MNRAS, 275, 244

Lucas, P. W. & Roche, P. F. 1997, MNRAS, 286, 895

Lüst, R. 1952, Zeitschrift fur Naturforschung, 7, 87

Lynden-Bell, D. & Pringle, J. E. 1974, MNRAS, 168, 603

MacNeice, P., Olson, K., Mobarry, C., de Fainchtein, R., & Packer, C. 2000, Computer Physics Communications, 126, 330

Maiorano, E., Masetti, N., Palazzi, E., et al. 2006, A&A, 455, 423

Masciadri, E. & Raga, A. C. 2002, ApJ, 568, 733

Masson, C. R. & Chernin, L. M. 1992, ApJ, 387, L47

Masson, C. R. & Chernin, L. M. 1993, ApJ, 414, 230

Mathieu, R. D. 1994, ARA&A, 32, 465

Matt, S., Goodson, A. P., Winglee, R. M., & Böhm, K. 2002, ApJ, 574, 232

Matt, S. & Pudritz, R. E. 2004, ApJ, 607, L43

Matt, S. & Pudritz, R. E. 2005, MNRAS, 356, 167

Mayor, M., Duquennoy, A., Halbwachs, J.-L., & Mermilliod, J.-C. 1992, in ASP Conf. Ser. 32: IAU Colloq. 135: Complementary Approaches to Double and Multiple Star Research, ed. H. A. McAlister & W. I. Hartkopf, 73–+

Mellema, G., Eulderink, F., & Icke, V. 1991, A&A, 252, 718

Mellema, G. & Frank, A. 1997, MNRAS, 292, 795

Ménard, F. & Duchêne, G. 2004, A&A, 425, 973

Mignone, A., Massaglia, S., & Bodo, G. 2004, Ap&SS, 293, 199

Mirabel, I. F. & Rodríguez, L. F. 1999, ARA&A, 37, 409

Mirabel, I. F., Rodriguez, L. F., Cordier, B., Paul, J., & Lebrun, F. 1992, Nature, 358, 215

Moriarty-Schieven, G. H., Johnstone, D., Bally, J., & Jenness, T. 2005, in Protostars and Planets V, 8527–+

Moriarty-Schieven, G. H. & Snell, R. L. 1988, ApJ, 332, 364

Moriarty-Schieven, G. H. & Wannier, P. G. 1991, ApJ, 373, L23

Mullan, D. J. 1971, MNRAS, 153, 145

Mundt, R., Ray, T. P., & Raga, A. C. 1991, A&A, 252, 740

Najita, J. R. & Shu, F. H. 1994, ApJ, 429, 808

Norman, M. L., Smarr, L., Smith, M. D., & Wilson, J. R. 1981, ApJ, 247, 52

O'Dell, C. R., Wen, Z., & Hu, X. 1993, ApJ, 410, 696

Okuda, T. & Ikeuchi, S. 1986, PASJ, 38, 199

Opher, M., Liewer, P. C., Velli, M., et al. 2004, ApJ, 611, 575

Orszag, S. A. & Tang, C.-M. 1979, Journal of Fluid Mechanics, 90, 129

Osterbrock, D. E. 1958, PASP, 70, 399

O'Sullivan, S. D. 1999, PhD thesis, Dublin Institute for Advanced Studies

Palacios, J. & Eiroa, C. 1999, A&A, 346, 233

Paredes, J. M., Ribó, M., Ros, E., Martí, J., & Massi, M. 2002, A&A, 393, L99

Parise, B., Belloche, A., Leurini, S., et al. 2006, A&A, 454, L79

Parker, E. N. 1958, ApJ, 128, 664

Patience, J., White, R. J., Ghez, A. M., et al. 2002, ApJ, 581, 654

Pound, M. W. & Bally, J. 1991, ApJ, 383, 705

Powell, K. G., Roe, P. L., Linde, T. J., Gombosi, T. I., & de Zeeuw, D. L. 1999, Journal of Computational Physics, 154, 284

Preibisch, T., Balega, Y., Hofmann, K.-H., Weigelt, G., & Zinnecker, H. 1999, New Astronomy, 4, 531

Pringle, J. E. 1989, MNRAS, 236, 107

Pudritz, R. E. 1985, ApJ, 293, 216

Pudritz, R. E. & Norman, C. A. 1983, ApJ, 274, 677

Pudritz, R. E. & Norman, C. A. 1986, ApJ, 301, 571

Pyo, T.-S., Hayashi, M., Kobayashi, N., et al. 2002, ApJ, 570, 724

Quillen, A. C., Thorndike, S. L., Cunningham, A., et al. 2005, ApJ, 632, 941

Raga, A., Cabrit, S., Dougados, C., & Lavalley, C. 2001, A&A, 367, 959

Raga, A. C., Binette, L., Canto, J., & Calvet, N. 1990, ApJ, 364, 601

Raga, A. C. & Bohm, K. H. 1987, ApJ, 323, 193

Raga, A. C. & Canto, J. 1989, ApJ, 344, 404

Raga, A. C., Mellema, G., & Lundqvist, P. 1997, ApJS, 109, 517

Raga, A. C., Taylor, S. D., Cabrit, S., & Biro, S. 1995, A&A, 296, 833

Raymond, J. C., Hartmann, L., & Hartigan, P. 1988, ApJ, 326, 323

Reipurth, B., Heathcote, S., Roth, M., Noriega-Crespo, A., & Raga, A. C. 1993, ApJ, 408, L49

Renaud, N. & Henri, G. 1998, MNRAS, 300, 1047

Roache, P. J. 1976, Computational Fluid Dynamics (Computational Fluid Dynamics, Albuquerque: Hermosa, 1976)

Rodríguez, L. F., D'Alessio, P., Wilner, D. J., et al. 1998, Nature, 395, 355

Rodríguez, L. F., Porras, A., Claussen, M. J., et al. 2003, ApJ, 586, L137

Roe, P. L. 1981, Journal of Computational Physics, 43, 357

Roe, P. L. & Balsara, D. S. 1996, SIAM Journal on Applied Mathematics, 56, 57

Ryu, D. & Jones, T. W. 1995, ApJ, 442, 228

Ryu, D., Jones, T. W., & Frank, A. 1995, ApJ, 452, 785

Ryu, D., Miniati, F., Jones, T. W., & Frank, A. 1998, ApJ, 509, 244

Sakashita, S., Hanami, H., & Umemura, M. 1984, Ap&SS, 98, 315

Saugé, L. & Henri, G. 2006, A&A, 454, L1

Scarrott, S. M. 1988, MNRAS, 231, 39P

Schwartz, R. D. 1975, ApJ, 195, 631

Schwartz, R. D. 1978, ApJ, 223, 884

Shirley, Y. L., Evans, N. J., & Rawlings, J. M. C. 2002, ApJ, 575, 337

Shu, F., Najita, J., Ostriker, E., et al. 1994a, ApJ, 429, 781

Shu, F. H., Adams, F. C., & Lizano, S. 1987a, ARA&A, 25, 23

Shu, F. H., Lizano, S., & Adams, F. C. 1987b, in IAU Symp. 115: Star Forming Regions, 417–433

Shu, F. H., Lizano, S., Ruden, S. P., & Najita, J. 1988, ApJ, 328, L19

Shu, F. H., Najita, J., Ruden, S. P., & Lizano, S. 1994b, ApJ, 429, 797

Simon, M., Ghez, A. M., Leinert, C., et al. 1995, ApJ, 443, 625

Snell, R. L., Loren, R. B., & Plambeck, R. L. 1980, ApJ, 239, L17

Sod, G. A. 1978, Journal of Computational Physics, 27, 1

Stone, J. M. 1997, ApJ, 487, 271

Stone, J. M. & Norman, M. L. 1992, ApJS, 80, 753

Strang, G. 1968, SIAM Journal of Numerical Analysis, 5, 506

Strom, K. M., Strom, S. E., Wolff, S. C., Morgan, J., & Wenz, M. 1986, ApJS, 62, 39

Strom, S. E., Vrba, F. J., & Strom, K. M. 1976, AJ, 81, 638

Sutherland, R. S. & Dopita, M. A. 1993, ApJ, 88, 253

Tamura, M. & Sato, S. 1989, AJ, 98, 1368

Terebey, S., Vogel, S. N., & Myers, P. C. 1989, ApJ, 340, 472

Toro, E. F. 1997, Riemann solvers and numerical methods for fluid dynamics: a practical introduction (Heidelberg: Springer-Verlag), xviii + 592

Toth, G. & Odstrčil, D. 1996, Journal of Computational Physics, 128, 82

Truelove, J. K., Klein, R. I., McKee, C. F., et al. 1998, ApJ, 495, 821

Uchida, Y. & Shibata, K. 1985, PASJ, 37, 515

Van Dyke, M. 1964, An Album of Fluid Motion (Parabolic Press)

van Leer, B. 1979, Journal of Computational Physics, 135, 229

Vlemmings, W. H. T., Diamond, P. J., & Imai, H. 2006, Nature, 440, 58

von Neumann, J. & Richtmyer, R. D. 1950, Journal of Applied Physics, 21, 232

von Weizsäcker, C. F. 1943, Zeitschrift fur Astrophysik, 22, 319

Weber, E. J. & Davis, L. J. 1967, ApJ, 148, 217

Whelan, E. T., Ray, T. P., Bacciotti, F., et al. 2005, Nature, 435, 652

Whitham, G. B. 1974, Linear and Nonlinear Waves, Pure and Applied Mathematics (New York, NY: Wiley-Interscience)

Wolfire, M. G. & Cassinelli, J. P. 1987, ApJ, 319, 850

Wood, D. O. S. & Churchwell, E. 1989, ApJ, 340, 265

Woodward, P. & Colella, P. 1984, Journal of Computational Physics, 54, 115

Yorke, H. W. & Kruegel, E. 1977, A&A, 54, 183

Zanni, C., Ferrari, A., Rosner, R., Bodo, G., & Massaglia, S. 2007, ArXiv Astrophysics e-prints

Zinnecker, H., Brandner, W., & Reipurth, B. 1992, in ASP Conf. Ser. 32: IAU Colloq. 135: Complementary Approaches to Double and Multiple Star Research, ed. H. A. McAlister & W. I. Hartkopf, 50–+

A

List of variables used in the text

For clarity, the variables used in the text have been collected together here.

α	Mach angle
β	ratio of magnetic pressure to thermal pressure
γ	adiabatic/polytropic index or ratio of specific heats
δ_Q	charge density
$\mathcal{E}$	electric field
η	density contrast
λ	wavelength
$\overline{\overline{\pi}}$	pressure tensor
ρ	density
σ_{csa}	cross-sectional area
σ	conductivity
χ	conserved quantity
ω	angular velocity

Λ	cooling energy loss rate
Φ	Magnetic Flux
$\mathbf{A}$	magnetic vector potential
A_V	extinction
$\mathbf{a}$	acceleration
$\mathbf{B}$	magnetic flux density
c	speed of light
c_{sound}	Sound speed
c_{slow}	Slow Magnetosonic speed
c_{fast}	Fast Magnetosonic speed
c_a	Alfvén speed
$\mathbf{D}$	electric flux density
G	Universal gravitational constant
$\mathbf{F}, \mathbf{G}, \mathbf{H}$	flux vectors
$\mathbf{J}$	electric current density
k	Boltzmann’s number
K_I	collisional ionisation rate coefficient
K_R	radiative recombination rate coefficient
$L_{cooling}$	Energy lost due to radiative cooling
L_D	Debye-Huckel length
m	mass
M_J	Jeans mass
R_e	Reynolds number
R_m	Magnetic Reynolds number
$\mathbf{P}$	vector of primitive variables
p	pressure
p*	total pressure (magnetic + thermal)
T_{bol}	bolometric temperature
T	temperature
$\mathbf{u}$	bulk or flow velocity
$\mathbf{v}$	total (bulk + random) velocity
$\mathbf{w}$	random thermal velocity

B

Derivation of the energy equation from the second moment of the Boltzmann equation

This derivation uses parts of Kominsky (2006). The collisionless form of the Boltzmann equation is:

$$\frac{\partial n\langle\chi\rangle}{\partial t} + \boldsymbol{\nabla}_x n\langle \mathbf{v}\chi\rangle + n\langle \mathbf{a}\boldsymbol{\nabla}_v.\chi\rangle = 0 \tag{B.1}$$

where χ represents a conserved quantity such as density, total energy or momentum.

Taking the second moment, $\chi = \frac{1}{2}mv^2 = \frac{1}{2}m\mathbf{v}\cdot\mathbf{v}$, gives

$$\frac{\partial}{\partial t}\left[\rho\left(\mathbf{u}\cdot\mathbf{u} + \langle\mathbf{w}\cdot\mathbf{w}\rangle\right)\right] + \boldsymbol{\nabla}_x\cdot\left(\frac{1}{2}\rho\langle\left(\mathbf{v}\cdot\mathbf{v}\right)\mathbf{v}\rangle\right) + \rho\mathbf{a}.\boldsymbol{\nabla}_v\frac{1}{2}\mathbf{u}^2 = 0 \tag{B.2}$$

Taking the definition of $P = \frac{1}{d}\langle\mathbf{w}\cdot\mathbf{w}\rangle$ where d is the dimensionality of the system (often 3). Introducing the adiabatic index or ratio of specific heats;

$$\gamma = \frac{d+2}{d} \tag{B.3}$$

for a monatomic gas.

$$P = \frac{1}{d}\rho\langle w^2\rangle = \frac{\gamma-1}{\gamma}\rho\langle w^2\rangle \tag{B.4}$$

Define the energy density,

$$E = \frac{1}{2}\rho u^2 + \frac{p}{\gamma - 1} \tag{B.5}$$

The first term in Equation B.2 is then

$$\frac{\partial}{\partial t}\left[\rho\left(\mathbf{u}\cdot\mathbf{u} + \langle\mathbf{w}\cdot\mathbf{w}\rangle\right)\right] = \frac{\partial E}{\partial t} \tag{B.6}$$

The second term:

$$\begin{aligned}
\boldsymbol{\nabla}.\left(\frac{1}{2}\rho\langle\left(\mathbf{v}\cdot\mathbf{v}\right)\mathbf{v}\rangle\right) &= \boldsymbol{\nabla}.\left(\frac{1}{2}\rho\langle\left(\left(\mathbf{u}+\mathbf{w}\right)\cdot\left(\mathbf{u}+\mathbf{w}\right)\right)\left(\mathbf{u}+\mathbf{w}\right)\rangle\right) \\
&= \boldsymbol{\nabla}.\left(\frac{1}{2}\rho\langle\left(\mathbf{u}^2 + 2\mathbf{u}\cdot\mathbf{w} + \mathbf{w}^2\right)\left(\mathbf{u}+\mathbf{w}\right)\rangle\right) \\
&= \boldsymbol{\nabla}.\left(\frac{1}{2}\rho u^2\mathbf{u} + \frac{1}{2}\rho\langle w^2\rangle\mathbf{u} + \rho u w^2 + \frac{1}{2}\rho w^3\right) \\
&= \boldsymbol{\nabla}.\left(E\mathbf{u} + P\mathbf{u} + \frac{1}{2}\rho w^3\right)
\end{aligned}$$

Excluding gravity, the acceleration due to electromagnetic forces is:

$$\mathbf{a} = \frac{q}{m}\left(\mathbf{E} + \mathbf{u}\times\mathbf{B}\right) \tag{B.7}$$

The acceleration term is then:

$$\boldsymbol{\nabla}_v\chi = \frac{1}{2}m\boldsymbol{\nabla}_v\left(\mathbf{v}\cdot\mathbf{v}\right) = \mathbf{v}\cdot m\boldsymbol{\nabla}_v\left(\mathbf{v}\right) = m\mathbf{v} \tag{B.8}$$

$$-n\langle\mathbf{a}\cdot\boldsymbol{\nabla}_v\chi\rangle = -n\langle\frac{\mathbf{F}}{m}\cdot m\mathbf{v}\rangle = -n\langle\mathbf{F}\cdot\mathbf{v}\rangle \tag{B.9}$$

Now,

$$\langle\mathbf{F}\cdot\mathbf{v}\rangle = \langle\mathbf{F}\cdot\mathbf{u}\rangle + \langle\mathbf{F}\cdot\mathbf{w}\rangle = \langle\mathbf{F}\rangle\mathbf{u} + \langle\mathbf{F}\cdot\mathbf{w}\rangle \tag{B.10}$$

For all velocity-independent forces **F**

$$\langle\mathbf{F}\cdot\mathbf{w}\rangle = \mathbf{F}\cdot\langle\mathbf{w}\rangle = 0 \tag{B.11}$$

For the Lorentz force,

$$\begin{aligned}
\langle\mathbf{F}\cdot\mathbf{w}\rangle &= \langle\left(q\left(\mathbf{E} + \mathbf{v}\times\mathbf{B}\right)\right)\cdot\mathbf{w}\rangle \\
&= q\langle\left(\mathbf{v}\times\mathbf{B}\right)\cdot\mathbf{w}\rangle + q\langle\mathbf{E}\cdot\mathbf{w}\rangle \\
&= q\mathbf{u}\times\mathbf{B}\langle w\rangle + q\langle\left(w\times B\right)\cdot w\rangle
\end{aligned}$$

The moment equation is now:

$$\frac{\partial}{\partial t}E + \boldsymbol{\nabla}_x \left(u\left(E+P\right)\right) - nq\mathbf{u}\cdot\mathbf{E} = 0 \tag{B.12}$$

Defining the current density:

$$\mathbf{J} = nq\mathbf{u} \tag{B.13}$$

$$\frac{\partial}{\partial t}E + \boldsymbol{\nabla}_x \left(u\left(E+P\right)\right) - \mathbf{J}\cdot\mathbf{E} = 0 \tag{B.14}$$

Using vector identities, and assuming infinite conductivity, $\frac{\mathbf{J}}{\sigma} = \mathbf{E} + \mathbf{u}\times\mathbf{B} = 0$ the $\mathbf{J}\cdot\mathbf{E}$ term can be written as:

$$\begin{aligned}
\mathbf{J}\cdot\mathbf{E} &= \left(\boldsymbol{\nabla}\times\mathbf{B}\right)\cdot\mathbf{E} \\
&= \left(\boldsymbol{\nabla}\times\mathbf{E}\right)\cdot\mathbf{B} - \boldsymbol{\nabla}\cdot\left(\mathbf{E}\times\mathbf{B}\right) \\
&= \frac{\partial\mathbf{B}}{\partial t}\cdot\mathbf{B} - \boldsymbol{\nabla}\cdot\left(\mathbf{u}\times\mathbf{B}\times\mathbf{B}\right) \\
&= \frac{1}{2}\frac{\partial B^2}{\partial t} - \boldsymbol{\nabla}\cdot\big(\left(\mathbf{u}\cdot\mathbf{B}\right)\mathbf{B} - B^2\mathbf{u}\big)
\end{aligned}$$

Finally, the conservation of energy is:

$$\frac{\partial E}{\partial t} + \boldsymbol{\nabla}_x\left(u\left(E+P+\frac{1}{2}B^2\right) - \left(\mathbf{u}\cdot\mathbf{B}\right)\mathbf{B}\right) = 0 \tag{B.15}$$